To appear in *The Cold Universe: Saas-Fee Advanced Course 32*
ed. D. Pfenniger. Berlin: Springer-Verlag, 2003, in press

Astrophysics of Dust in Cold Clouds

B. T. Draine
Princeton University

Dust plays an increasingly important role in astrophysics. Historically, dust was first recognized for its obscuring effects, and the need to correct observed intensities for attenuation by dust continues today. But with the increasing sensitivity of IR, FIR, and submm telescopes, dust is increasingly important as a diagnostic, with its emission spectrum providing an indicator of physical conditions, and its radiated power bearing witness to star populations of which we might otherwise be unaware. Finally, and most fundamentally, dust is now understood to play many critical roles in galactic evolution. By sequestering selected elements in the solid grains, and by catalyzing formation of the H_2 molecule, dust grains are central to the chemistry of interstellar gas. Photoelectrons from dust grains can dominate the heating of gas in regions where ultraviolet starlight is present, and in dense regions the infrared emission from dust can be an important cooling mechanism. Finally, dust grains can be important in interstellar gas dynamics, communicating radiation pressure from starlight to the gas, and providing coupling of the magnetic field to the gas in regions of low fractional ionization.

We would like to understand these effects of dust in the Milky Way, in other galaxies, and as a function of cosmic time. These lectures are organized around topics in the astrophysics of dust in the the Milky Way, as this is our best guide to understanding and modelling dust long ago and far away.

1 Introduction to Interstellar Dust

We begin with a brief review of some of the observational evidence which informs our study of interstellar dust.

1.1 Interstellar Extinction

Through study of open star clusters in the Galaxy, Trumpler (1930) found that distant stars were dimmed by something in addition to the inverse square law, and concluded that interstellar space in the galactic plane contained "fine cosmic dust particles of various sizes ... producing the observed selective absorption". Over the past 7 decades we have built on Trumpler's pioneering study, but many aspects of interstellar dust – including its chemical composition! – remain uncertain. Let us therefore begin by reviewing the different ways in which nature permits us to study interstellar dust.

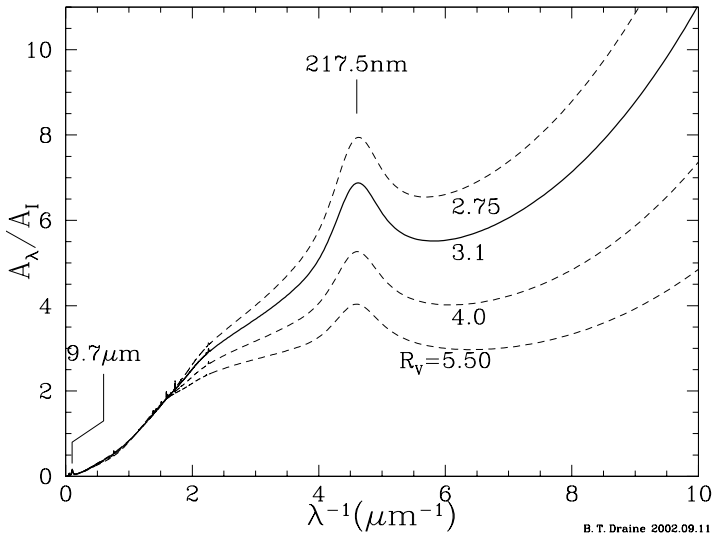

Fig. 1. Extinction at wavelength λ, relative to the extinction at $I = 900\,\mathrm{nm}$, as a function of inverse wavelength λ^{-1}, for Milky Way regions characterized by different values of $R_V \equiv A_V/E(B-V)$, where A_B is the extinction at $B = 4400\,\mu\mathrm{m}$, A_V is the extinction at $V = 5500\,\mu\mathrm{m}$, and the "reddening" $E(B-V) \equiv A_B - A_V$. Note the rapid rise in extinction in the vacuum ultraviolet ($\lambda \lesssim 0.2\,\mu\mathrm{m}$) for regions with $R_V \lesssim 4$. The normalization per H nucleon is approximately $A_I/N_\mathrm{H} \approx 2.6 \times 10^{-22}\,\mathrm{cm}^2/\mathrm{H}$. The silicate absorption feature (§1.5) at $9.7\,\mu\mathrm{m}$ and the diffuse interstellar bands (§1.6) are barely visible.

Trumpler analyzed the interaction of light with interstellar dust, and this remains our most direct way to study interstellar dust. We use stars as "standard candles", and study the "selective extinction" – or "reddening" – of starlight by the dust. With the assumption that the extinction ($\equiv$ absorption + scattering) goes to zero at wavelengths $\lambda \to \infty$, and observing the star at sufficiently long wavelength (to, in effect, determine its distance) one can determine the attenuation of the starlight by dust as a function of wavelength. Because atomic hydrogen absorbs strongly for $h\nu > 13.6\,\mathrm{eV}$, it it is only possible to measure the contribution of dust to the extinction at $h\nu < 13.6\,\mathrm{eV}$, or $\lambda > 912$Å. A typical "extinction curve" – the extinction as a function of wavelength or frequency — is shown in Figure 1, showing the rapid rise in extinction in the vacuum ultraviolet. Observed extinction curves vary in shape from one line-of-sight to another, but appear to approximately form a one-parameter family (Cardelli et al. 1989); the parameter is often taken to be the ratio $R_V \equiv (A_B - A_V)/A_V$, where A_B and A_V are the extinctions measured in the B (4400Å) and V (5500Å) spectral bands. A parametrization of the extinction curve was provided by Cardelli et al.; the curves in Fig. 1

were calculated using a more recent prescription by Fitzpatrick (1999), with the extinction in the infrared following Draine (1989b).

We will discuss dust grain optics below, but it is clear that if the dust grains were large compared to the wavelength, we would be in the "geometric optics" limit and the extinction cross-section would be independent of wavelength. Therefore the tendency for the extinction to rise even at the shortest wavelengths where we can measure it tells us that grains smaller than the wavelength must be making an appreciable contribution to the extinction at all of observed wavelengths. As we will see below, "small" means (approximately) that $2\pi a|m-1|/\lambda \lesssim 1$, where $m(\lambda)$ is the complex refractive index. Thus if $|m-1| \approx 1$ at $\lambda = 0.1\,\mu$m,

- we must have large numbers of grains with $a \lesssim .015\,\mu$m.

1.2 Scattering of Starlight by Dust Grains

When an interstellar cloud happens to be unusually near one or more bright stars, we have a "reflection nebula", where we see the starlight photons which have been scattered by the dust in the cloud. The spectrum of the light coming from the cloud surface shows the stellar absorption lines, showing that scattering rather than some emission process is responsible. By comparing the observed scattered intensity with the estimated intensity of the starlight incident on the cloud, it is possible to infer the albedo of the dust – the ratio of scattering cross section to extinction cross section. The result is that in the optical the interstellar dust mixture has an albedo $\omega \approx 0.5$ – scattering is about as important as absorption – and the grains are somewhat forward scattering, with $\langle \cos\theta \rangle \approx 0.5$. Rayleigh scattering by particles small compared to the wavelength has $\langle \cos\theta \rangle \approx 0$, so this tells us that

- the particles dominating the scattering at $\lambda \approx 0.6\,\mu$m have $a \gtrsim \lambda/2\pi \approx 0.1\,\mu$m.

1.3 Polarization of Starlight

The polarization of starlight was discovered in 1949 (Hall 1949; Hall & Mikesell 1949; Hiltner 1949a,b). When it was realized that the degree of polarization tended to be larger for stars with greater reddening, and that stars in a given region of the sky tended to have similar polarization directions, it was obvious that the polarization is produced by the interstellar medium: light propagating through the interstellar medium becomes linearly polarized as a result of preferential extinction of one linear polarization mode relative to the other. The polarization percentage typically peaks near the V band (5500Å), and can be empirically described by the "Serkowski law" (Serkowski 1973):

$$p(\lambda) \approx p(\lambda_{\rm max}) \exp[-K \ln^2(\lambda/\lambda_{\rm max})] \quad , \tag{1}$$

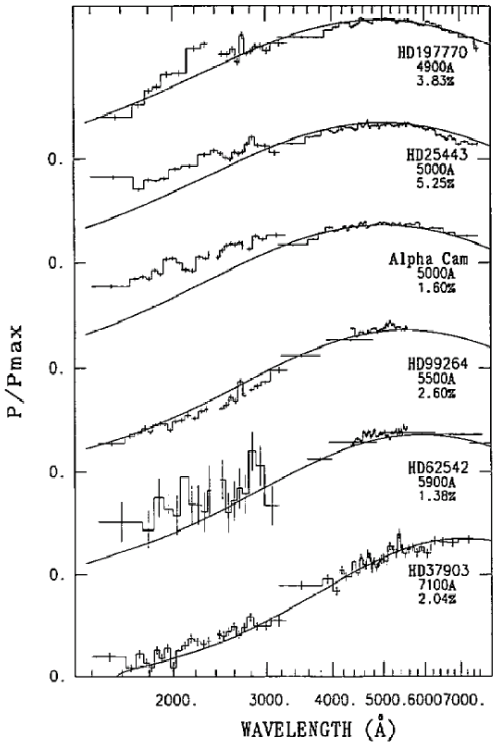

Fig. 2. Linear polarization in the ultraviolet measured by Clayton et al. (1992). The solid line is the "Serkowski law" fit to the data. Figure from Clayton et al (1992).

with $\lambda_{\rm max} \approx 5500$Å and $K \approx 1.15$. This "linear dichroism" of the interstellar medium is due to dust grains which are partially aligned by the interstellar magnetic field. The peak polarization $p_{\rm max}$ is found to fall within an envelope $0 < p_{\rm max} \leq 0.09(E(B-V)/{\rm mag})$, or $0 < p_V \lesssim 0.03\tau_V$; the maximum values are presumed to arise on sightlines where the magnetic field is uniform and perpendicular to the line-of-sight. While the "Serkowski law" was put forward as a fit to the observed polarization at $0.3\,\mu{\rm m} \lesssim \lambda \lesssim 1\,\mu{\rm m}$, it turns out to give a surprisingly good approximation to the measured linear polarization in the vacuum ultraviolet (Clayton et al 1992, Wolff et al 1997) as seen in Figure 2

The mechanism responsible for the grain alignment remains a fascinating puzzle, which we will discuss below. Independent of the grain alignment mechanism, however, we can infer the sizes of the interstellar grains responsible for this polarization by noting that the extinction rises rapidly into the UV whereas the polarization drops (Kim & Martin 1995). This can be understood if the grains responsible for the polarization have sizes a such that

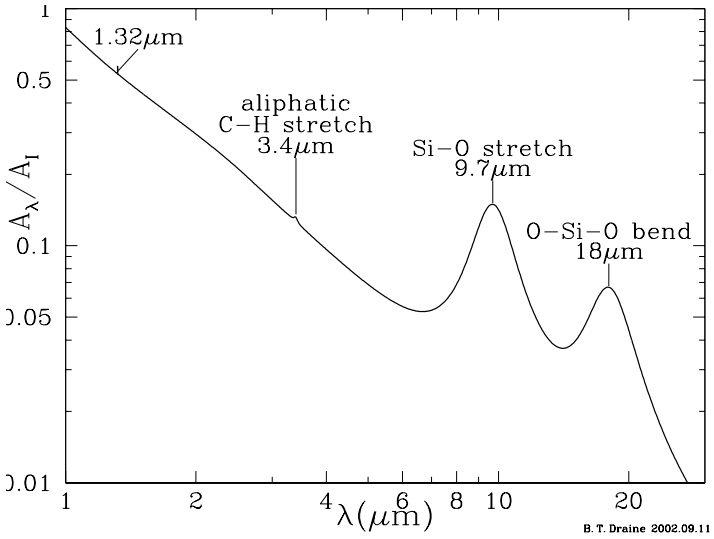

Fig. 3. Infrared extinction, relative to extinction at $I = 900\,\mathrm{nm}$, showing the strong $9.7\,\mu$m and $18\,\mu$m silicate features, the $3.4\,\mu$m aliphatic C-H stretch, and a weak unidentified DIB at $1.32\,\mu$m (Joblin et al. 1990).

$a \approx (\lambda_{\max}/2\pi) \approx 0.1\,\mu$m: then as one proceeds into the UV one moves toward the "geometric optics" limit where both polarization modes suffer the same extinction, so the polarization goes to zero:

- The extinction at $\lambda \approx 0.55\,\mu$m has an appreciable contribution from grains with sizes $a \approx 0.1\,\mu$m which are nonspherical and substantially aligned.
- The grains with $a \lesssim 0.05\,\mu$m which dominate the extinction at $\lambda \lesssim 0.3\,\mu$m are either spherical (which seems unlikely) or minimally aligned.

1.4 Spectroscopy of Dust: The 2175Å Feature

Of what is interstellar dust composed? One may look for spectroscopic clues in the extinction. The extinction curves in Fig. 1 show a conspicuous extinction feature at $\lambda^{-1} = 4.6\,\mu\mathrm{m}^{-1}$, or $\lambda = 2175$Å. The feature is well-described by a Drude profile. The central wavelength is nearly identical on all sightlines, but the width varies significantly from one region to another (Fitzpatrick & Massa 1986).

The strength of this feature implies that the responsible material must be abundant (Draine 1989a): it must be made from H, C, N, O, Mg, Si, S, or Fe. Small graphite grains would have a strong absorption peak at about this frequency (Stecher & Donn 1965; Draine 1989a), due to $\pi \rightarrow \pi^*$ electronic excitations in the sp^2-bonded carbon sheets. Since the carbon skeleton of

polycyclic aromatic hydrocarbon (PAH) molecules resembles a portion of a graphite sheet, such molecules also tend to have strong electronic transitions at about this frequency. It therefore seems likely that the 2175Å feature is due to some form of sp^2-bonded carbon material.

1.5 Spectroscopy of Dust: The Silicate Features

There is a conspicuous infrared absorption feature at 9.7 μm, shown in Figure 3. Silicate minerals generally have strong absorption resonances due to the Si-O stretching mode near 10 μm, and it seems virtually certain that the interstellar 9.7 μm feature is due to silicates. This conclusion is strengthened by the fact that the 10 μm emission feature is seen in the outflows from oxygen-rich stars (which would be expected to condense silicate dust) but not in the outflows from carbon-rich stars. The interstellar 9.7 μm feature is seen both in emission (e.g., in the Trapezium region in Orion [Gillett, Forrest, et al. 1975]) or in extinction in the interstellar medium (Roche & Aitken 1984).

Crystalline silicate minerals generally have sharp features in their 10 μm absorption which are not seen in the broad interstellar 10 μm feature, leading to the conclusion that interstellar silicates are probably amorphous.

Near 18 μm warm interstellar dust shows another emission feature, which is attributable to the Si-O-Si bending mode in amorphous silicates.

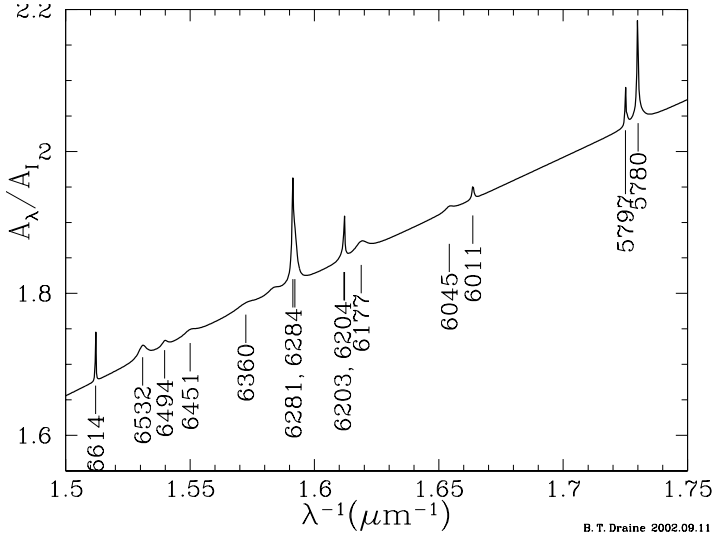

Fig. 4. Extinction at wavelength λ, relative to the extinction at $I = 900$ nm, showing some of the diffuse interstellar bands.

1.6 Spectroscopy of Dust: Diffuse Interstellar Bands

The 3 features at $0.22\,\mu$m, $9.7\,\mu$m, and $18\,\mu$m are by far the strongest features seen in diffuse interstellar dust. There are, in addition, numerous weaker features in the optical known as the "diffuse interstellar bands", or DIBs. Figure 4 shows the extinction for $1.5\,\mu\mathrm{m}^{-1} < \lambda^{-1} < 1.75\,\mu\mathrm{m}^{-1}$, with several conspicuous DIBs present, most notably the DIB at $0.5780\,\mu$m. The strongest DIB falls at 443.0nm. Jenniskens & Desert (1994) report a total of 154 "certain" DIBs in the interval $0.38 - 0.868\,\mu$m, plus another 52 "probable" detections. DIBs were discovered 80 years ago (Heger 1922) and their interstellar nature was established 68 years ago (Merrill 1934).

It is embarassing that Nature has provided astrophysicists with this wealth of spectroscopic clues, yet as of this writing not a single one of the DIBs has been convincingly identified! It seems likely that some of the DIBs may be due to free-flying large molecules; this hypothetis has received support from high resolution spectra of the 5797Å feature (see Figure 5) showing intrinsic ultrafine structure (Sarre et al. 1995; Kerr et al. 1998).

1.7 Spectroscopy of Dust: The 3.4μm Feature

There is a broad absorption feature at $3.4\,\mu$m which is almost certainly due to the C-H stretching mode in hydrocarbons. A recent study by Pendleton & Allamandola (2002) concluded that hydrocarbons with a mixed aromatic (ring) and aliphatic (chain) character provided a good fit to the observed interstellar absorption, including the $3.35 - 3.53\,\mu$m region. This included hydrocarbon films deposited following laser-ablation of amorphous carbon in Ar, followed by exposure to atomic H (Mennella et al. 1999) or from a weakly-ionized plasma produced by laser-ablation of graphite in hydrogen (Scott & Duley 1996; Duley et al. 1998).

1.8 Spectroscopy of Dust: Ice Features

In dark molecular clouds a number of additional absorption features are seen, most notably a strong band at $3.1\,\mu$m which is attributed to the O-H stretching mode in H_2O ice. However, the $3.1\,\mu$m feature is *not* seen on sightlines which are confined to diffuse interstellar clouds (Gillett, Jones et al. 1975).

When a strong $3.1\,\mu$m feature appears in absorption, a number of other absorption features are also seen, including features due to CO ($4.67\,\mu$m), CH_3OH ($3.53\,\mu$m), and CO_2 ($15.2\,\mu$m). The shape of the $3.1\,\mu$m H_2O feature is indicative of the type of ice and the impurities present in it. The relative strengths of the various features indicate that H_2O is the dominant "ice" species, with NH_3, CO, CH_3OH, and CO_2 as secondary constituents.

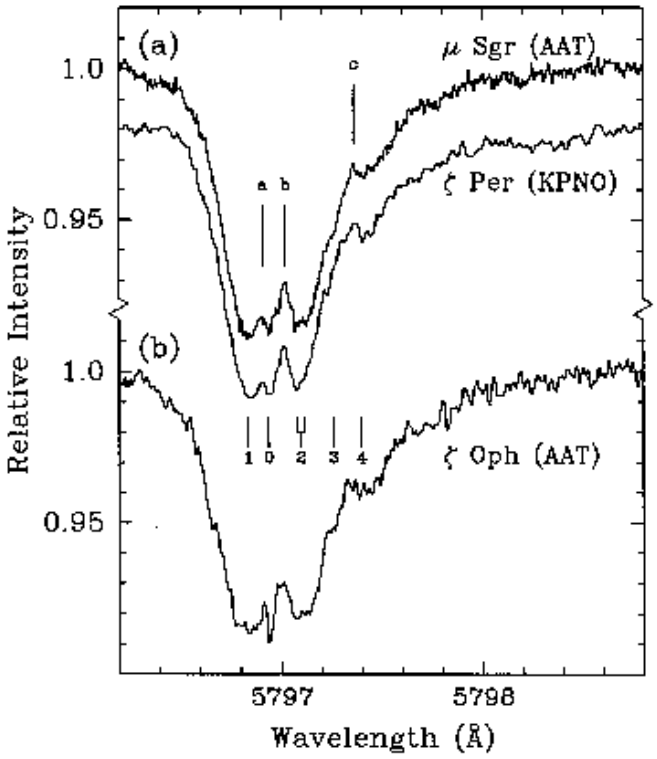

Fig. 5. Fine structure of the 5797Å DIB toward ζ Oph, ζ Per, and μ Sgr (from Kerr et al. 1998). Note in particular the very narrow feature labelled 0.

1.9 Spectroscopy of Dust: PAH Emission Features

A wide variety of galactic objects, including planetary nebulae, HII regions, photodissociation fronts, and reflection nebulae, have strong infrared emission in the 3-13 μm region. Most of the radiated power emerges in 5 broad infrared bands, at 3.3, 6.2, 7.7, 8.6, and 11.3 μm. In Figure 6 we show the 4-15 μm emission observed from the reflection nebula NGC 7023 (Cesarsky et al. 1996). These features are seen in many other objects as well (see, e.g., Boulanger et al. 1998). The emission is quite strong: a significant fraction of the starlight energy incident on the reflection nebula is reradiated in these infrared emission bands – the fraction can be as large as 10-20% depending on the spectral type of the star – so the particles responsible for this emission must be quite abundant, as we will discuss further below.

The emission is thought to result from vibrational modes of polycyclic aromatic hydrocarbon (PAH) molecules. PAHs can be thought of as a section of a graphite "sheet" with the C atoms in a 2-dimensional hexagonal lattice,

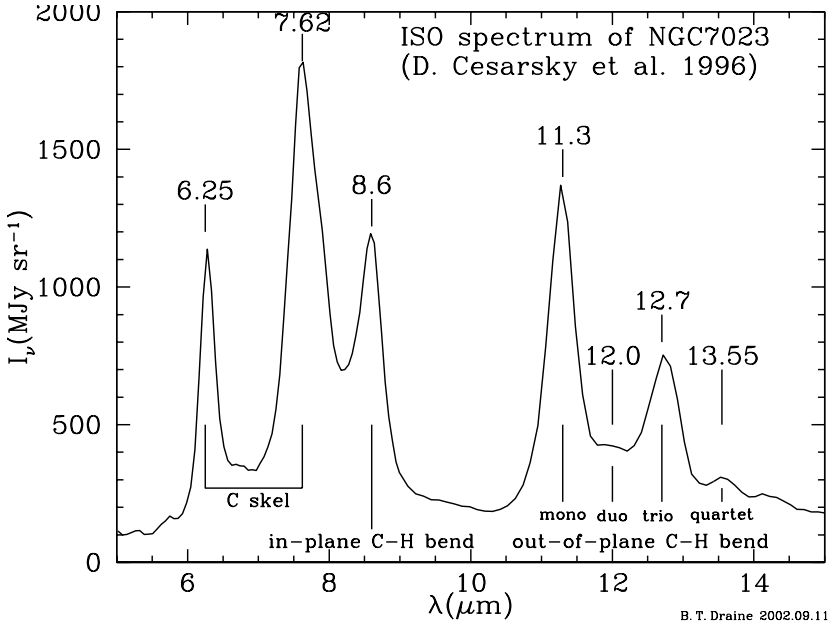

Fig. 6. Emission spectrum of the reflection nebula NGC 7023 measured by ISOCAM (Cesarsky et al. 1996).

with the H atoms attached to C atoms at the edges of the lattice. Three examples of PAHs are shown in Figure 7. When H atoms are attached to the edge of an aromatic ring,

- the C-H stretching mode tends to be at 3.3 μm,
- the C-H in-plane bending mode is near 8.6 μm
- the C-H out-of-plane bending mode tends to fall at 11.3, 11.9, 12.7, or 13.6 μm, depending on whether there are one, two, three, or four adjacent C-H bonds ("solo-", "duo-", "trio-", or "quartet-" C-H). The observed spectra suggest approximately equal fractions of solo, duo, or trio C-H, and little quartet C-H, consistent with what one would expect for a mixture of large symmetric compact PAHs (Stein & Brown 1991).
- The carbon skeleton has C-C-C bending modes near 6.2 and 7.7 μm

The precise position of the bands, and their relative strengths, vary from one individual PAH to another, and upon their state of ionization, but the observed spectra are in good agreement with what one might obtain from a mixture of neutral and ionized PAHs (Allamandola, Hudgins, & Sandford 1999).

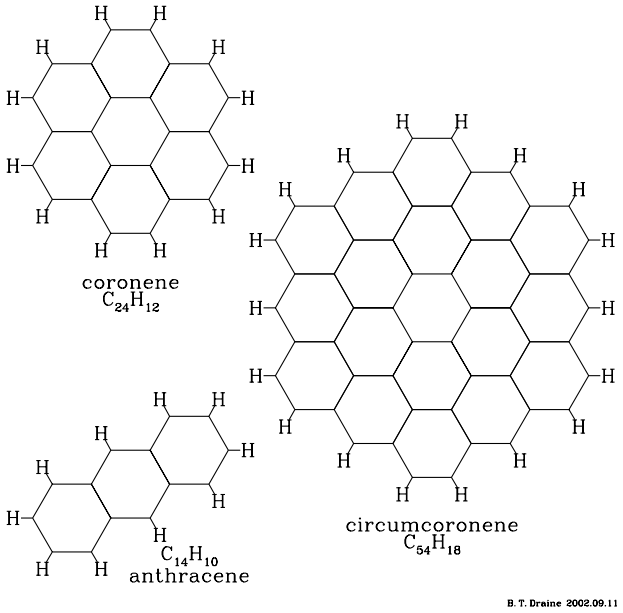

Fig. 7. Three examples of PAH molecules.

1.10 IR and FIR Emission

The energy which grains absorb from starlight is reradiated at longer wavelengths, mainly into the far-infrared. We can estimate the emission spectrum of the Galaxy using data from all-sky surveys by the IRAS and COBE satellites, and pointed observations by the Japanese IRTS satellite. At high galactic latitudes we know that most of the dust is illuminated by the local average starlight background. Theoretical studies of dust grain heating by starlight suggested that $a \gtrsim 0.01\,\mu$m interstellar grains would be heated to temperatures $15\,\mathrm{K} \lesssim T \lesssim 20\,\mathrm{K}$ by the diffuse starlight (see, e.g., Draine & Lee 1984).

Because there is little dust at high galactic latitudes, the infrared surface brightness is low, but from the correlation of infrared surface brightness with 21 cm emission one can extract the infrared emission per H atom. This has been done using photometry in the 4 IRAS photometric bands, the 9 photometric bands of the DIRBE instrument on COBE, and using the spectrophotometry by the FIRAS instrument on COBE.

The Japanese IRTS satellite obtained the 3-13 μm spectrum of the galactic plane ($l \approx 45°$, $b \approx 0$). If we assume that the 3-13 μm surface brightness is proportional to the 100 μm surface brightness, we can estimate the 3-13 μm emission per H atom. The results are shown in Figure 8. The $3 - 13\,\mu$m emission appears to be dominated by the same infrared emission features

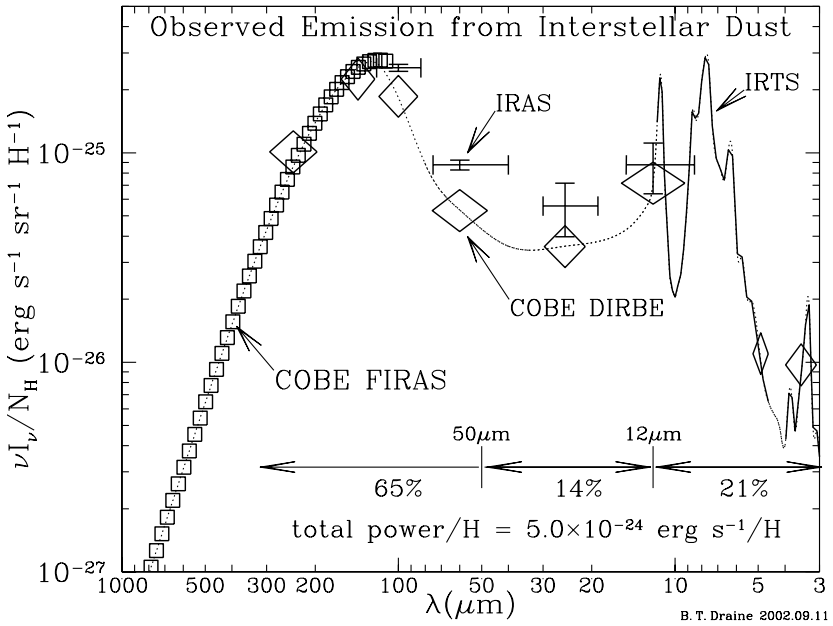

Fig. 8. Observed infrared emission per H nucleon from dust heated by the average starlight background (see text). Crosses: IRAS (Boulanger & Perault 1988); Squares: COBE-FIRAS (Wright et al. 1991); Diamonds: COBE-DIRBE (Arendt et al. 1998); Heavy Curve: IRTS (Onaka et al. 1996, Tanaka et al. 1996). The interpolated dotted line is used to estimate the total power.

observed in reflection nebulae and planetary nebulae, and widely attributed to polycyclic aromatic hydrocarbons.

If we interpolate to obtain the dotted line in Figure 8, we can numerically integrate to obtain the total infrared emission power per H nucleon $= 5.0 \times 10^{-24}\,\mathrm{erg\,s^{-1}H^{-1}}$. About 2/3 of this power is radiated at wavelengths $\lambda > 50\,\mu$m, which is where interstellar dust at $T \lesssim 20\,$K was expected to radiate. However, about 1/3 of the power is radiated at $\lambda < 50\,\mu$m, where the emission from $T < 20\,$K dust should be negligible. Furthermore, about 1/6 of the total power is radiated at $\lambda < 10\,\mu$m, primarily in 6.6, 7.7, and 8.6 μm PAH features.

1.11 Interstellar Depletions: Atoms Missing from the Gas

Narrow optical and ultraviolet absorption lines seen in absorption in stellar spectra can be used to determine interstellar gas phase abundances of many elements. While some species, such as N and S, have gas phase abundances (relative to H) which are approxiamtely solar, certain others, such as Mg, Al, Si, Ti, Ca, Fe, Ni, Cr show abundances which are far below solar. Since we

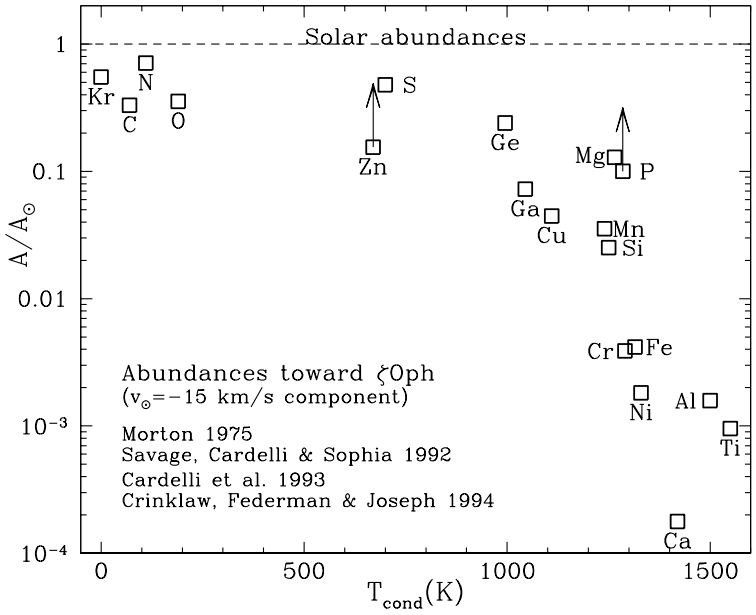

Fig. 9. Depletions in the diffuse molecular cloud toward ζOph.

presume that the interstellar abundances are approximately solar (Sofia & Meyer 2001), the atoms missing from the gas must be locked up in dust grains. In Fig. 9 the abundances have been plotted as a function of "condensation temperature" – the temperature at which cooling, solar abundance gas at LTE would begin to condense a particular element into a solid or liquid phase. Elements with $T_{\rm cond} \gtrsim 1200\,{\rm K}$ are able to form "refractory" solids with large binding energies, and it is therefore not surprising that the strongly depleted elements tend to be those with high values of $T_{\rm cond}$. The observed elemental depletions provide a clue to the composition of interstellar dust. Restricting ourselves to abundant elements, we see that the "electron donor" species in interstellar dust material must be predominantly C, Mg, Si, and Fe. The grains could contain a significant amount of O, and perhaps H.

1.12 A Provisional Grain Model

Below we will be discussing the astrophysics of interstellar dust. It is helpful to have a specific grain model in mind so that one can carry out calculations. Accordingly, here we describe briefly a grain model which appears to be consistent with observations. The model consists of a mixture of carbonaceous particles and silicate particles. The carbonaceous particles have the physical and optical properties of polycyclic aromatic hydrocarbon molecules when they are small $a < 50$Å, or $N_{\rm C} \lesssim 6 \times 10^4$ carbon atoms. When they are

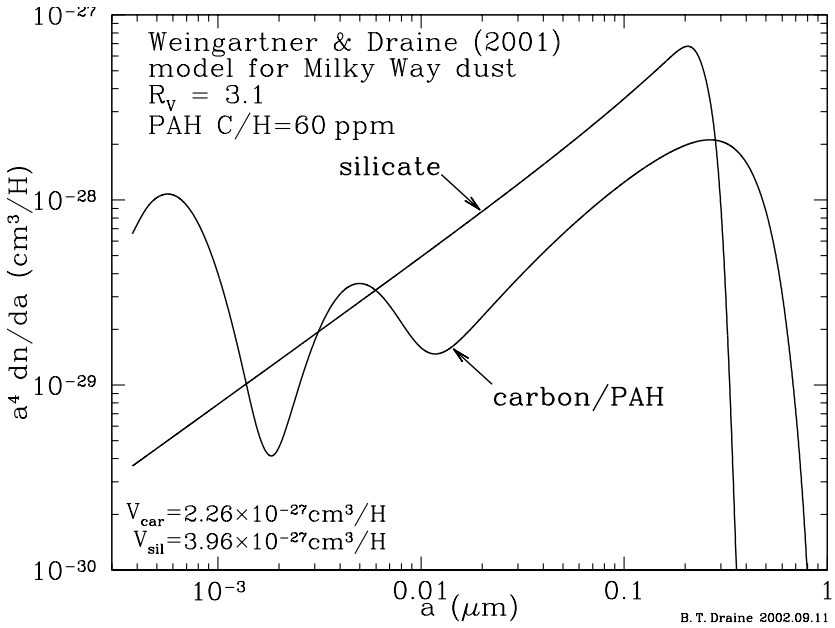

Fig. 10. WD01 size distribution for dust consistent with an $R_V = 3.1$ extinction curve for the local Milky Way. The quantity plotted – $a^4 dn/da$ – is proportional to the dust volume per logarithmic size interval.

larger, the carbonaceous grains are assumed to have the optical properties of randomly-oriented graphite spheres. The silicate grains are assumed to be amorphous silicates.

The emission in the $3 - 12\,\mu$m region from the diffuse ISM is attributed to dust grains small enough that a single starlight photon can raise the vibrational temperature high enough for thermal emission in the observed vibrational modes. In order for this emission to amount for $\sim 21\%$ of the total radiated power, very large numbers of very small dust grains are required. Li & Draine (2001) estimate that $\sim$15% of the total carbon abundance must be in carbonaceous particle containing $< 10^3$ C atoms. Since these particles must account for $\sim$20% of the total absorption of starlight, it is obvious that they must make a signficant contribution to the interstellar extinction curve.

Weingartner & Draine (2001a, hereafter WD01) have shown that there are dust size distributions which include the required large numbers of ultrasmall carbonaceous grains and which are compatible with the observed extinction curves for various regions in the Milky Way, LMC, and SMC galaxies. The size distributions are by no means unique – the observed extinction curve cannot be "inverted" – but they are nevertheless strongly constrained, so the WD01 size distributions are probably not too far from the truth. Figure 10

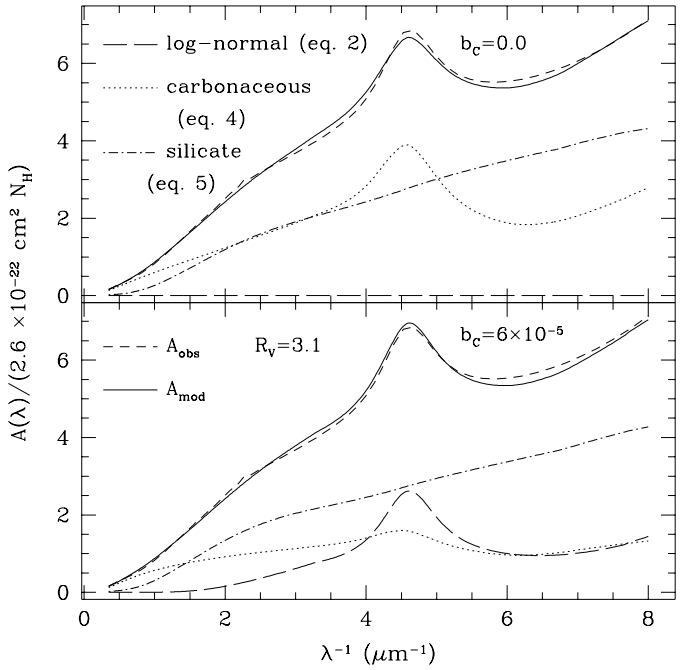

Fig. 11. Dashed line: average diffuse cloud extinction curve. Solid lines: model extinction curve for two extreme values of the ultrasmall carbonaceous grain abundance: $b_C = 0$ (no PAHs) and $b_C = 60$ppm C in PAHs. For each case the size distribution of carbonaceous and silicate grains was adjusted to obtain good overall agreeement with the observed extinction. From Weingartner & Draine (2001a).

shows a grain size distribution appropriate for diffuse clouds in the local Milky Way. The total mass in grains with $a \lesssim 100$Å is constrained by the observed extinction in the ultraviolet, but since these grains are in the "Rayleigh limit" the extinction is virtually independent of the actual sizes and numbers of these particles, provided only that the constraint on the total volume of these grains is satisfied.

The size distribution for $a \lesssim 15$Å carbonaceous grains is adjusted to make the predicted infrared emission agree with observations. The bimodal nature of the carbonaceous size distribution for $a \lesssim 100$Å is probably an artifact of the fitting procedure.

1.13 Far-Infrared and Submm Opacities

If dust grains in a cloud have a temperature T_d, the emergent intensity is

$$I_\nu = B_\nu(T_d)\left[1 - e^{-\tau_d}\right] \quad , \tag{2}$$

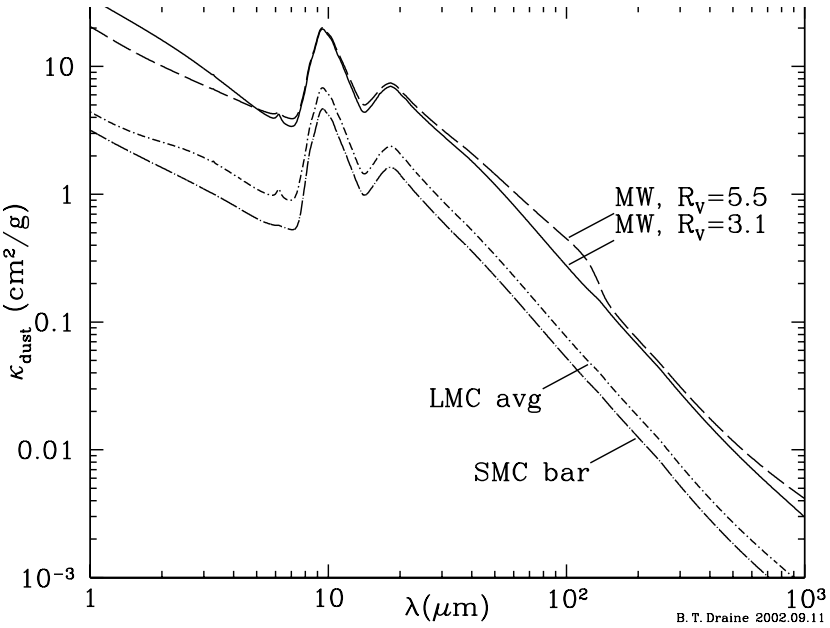

Fig. 12. Opacities $\kappa(\lambda)$ = (dust absorption cross section)/(mass of gas + dust) for Milky Way dust with $R_V = 3.1$ and $R_V = 5.5$, LMC average dust, and dust in the SMC bar, computed for the carbonaceous/silicate dust model (Weingartner & Draine 2001a; Li & Draine 2001).

$$\tau_d(\lambda) = \kappa(\lambda) \int \rho \; ds \quad , \tag{3}$$

where the dust opacity

$$\kappa(\lambda) = \frac{1}{1.4 n_{\rm H} m_{\rm H}} \int da \frac{dn_d}{da} C_{\rm abs}(a,\lambda) \quad , \tag{4}$$

ρ is the total mass density (gas + dust), and we have assumed $n_{\rm He}/n_{\rm H} = 0.1$. Dust opacities κ are given in Fig. 12; these opacities are also available at http://www.astro.princeton.edu/~draine/dust/dust.html.

At long wavelengths the optical depth $\tau_d \ll 1$. If we can estimate the dust temperature, the cloud mass per area can be obtained from the observed intensity I_ν by

$$\int \rho \; ds \approx \frac{1}{\kappa(\lambda)} \frac{I_\nu}{B_\nu(T_d)} \quad . \tag{5}$$

The derived mass density depends sensitively on the value of T_d unless one is in the Rayleigh-Jeans limit, $\lambda \gtrsim hc/kT_d$, in which case $\int \rho \, ds \propto T_d^{-1}$.

2 Optics of Interstellar Dust Grains

Our knowledge of interstellar dust is based in large part on the interaction of dust grains with electromagnetic radiation: absorption, scattering, and emission. The interaction of electromagnetic radiation with a "target" will depend on the composition of the target (which determines the "response" of the target material to applied electric and magnetic fields) and the geometry of the target – both the shape and the size. Lacking definite knowledge of both the composition and the grain geometry, we must make some assumptions to proceed.

2.1 Cross Sections, Scattering Matrices, and Efficiency Factors

We are generally interested in calculating the following quantities for unpolarized plane waves incident on the target:

- $C_{\rm abs}$ = the total absorption cross section.
- $C_{\rm sca}$ = the total scattering cross section.
- $dC_{\rm sca}/d\Omega$ = differential scattering cross section. This is related to the Muller matrix element S_{11} by $dC_{\rm sca}/d\Omega = S_{11}/k^2$, where $k = 2\pi/\lambda$.
- polarization P for the radiation scattered in a particular direction.

In some cases we wish to explicitly consider polarized light. For this case the Stokes vector for the scattered radiation is obtained by multiplying the Stokes vector of the incident radiation by the 4×4 Mueller scattering matrix S_{ij}. The 4×4 scattering matrix (which, for a fixed grain, is a function of direction of incidence and direction of scattering) fully characterizes the scattering properties of a grain. See Bohren & Huffman (1983) or Mishchencko, Hovenier, & Travis (2000) for discussions of scattering concepts.

It is convenient to normalize scattering and absorption cross sections by dividing them by a geometric cross section. In the case of spherical target of radius a, the standard convention is to simply divide by the geometric cross section πa^2. In the case of nonspherical targets, there is more than one convention in use. Some authors divide by the geometric cross section of the target as seen from the direction of the illumination. Other authors divide by the average geometric cross section for random orientations.

My preference is to normalize by dividing by the geometric cross section of an "equal volume sphere". Thus for a target of mass M, and made of a material with density ρ, the volume is $V = M/\rho$, and we define "efficiency factors" $Q_{\rm sca}$, $Q_{\rm abs}$, $Q_{\rm ext} \equiv Q_{\rm sca} + Q_{\rm abs}$ by

$$Q = \frac{C}{\pi a_{\rm eff}^2} \quad \text{where} \quad a_{\rm eff} \equiv \left(\frac{3V}{4\pi}\right)^{1/3} \quad . \tag{6}$$

2.2 Grain Geometry?

Since interstellar dust is able to polarize starlight, we know that at least some interstellar dust grains must be appreciably nonspherical. Nevertheless, for many purposes we will approximate dust grains as spheres for the simple reason that we can use "Mie theory" to calculate scattering and absorption of light by spherically-symmetric targets with sizes comparable to the wavelength. Exact series solutions have been found for spheroids (Asano & Yamamoto 1975, Asano & Sato 1980; Voshchinnikov & Farafonov 1993) but numerical calculations are much more challenging than for spheres. Solutions for other shapes (other than the unphysical case of infinite cylinders) are not available.

2.3 Dielectric Functions

First, a few words about conventions: We will follow c.g.s. electromagnetism, so that $\epsilon = \mu = 1$ for the vacuum. We will represent plane waves as proportional to $e^{ikx-i\omega t}$; with this convention, absorption corresponds to $\mathrm{Im}(\epsilon) > 0$.

When an electric field is applied to a material, there are two distinct types of response possible: the response of the *bound* charge and the *free* charge. The *bound* charge (e.g., electrons and nucleus within an atom) undergoes a finite displacement when the electric field is applied, with the individual atoms or molecules acquiring an electric dipole moment in response to the applied electric field. The response of the bound charge is characterized by a complex dielectric function $\epsilon^{(bound)}(\omega)$.

The *free* charge responds in the form of an electric current density, $J = \sigma E$, where $\sigma(\omega)$ is the electrical conductivity.

When dealing with a monochromatic electric field it is convenient to define a dielectric function ϵ describing the response of both bound and free charge:

$$\epsilon = \epsilon^{(bound)}(\omega) + \frac{4\pi i\sigma(\omega)}{\omega} \quad . \tag{7}$$

With this definition, the free charge current J is now absorbed into the displacement current $(1/4\pi)\partial D/\partial t$, so that Maxwell's equation becomes

$$\nabla \times B = \frac{1}{c}\frac{\partial D}{\partial t} \quad , \tag{8}$$

where $D = \epsilon E$.

2.3.1 A Model Insulator

It is instructive to consider a simple classical model for the dielectric response of an insulator. Suppose the insulator consists of "molecules", with no permanent dipole moment, but which can be polarized in response to the local applied electric field plus the electric field from all of the other polarized molecules. The dipole moment of a molecule is qx, where x is the

displacement of the bound charge q. Suppose the displacement x behaves like a driven, damped harmonic oscillator,

$$m\ddot{x} = qE - m\omega_0^2 x - m\dot{x}/\tau_0 \quad , \tag{9}$$

where ω_0 is the resonant frequency, and τ_0 is a damping time. For a periodic electric field $E \propto e^{-i\omega t}$ we can readily solve for the molecular polarizability $\alpha = qx/E$:

$$\alpha(\omega) = \frac{\alpha_0}{1 - (\omega/\omega_0)^2 - i\omega/(\omega_0^2\tau_0)} \quad , \tag{10}$$

where

$$\alpha_0 \equiv \frac{q^2}{m\omega_0^2} \tag{11}$$

is the zero-frequency polarizability of the molecule. We now consider a medium consisting of a number density n of such molecules. Each now responds to the externally applied electric field plus the electric field due to all of the other polarized molecules. In the low frequency limit, the effective dielectric function ϵ of the medium is related to the molecular polarizability through the famous Clausius-Mossotti relation (see, e.g., Jackson 1975)

$$\epsilon = 1 + \frac{4\pi n\alpha}{1 - (4\pi/3)n\alpha} \quad . \tag{12}$$

For molecules on a cubic lattice, the Clausius-Mossotti relation (12) is exact in the limit $|m|kd \ll 1$, where $d \equiv n^{-1/3}$ is the intermolecular spacing and $k \equiv \omega/c$. For finite kd, corrections to $O[(kd)^3]$ have been derived by Draine & Goodman (1993). Substituting (10) into (12) we obtain

$$\epsilon = 1 + \frac{4\pi n\alpha_0}{1 - (4\pi/3)n\alpha_0 - (\omega/\omega_0)^2 - i\omega/(\omega_0^2\tau_0)} \quad . \tag{13}$$

In the low frequency limit $\omega \to 0$, we have

$$\mathrm{Re}(\epsilon^{(bound)}) \to \epsilon_0^{(bound)} \equiv 1 + \frac{4\pi\alpha_0}{1 - (4\pi/3)\alpha_0} \quad , \tag{14}$$

from which we note that

$$4\pi\alpha_0 = 3\left[\frac{\epsilon_0^{(bound)} - 1}{\epsilon_0^{(bound)} + 2}\right] \quad . \tag{15}$$

At low frequencies, the imaginary part of $\epsilon^{(bound)}$ varies linearly with frequency:

$$\mathrm{Im}(\epsilon^{(bound)}) \approx A\omega \quad , \tag{16}$$

$$A = \frac{3}{\omega_0^2\tau}\frac{\epsilon_0^{(bound)} - 1}{\epsilon_0^{(bound)} + 2} \quad . \tag{17}$$

An insulator has no mobile charges ($\sigma = 0$), and for our model at low frequencies we have

$$\mathrm{Re}\,(\epsilon) \rightarrow \epsilon_0^{(bound)} = const \quad , \tag{18}$$

$$\mathrm{Im}\,(\epsilon) \rightarrow A\omega \quad . \tag{19}$$

2.3.2 A Model Conductor

For a material with a density n_e of free electrons, a simple classical model for the electron dynamics would be

$$m_e\ddot{x} = eE - m_e\dot{x}/\tau_e \quad , \tag{20}$$

where τ_e is the electron collision time. With this equation of motion, the conductivity $\sigma(\omega) \equiv n_e e\dot{x}/E$ is just

$$\sigma(\omega) = \frac{\sigma_0}{1 - i\omega\tau_e} \quad , \tag{21}$$

where

$$\sigma_0 = n_e e^2 \tau_e / m_e = \frac{\omega_p^2 \tau_e}{4\pi} \quad , \tag{22}$$

where σ_0 is the d.c. conductivity, and $\omega_p \equiv (4\pi n_e e^2/m_e)^{1/2}$ is the plasma frequency. For this case, the low-frequency behavior of ϵ is

$$\mathrm{Re}\,(\epsilon) \rightarrow \epsilon_0^{(bound)} - 4\pi\sigma_0\tau_e = const \quad , \tag{23}$$

$$\mathrm{Im}\,(\epsilon) \rightarrow A\omega + \frac{4\pi\sigma_0}{\omega} \quad . \tag{24}$$

Comparing (19) and (24), we see that the low-frequency behavior of Imϵ is qualitatively different for an insulator or for a conductor. Below we will see what this implies for the frequency-dependence of the absorption by small particles.

2.4 Calculational Techniques

In many astrophysical applications we are concerned with particles which are neither very small nor very large compared to the wavelength of the incident radiation. There are several different methods which can be used to calculate scattering and absorption cross-sections by targets which are neither very large nor very small compared to the wavelength:

- Mie theory solution for spherical targets (Bohren & Huffman 1983). Mie theory codes are highly-developed and readily available. They break down due to numerical roundoff error when the target becomes too large compared to the wavelength. A modified version of the Bohren & Huffman code is available at
  http://www.astro.princeton.edu/~draine/scattering.html

- Series solution for homogeneous spheroid or layered spheroid (boundaries must be confocal spheroids) (Asano & Yamamoto 1975; Asano & Sato 1980; Voshchinnikov & Farafonov 1993). Codes for spheroids have been developed but have not been widely used. Codes based on the Asano & Yamamoto treatment had a reputation for being somewhat numerically delicate (Rogers & Martin 1979). Voshchinnikov & Farafanov (1993) have developed a treatment based upon separation of variables which is reported to be more robust. They have recently generalized this to core-mantle spheroidal targets (Farafanov, Voshchinnikov, & Somsikov 1996).
- Extended Boundary Condition Method (EBCM), often referred to as the "T-matrix method" (Mishchenko, Travis & Macke 2000). The EBCM method (Mischchenko, Travis & Macke 2000) is used to construct the "T matrix" which gives the coupling between vector spherical harmonic components of the incoming wave and vector spherical harmonic components of the scattered wave. Once the T-matrix has been obtained, orientational averages can be efficiently calculated. The EBCM method appears to be well-suited to targets with rotational symmetry which are not extremely elongated. EBCM T-matrix codes have been made available by M. Mishchenko at http://www.giss.nasa.gov/~crmim/t_matrix.html
- Discrete Dipole Approximation (Draine & Flatau 1994; Draine 2000). The Discrete Dipole Approximation can be quite readily applied to complex geometries. It has been used to calculate the optical properties of graphite particles, with a highly anisotropic dielectric tensor (Draine 1988; Draine & Malhotra 1993). In recent years it has been accelerated by use of FFT techniques (Goodman, Draine, & Flatau 1991), and its accuracy has been improved by refinements in the assignment of dipole polarizabilities (Draine & Goodman 1993). The Fortran code DDSCAT is available from http://www.astro.princeton.edu/~draine/DDSCAT.html , and a detailed User Guide is available (Draine & Flatau 2000).

2.5 Scattering by Homogeneous Isotropic Spheres

The solution to Maxwell's equations for a plane wave incident on a homogeneous and isotropic sphere was independently obtained by Mie (1908) and Debye (1909). The solution – now generally referred to as "Mie theory" – is given in terms of a series expansion in powers of the "size parameter" $x \equiv 2\pi a/\lambda$. The expansion converges, but the number of terms which must be retained is of $O(x)$. The details of the Mie theory solution are nicely described in the excellent monograph by Bohren & Huffman (1983). There are a number of computer codes to evaluate the absorption cross section and differential scattering cross sections given by Mie scattering theory. When x is large, care must be taken to avoid errors due to finite precision arithmetic in numerical evaluation of the series solution.

For an incident monochromatic plane wave, the full Mie theory solution depends on the dielectric function $\epsilon(\omega)$ – describing the electric polarization

of the material in response to an applied electric field oscillating at angular frequency ω – and the magnetic permeability function $\mu(\omega)$ – characterizing the magnetization of the material in response to an applied oscillating magnetic fields. Because the magnetic response is generally negligible (i.e., $|\mu - 1| \ll |\epsilon - 1|$) at frequencies above 100 GHz) it is customary to neglect the magnetization of the grain material except insofar as it is due to eddy currents.

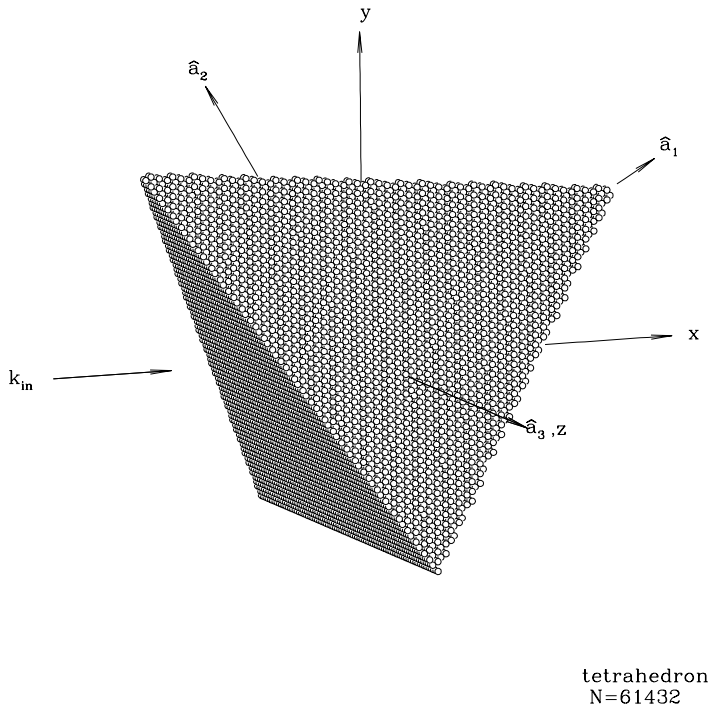

Fig. 13. Representation of a tetrahedron with a dipole array. The dipoles are actually pointlike – here they are represented by small spheres for purposes of visualization. We consider incident radiation propagating along the direction of the vector $\mathbf{k}_{\rm in}$ illustrated here. Taken from Draine (2000).

2.6 Discrete Dipole Approximation

The discrete dipole approximation consists in replacing the (continuum) target of specified dielectric function ϵ with an array of polarizable points (referred to as "dipoles"). The array geometry is chosen to mimic the target geometry. The polarizabilities α of the points are chosen so that an infinite

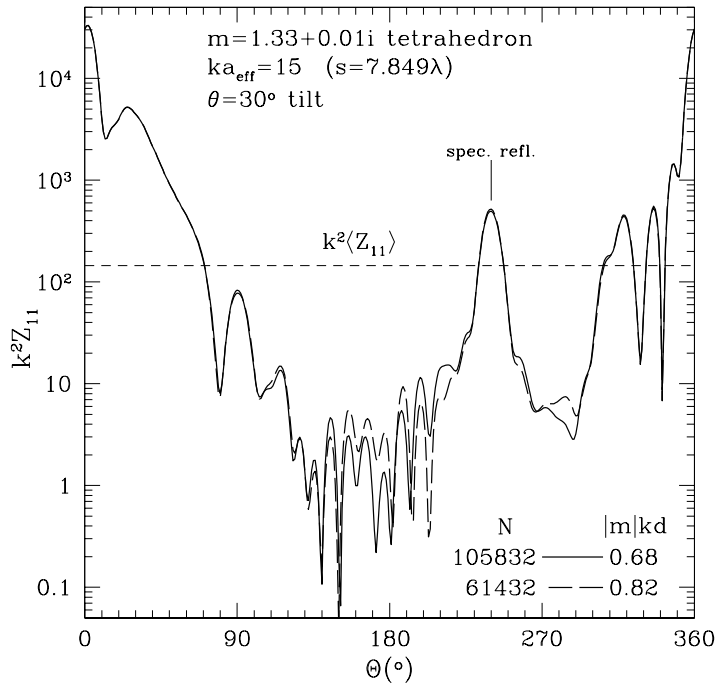

Fig. 14. $S_{11} = k^2 dC_{\rm sca}/d\Omega$ for scattering of unpolarized light bya tetrahedron, for scattering directions in the x-y plane (see Fig. 13), as a function of scattering angle Θ. The tetrahedron has refractive index $m = 1.33 + 0.01i$, has edges of length $s = 7.849\lambda$, where λ is the wavelength of the incident light in vacuo, and is oriented with an angle $\theta = 30^\circ$ between $\mathbf{k}_{\rm in}$ and $\hat{\mathbf{a}}_1$. The peak at $\Theta = 240^\circ$ corresponds to the direction of specular reflection for geometric optics. Results are shown for a tetrahedron represented by $N = 61432$ and $N = 105832$ dipoles. The scattered intensities are in excellent agreement in all directions where the scattering is at all strong. The dashed line shows $k^2\langle Z_{11}\rangle = C_{\rm sca}/4\pi$. Taken from Draine (2000).

lattice of such polarizable points would have the same dispersion relation as the material of dielectric function ϵ (Draine & Goodman 1993). With FFT techniques employed to speed the calculation, it is now feasible to calculate scattering and absorption by targets represented by more than 100,000 polarizable dipoles on a workstation with 256 MB of RAM. There are great efficiencies if the dipoles are situated on a cubic lattice, so DDSCAT requires that this be the case.

The DDA can be applied to inhomogeneous targets and targets with complex geometries. As an example of the type of problem which can be solved, in Fig. 13 we show a discrete-dipole array of 61432 dipoles intended to approximate a tetrahedral target. In Fig. 14 we show the calculated scattered

intensity in the x-y plane as a function of scattering angle Θ. Notice the pronounced scattering peak at $\Theta = 240°$ – this is the direction where one would have a specular reflection peak in the geometric optics limit.

For a fixed target size D, complex refractive index m, and wavelength λ, the DDA converges to the exact answer in the limit where the interdipole separation $d \to 0$: the target structure is well-resolved and the dipole separation is small compared to the wavelength in the target material. The criterion for separation small compared to λ can be written $|m|kd \lesssim 1$. If $|m|$ is not too large, we find that the overall scattering and absorption cross section is calculated fairly accurately provided $|m|kd \lesssim 1$; the detailed scattering pattern will be calculated accurately if $|m|kd \lesssim 0.5$. For example, the two calculations in Fig. 14, with $|m|kd = 0.82$ and 0.68, are already in fairly good agreement.

2.7 Infrared and Far-Infrared

When the wavelength is long compared to the target size, we may use the "dipole approximation" (Draine & Lee 1984) and characterize the response of the target to the incident electromagnetic field purely in terms of the (oscillating) electric and magnetic dipole moments of the target. We may write

$$C_{\rm abs} = \frac{4\pi\omega}{c}\left[{\rm Im}(\alpha_E^e) + {\rm Im}(\alpha_H^m)\right] \quad , \tag{25}$$

$$C_{\rm sca} = \frac{8\pi}{3}\left(\frac{\omega}{c}\right)^4\left[|\alpha_E^e|^2 + |\alpha_H^m|^2\right] \quad , \tag{26}$$

where α_E^e is the (complex) electric polarizability along the direction of the incident electric field vector, and α_H^m is the (complex) magnetic polarizability along the direction of the incident magnetic field vector.

Consider a homogeneous ellipsoidal particle composed of an isotropic material, with semiaxes a, b, c. If the applied electric field is along one of its principal axes, the electric polarizability is

$$\alpha_E^e = \frac{V}{4\pi}\frac{\epsilon - 1}{(\epsilon - 1)L_E + 1} \quad , \tag{27}$$

where L_E is the "shape factor" along the direction of the applied E field, and $V = 4\pi abc/3$ is the volume of the ellipsoid. The shape factors along the three principal axes satisfy the sum rule $L_1 + L_2 + L_3 = 1$ and may be obtained by numerical quadrature (Bohren & Huffman 1983).

Consider now a spheroid with semiaxes a, b, b (prolate if $a/b > 1$, oblate if $a/b < 1$). For this case we have analytic expressions for the shape factors L_a and $L_b = (1 - L_a)/2$. For a prolate spheroid ($a < b$) we have (van de Hulst 1957)

$$L_a = \frac{1 - e^2}{e^2}\left[\frac{1}{2e}\ln\left(\frac{1+e}{1-e}\right) - 1\right] \quad , \tag{28}$$

and for an oblate spheroid ($a < b$) we have

$$L_a = \frac{1+e^2}{e^2}\left[1 - \frac{1}{e}\arctan(e)\right] \quad , \tag{29}$$

where

$$e^2 \equiv |1-(b/a)^2| \quad . \tag{30}$$

Exact solutions for α_E^e in the limit $\lambda \gg a_{\rm eff}$ are also available for layered grains provided the interfaces are confocal spheroids (Gilra 1972; Draine & Lee 1984).

For spheres we have $L_a = L_b = 1/3$, and

$$C_{\rm abs} = \frac{9\omega V}{c}\frac{\epsilon_2}{(\epsilon_1+2)^2+\epsilon_2^2} \quad , \tag{31}$$

where $\epsilon_1 \equiv {\rm Re}(\epsilon)$ and $\epsilon_2 \equiv {\rm Im}(\epsilon)$.

Eq. (31) contains an important result: the absorption cross section of a grain with size $\ll \lambda$ is simply proportional to the grain volume! The far-infrared opacity therefore depends only on the total volume of grain material present, but not on the sizes of the particles, provided only that they are small compared to the wavelength λ.

How do we expect the absorption cross section to depend on frequency ω at low frequencies? For an insulator, from (19) we see that

$$C_{\rm abs} \rightarrow \frac{9V}{c}\frac{A}{(\epsilon_0+2)^2} \quad \omega^2 \quad , \tag{32}$$

while for a conductor, we see from (24) that

$$C_{\rm abs} \rightarrow \frac{9V}{c}\left(\frac{1}{4\pi\sigma_0}\right) \quad \omega^2 \quad . \tag{33}$$

Thus we see that for both insulating grains and conducting grains, a simple physical model leads to $C_{\rm abs} \propto \omega^2$ at low frequencies! This is the basis for the expectation that dust opacities should vary as λ^{-2} in the far-infrared, as in the dust models of Draine & Lee (1984).

Now the above discussion has been based on simple classical models for the response of charge to applied electric fields. Real materials obey quantum mechanics, so results may differ. Furthermore, the above discussion assumed that $\omega \ll \omega_0$ in discussion of the response of the bound charge, but an amorphous material could have very low frequency vibrational modes, so that the assumption that $\omega \ll \omega_0$ might not be valid in the far-infrared. This might explain why some laboratory studies of amorphous materials find different behavior: for example, Agladze et al. (1996) find that the absorption coefficient for amorphous $MgO{\cdot}2SiO_2$ varyies as $\omega^{1.2}$ between 800 μm and 4 mm.

Nature must be our guide, but it is worth keeping in mind that opacities varying as ω^2 emerge naturally from simple models.

2.8 Kramers-Kronig Relations

Purcell (1969) pointed out that the Kramers-Kronig relations can provide useful constraints in dust modelling. The Kramers-Kronig relations are general relations which apply to "linear response functions", such as a dielectric function, which specifies the response (e.g., the electric polarization) to an applied stress (e.g., an applied electric field). The *only* assumptions are that (1) the response is linear, and (2) the system is causal – the response can depend on the stress applied in the past, but cannot depend upon the future. With these very simple assumptions, it is possible to derive the Kramers-Kronig relations (see Landau & Lifshitz 1960 for a nice derivation). In the case of the dielectric function, the Kramers-Kronig relations are

$$\epsilon_1(\omega_0) = 1 + \frac{2}{\pi} P \int_0^\infty d\omega \frac{\omega \epsilon_2(\omega)}{\omega^2 - \omega_0^2} \quad , \tag{34}$$

$$\epsilon_2(\omega_0) = \frac{2}{\pi} \omega_0 P \int_0^\infty d\omega \frac{\epsilon_1(\omega)}{\omega_0^2 - \omega^2} \quad , \tag{35}$$

where P indicates that the principal value is to be taken.

Thus the real and imaginary parts of $\epsilon(\omega)$ are by no means independent – if either one is known at all frequencies, the other is fully determined. In order to have a physically acceptable dielectric function, one approach (see, e.g., Draine & Lee 1984) is to specify ϵ_2 at all frequencies, and then construct $\epsilon_1(\omega)$ using (34).

2.9 Kramers-Kronig Relations for the ISM

Purcell showed that one could apply the Kramers-Kronig relations directly to the interstellar medium. Plane waves propagate through the interstellar medium but are attenuated by scattering and absorption. One can describe this attenuation by an imaginary component of the dielectric constant $\tilde{\epsilon}$ of the interstellar medium, where $|\tilde{\epsilon} - 1| \ll 1$.

Recall that for a electromagnetic plane wave of frequency ω, the wave vector is $k = m(\omega)\omega/c$, where $m(\omega) = \sqrt{\epsilon}$ is the complex refractive index. The electric field intensity decays as

$$E \propto \exp\left[-\mathrm{Im}(k)x\right] = \exp\left[-(1/2)\mathrm{Im}(\tilde{\epsilon})\omega/c\right] \quad . \tag{36}$$

The energy in the wave is proportional to $|E|^2$ and therefore decays twice as rapidly as E. Thus

$$n_{gr} C_{\rm ext}(\lambda) = \frac{\omega}{c} \tilde{\epsilon}_2 \quad . \tag{37}$$

We can now apply the Kramers-Kronig relation (34) to obtain the real part of the dielectric function $\tilde{\epsilon}$ of the ISM at zero frequency:

$$\tilde{\epsilon}_1(0) - 1 = \frac{2}{\pi} \int_0^\infty \frac{d\omega}{\omega} \frac{c}{\omega} n_{gr} C_{\rm ext}(\omega) \quad . \tag{38}$$

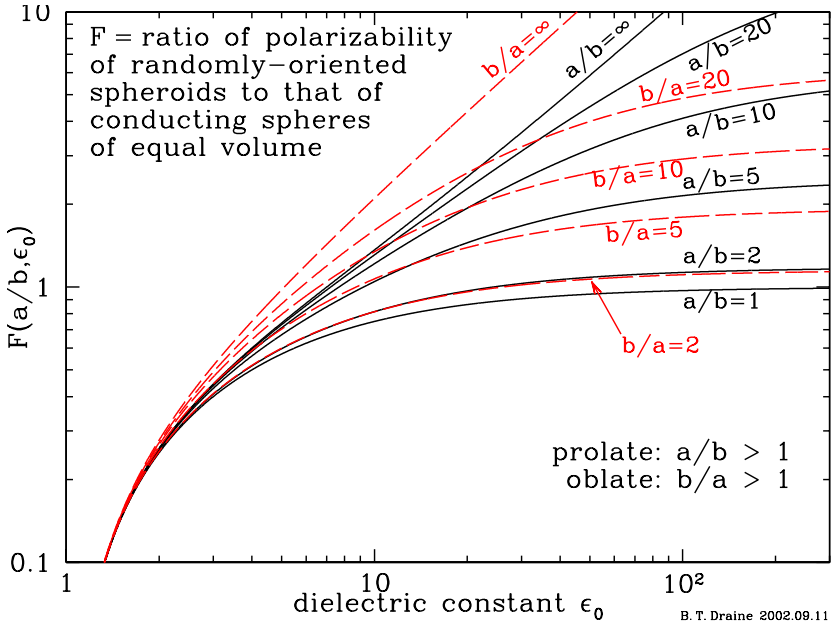

Fig. 15. Function $F(a/b, \epsilon_g)$ as a function of the static dielectric constant ϵ_0, for selected values of axial ratio a/b. After Purcell (1969).

The static dielectric function of the ISM is directly related to the electric polarizability α_{gr} of the grains in it:

$$\tilde{\epsilon}_1(0) - 1 = 4\pi n_{gr} \alpha_{gr}(0) \quad . \tag{39}$$

Thus

$$4\pi n_{gr} \alpha_{gr}(0) = \frac{2}{\pi} c n_{gr} \int_0^\infty d\omega \frac{1}{\omega^2} C_{\rm ext}(\omega) \tag{40}$$

$$= \frac{1}{\pi^2} n_{gr} \int_0^\infty d\lambda \; C_{\rm ext}(\lambda) \quad . \tag{41}$$

We have seen above how the static polarizability of a spheroidal grain depends on its volume, shape, and dielectric function. Averaged over random orientation, we have (for a dielectric grain)

$$4\pi \alpha_{\rm gr}(0) = 3V F(a/b, \epsilon_0) \quad , \tag{42}$$

$$F(a/b, \epsilon_0) \equiv \frac{(\epsilon_0 - 1)}{3} \left[\frac{1}{(\epsilon_0 - 1) 3L_a + 3} + \frac{2}{(\epsilon_0 - 1) 3L_b + 3} \right] \quad . \tag{43}$$

F is just the orientationally-averaged polarizability relative to the polarizability of an equal-volume conducting sphere. Using (42), we obtain the grain

volume per H atom in terms of an integral over the extinction per H atom:

$$\frac{n_{gr}V}{n_{\rm H}} = \frac{1}{3\pi^2 F}\int_0^\infty d\lambda\ \frac{n_{gr}}{n_{\rm H}}C_{\rm ext}(\lambda) \tag{44}$$

Now consider a conducting material. From (23-24) we see that $\epsilon \to i\times\infty$, so that

$$F \to \frac{1}{9L_a} + \frac{2}{9L_b} \tag{45}$$

so that a conducting sphere ($L_a = L_b = 1/3$) has $F(a/b = 1, \epsilon_0 = \infty) = 1$.

We do not know the grain shape, and we do not know the static dielectric constant ϵ_0. However, from Figure 15 we see that $F < 1.5$ unless the grain is *extremely* elongated ($a/b > 20$ or $b/a > 20$) *and* the static dielectric function is very large ($\epsilon_0 > 10$) – as for a metal. For a reasonable grain shape (e.g., $0.5 < a/b < 2$) and dielectric function $\epsilon_0 \approx 3$ we have $F \approx 0.4$.

Purcell's analysis is a delight, and has two important consequences:

2.9.1 Grain volume per H

It is of course not possible to measure the extinction per H atom at wavelengths from 0 to ∞. However, since $C_{\rm ext} > 0$, measurements over a finite wavelength range can be used to obtain a lower bound on $FVn_{gr}/n_{\rm H}$. The extinction per H nucleon is fairly well-known from $0.1\,\mu$m to $30\,\mu$m; a numerical evaluation gives

$$\int_{0.1\,\mu{\rm m}}^{30\,\mu{\rm m}} \frac{\tau_{\rm ext}(\lambda)}{N_{\rm H}}d\lambda \approx 1.1\times10^{-25}\,{\rm cm}^3/{\rm H} \quad . \tag{46}$$

Approximately 50% of the integral is contributed by wavelengths $0.1 < \lambda < 1\,\mu$m. If we estimate $F \approx 0.4$ this gives

$$\frac{n_{gr}V}{n_{\rm H}} \gtrsim 9.3\times10^{-27}\,{\rm cm}^3/{\rm H} \quad , \tag{47}$$

or, for an assumed grain mass density $\rho = 2.5\,{\rm g\,cm}^{-3}$ (intermediate between graphite and silicate) we have a lower bound on the ratio of grain mass to H mass:

$$\frac{M_{gr}}{M_{\rm H}} \gtrsim .014 \quad . \tag{48}$$

2.9.2 Asymptotic Behavior of $C_{\rm ext}$ at Long Wavelengths

Eq. (44) tells us that $\int_0^\infty C_{\rm ext}(\lambda)d\lambda$ must be convergent, and therefore that $C_{\rm ext}(\lambda)$ *must* decline more rapidly than $1/\lambda$: grain models in which $C_{\rm ext} \propto 1/\lambda$ for $\lambda \to \infty$ are unphysical. It is of course possible to have $d\ln C_{\rm ext}/d\ln\lambda \approx -1$ over a limited range of wavelengths, but this cannot be the asymptotic behavior.

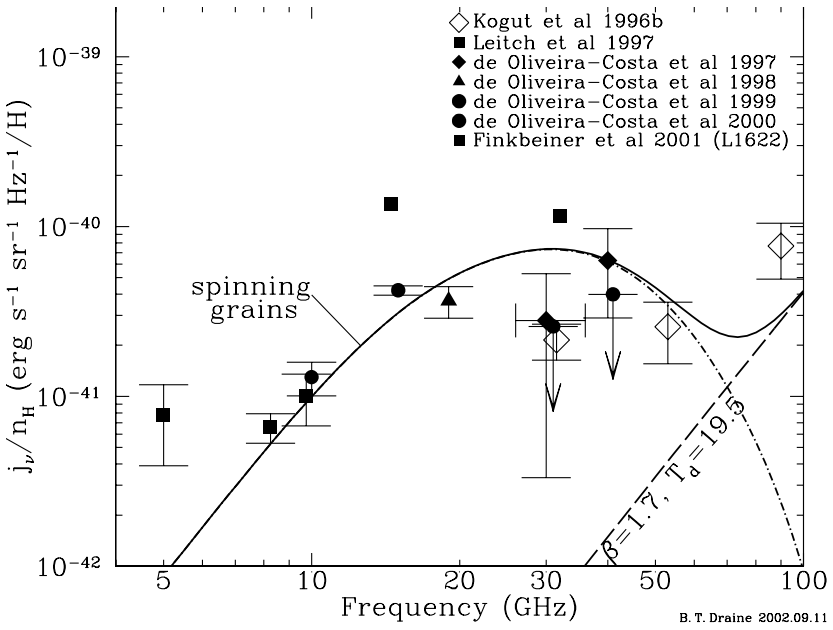

Fig. 16. Microwave sky brightness correlated with 100 μm emission. Shown is the estimated microwave emissivity per unit H nucleon.

2.10 Microwave

Dust grains would be expected to radiate thermally at microwave frequencies, but this emission was expected to be quite weak, based on an extrapolation from the thermal emission peak at $\sim 100\,\mu$m. It was therefore a surprise when sensitive maps of the microwave sky brightness (for the purpose of studying angular structure in the cosmic background radiation) showed relatively strong emission correlated with the Galactic 100 μm emission, and therefore with interstellar dust (Kogut et al. 1996a,b). Figure 16 shows the inferred microwave emissivity of per H nucleon. The dashed line labelled "$\beta = 1.7, T_d = 19.5$" is the contribution expected from thermal emission from dust grains if the dust opacity $\propto \lambda^{-1.7}$ for $\lambda \gtrsim 100\,\mu$m. We see that at 30 GHz ($\lambda = 1$ cm the observed microwave emission is two orders of magnitude above the value expected from classical dust grains.

The power radiated in the microwave is a tiny fraction of the total, so this microwave emission is not an important source of cooling. Nevertheless, we would like to know what process is responsible. Possible mechanisms include synchrotron emission from relativistic electrons, or free-free emission from a thermal plasma, but these seem unable to account for the observed 15-50 GHz emission (see Draine & Lazarian 1999b). We are left with interstellar dust.

The possibility of radio emission from rotating dust grains dates back to Erickson (1957). As discussed above, the strong infrared emission in the $3-12\,\mu$m range appears to require a very large population of very small dust grains. Ferrara & Dettmar (1994) pointed out that these dust grains would produce detectable radio emission if they were undergoing Brownian rotation at the gas temperature.

Draine & Lazarian (1998a,b) analyzed the grain rotational dynamics, and showed that the population of ultrasmall grains required to understand the infrared emission would be expected to produce microwave emission, with a predicted spectrum (and intensity) as shown in Fig. 16. We will discuss the grain dynamics in §6, but this rotational emission still seems likely to contribute a substantial fraction of the observed dust-correlated microwave emission. In principle, these rapidly spinning dust grains could be aligned, leading to polarized emission, but the polarization fraction has been estimated to be small (Lazarian & Draine 2000).

However, if dust grains contain magnetic materials – which does not seem implausible, considering the large amount of Fe in interstellar grains – there could also be *thermal* magnetic dipole emission from dust. Consider a ferromagnetic domain in a dust grain. This domain is spontaneously-magnetized: it is energetically favorable to have alignment of electron orbital angular momentum and electron spins. The lowest energy state has some specific magnetization, but there are nearby energy states where the domain has uniform magnetization with the same net magnetic moment but in a slightly different direction. In thermal equilibrium, it is possible for these higher energy states to be excited, so that the magnetization direction will fluctuate. This results in a time-varying magnetic dipole moment, and hence magnetic dipole radiation.

The optics of magnetic dust grains with size small compared to the wavelength has been developed by Draine & Lazarian (1999a; hereafter DL99a), and the magnetic susceptibility $\mu(\omega)$ was estimated for several magnetic materials, including metallic Fe and magnetite Fe_3O_4. The spectrum and intensity of this radiation was estimated by DL99a, and it was found that *if* a substantial fraction of the Fe in interstellar grains is incorporated into magnetic materials (e.g., magnetite), the resulting thermal emission could account for an appreciable fraction of the observed microwave emission!

How will we be able to distinguish between spinning dust grains and magnetic dust grains as sources of microwave emission? DL99a point out that small grains are believed to be underabundant in dense clouds (they presumably coagulate to form bigger grains), so that the rotational emissivity per H nucleon would be reduced. The magnetic dipole emission from magnetic grain materials does not, however, depend on the grain size. Hence if we see strong microwave emission from dust in dense clouds, this would suggest that magnetic dust grains may be responsible. Future pointed observations of dense clouds may answer this question.

2.11 X-rays

The scattering of X-rays by dust grains was first discussed by Overbeck (1965), Slysh (1969), and Hayakawa (1970). Because the refractive index of grain materials is close to unity at X-ray energies, the scattering is through small angles. As a result, images of X-ray point sources show a "halo" of dust-scattered X-rays. The observable halo can extend for tens of arcminutes from the source.

For sufficiently small grains, this scattering can be calculated using the Rayleigh-Gans approximation (see Bohren & Huffman 1983), which is valid if $|m-1|ka \ll 1$, where a is the grain radius. Because X-rays have large k, this condition may not be satisfied for the larger interstellar grains, in which case one should resort to full Mie theory. This can be numerically challenging because the number of terms which must be retained is of order $ka \approx 507(a/0.1\,\mu\mathrm{m})(E/\mathrm{keV})$, so high numerical accuracy is required. Smith & Dwek (1998) have compared scattering halos estimated using the Rayleigh-Gans approximation with Mie theory, and show that the Rayleigh-Gans approximation fails for energies below 1 keV. Scattering by grains with $|m-1|ka \ll 1$ and $ka \gg 1$ can be treated using "anomalous diffraction theory" (van de Hulst 1957).

Nova Cygni 1992, a bright X-ray nova, was observed by ROSAT. The observed X-ray halo has been compared to predictions for different grain models by Mathis et al. (1995), Smith & Dwek (1998), and Witt, Smith & Dwek (2001), with differing conclusions. The most recent study (Draine & Tan 2002) concludes that our standard dust model is in reasonable agreement with the observed X-ray halo. Future observations of X-ray scattering halos will be valuable to test and constrain grain models.

3 IR and Far-IR Emission from Interstellar Dust

3.1 Heating of Interstellar Dust

While dust grains can be heated by collisions with gas atoms and molecules, starlight usually is the dominant heating process. The rate of energy deposition, the rate of photon absorptions, and the mean energy per absorbed photon are

$$\langle dE/dt\rangle_{\rm abs} = \int_0^\infty d\nu\ u_\nu\ c\ C_{\rm abs}(\nu) \quad , \tag{49}$$

$$\dot{N}_{\rm abs} = \int_0^\infty d\nu \frac{u_\nu}{h\nu} c C_{\rm abs}(\nu) \quad , \tag{50}$$

$$\langle h\nu\rangle_{\rm abs} = \frac{\langle dE/dt\rangle_{\rm abs}}{\dot{N}_{\rm abs}} \quad , \tag{51}$$

where $u_\nu d\nu$ is the photon energy density in $(\nu, \nu+d\nu)$, and $C_{\rm abs}(\nu)$ is the photoabsorption cross section. We assume that all of the energy of an absorbed

photon is converted to heat; this is not exactly correct, since energetic photons may eject a photoelectron, or excite fluorescence, but these processes take away only a small fraction of the total absorbed power.

Now suppose that the dust grain has energy E distributed among its vibrational degrees of freedom. Except when the energy E is very small, the number of vibrational modes which can be excited is very large. The density of states has been discussed by Draine & Li (2001): even for a small molecule like coronene $C_{24}H_{12}$, there are $\sim 10^{20}$ different states with total energy $E < 1\,\mathrm{eV}$; for $C_{4000}H_{1000}$ this number becomes $\sim 10^{135}$. As a result, the statistical notion of "temperature" can be used, even for quite small grains: a grain with vibrational energy content E is assumed to be characterized by a temperature $T(E)$ such that if the grain were in contact with a heat bath at temperature T, the expectation value for its energy would be E.

At temperature T, the average power radiated by a grain is

$$\left(\frac{dE}{dt}\right)_{rad} = \int_0^\infty d\nu C_{\rm abs}(\nu) 4\pi B_\nu(T) \quad , \tag{52}$$

where $C_{\rm abs}(\nu)$ is the angle-averaged absorption cross section for photons of frequency ν, and

$$B_\nu(T) \equiv \frac{2h\nu^3}{c^2} \frac{1}{e^{h\nu/kT} - 1} \tag{53}$$

is the Planck function.

It is now natural to determine the "steady-state" temperature $T_{\rm ss}$ at which the power radiated equals the power absorbed:

$$\int_0^\infty d\nu C_{\rm abs}(\nu) 4\pi B_\nu(T_{\rm ss}) = \langle dE/dt \rangle_{\rm abs} \quad . \tag{54}$$

Once we solve for $T_{\rm ss}$, we calculate the thermal energy content of the grain at this temperature, $E(T_{\rm ss})$. There are two regimes:

- If $E(T_{\rm ss}) \gg \langle h\nu \rangle_{\rm abs}$, then individual photon absorption events do not substantially change the energy content of the grain, and we may assume that the grain temperature $T = T_{\rm ss}$. This is the "steady heating" regime, where we can approximate the discrete heating events as a continuous process.
- If $E(T_{\rm ss}) \ll \langle h\nu \rangle_{\rm abs}$, then individual photon absorption events heat the grain up to peak temperatures $T_{max} \gg T_{\rm ss}$, and the grain will usually cool to a temperature $T_{min} < T_{\rm ss}$ before the next photon absorption event. This is the "stochastic heating" regime, where the discrete nature of the heating has important consequences. As we will see below, stochastic heating is often important.

Figure 17 shows the temperature history of 4 grains of different sizes in the diffuse interstellar medium over a $\sim 10^5\,\mathrm{s}$ interval – about one day. The

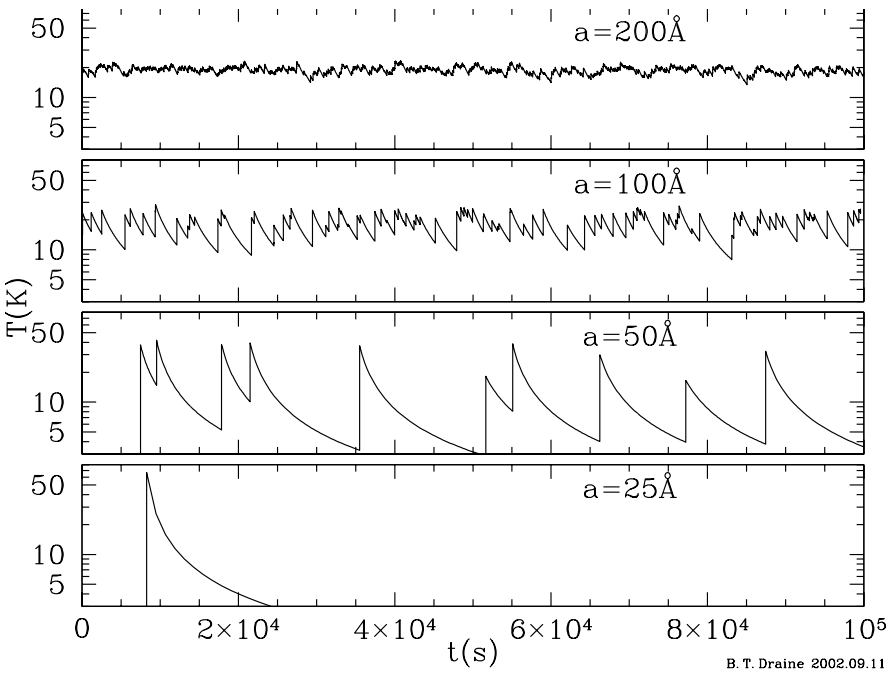

Fig. 17. A day in the life of an interstellar grain: grain temperature vs. time for 4 grain sizes, for grains heated by the average interstellar radiation field. Grains with $a \gtrsim 200$Å have a nearly constant temperature, but $a \lesssim 100$Å grains show conspicuous increases in temperature following each photon absorption, with gradual cooling between photon absorption events.

temperature of the $a = 200$Å grain fluctuates in a small range around $\sim 20\,$K. However, as the grain size is reduced, the fluctuations become increasingly extreme, with the peaks being higher and the low points being lower. The smallest grain shown ($a = 25$Å) absorbs about 1 starlight photon per day; this grain spends most of its time quite cool, but immediately following absorption of a photon the grain temperature reaches $\sim 50\,$K. The grain cools by infrared emission; it is obvious that most of the infrared emission must take place during the brief interval while the grain is "hot". If we wish to calculate the time-averaged emission spectrum, we cannot use the "average" grain temperature – we need to integrate over a distribution of grain temperatures. This phenomenon is even more pronounced for smaller grains. A grain with a radius of 5Å has a volume only 1/125 that of the 25Å shown in Figure 17; the mean time between photon absorptions is of order $\sim 10^7\,$s, but a 10 eV starlight photon can raise the grain temperature to $\sim 10^3\,$K.

Let $P(E)$ be the probability of the grain having vibrational energy $E' \geq E$. In the steady heating regime, we approximate $P(E)$ as a step function, and $|dP/dE|$ as a delta function $\delta(E - E_{\rm ss})$.

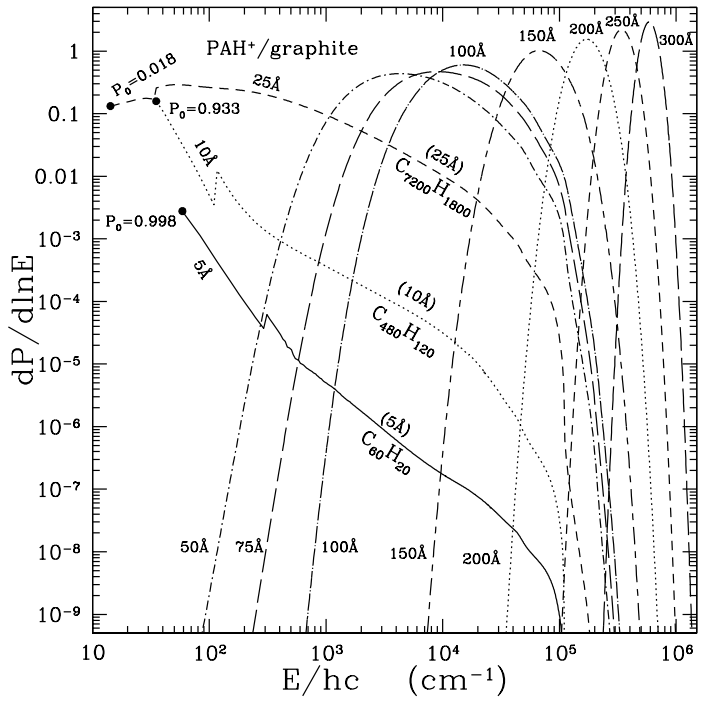

Fig. 18. Energy distribution functions for charged carbonaceous grains with radii $a = 5, 10, 25, 50, 75, 100, 150, 200, 250, 300$Å in the interstellar radiation field. The discontinuity in the 5, 10, and 25Å curves is an artifact due to a change in the method of estimating the cooling when the energy is equal to the 20th vibrational mode. For 5, 10, and 25Å, a dot indicates the first excited state, and the probability P_0 of being in the vibrational ground state is given. Taken from Li & Draine (2001).

In the stochastic heating regime, we must solve for $P(E)$. Draine & Li (2001a) show examples of energy distribution functions. If the energy states are grouped into bins $j = 0, 1, ...$ (where $j = 0$ is the ground state), then we can calculate the state-to-state transition rates T_{ji} for transitions $i \rightarrow j$ due to both photon absorptions and photon emissions. Once $T_{i\rightarrow j}$ is known, we define the diagonal elements $T_{ii} \equiv -\sum_{j\neq i} T_{ji}$. The steady state solution P_j for the probability of being in state j then satisfies the N coupled linear

equations

$$0 = \sum_{j=0}^{M} T_{ij} P_j \quad \text{for } i = 0, ..., M \quad . \tag{55}$$

Using the normalization condition $\sum_{j=0}^{M} P_j = 1$, we obtain a set of M linear equation for the first M elements of P_j:

$$\sum_{j=0}^{M-1} (T_{ij} - T_{iM}) P_j = -T_{iM} \quad \text{for } i = 0, ..., M-1 \quad , \tag{56}$$

which we solve using standard techniques. In practice, we take $M \approx 500$, in which case iterative methods are required to efficiently solve for P_j. Once the P_j are determined for $j = 0, ..., M-1$ we could obtain P_M by subtraction $P_M = 1 - \sum_{j=0}^{M-1}$ but this is inaccurate; it is better to instead use

$$P_M = \frac{-1}{T_{MM}} \sum_{j=0}^{M-1} T_{Mj} P_j \quad . \tag{57}$$

Fig. 18 shows $dP/d\ln E$ for carbonaceous grains heated by the average intestellar radiation field (ISRF) due to starlight in an H I region, as estimated by Mathis, Mezger, & Panagia (1983, hereafter MMP). For $a \lesssim 25$Å grains $dP/d\ln E$ becomes very small for $E/hc > (1/911\text{Å}) = 1.1 \times 10^5\,\text{cm}^{-1}$: this reflects the fact that grains cool essentially completely between photon absorption events, so that the energy content virtually never rises above the maximum energy (13.6 eV) of the illuminating photons. As the grain size increases, the time between photoabsorptions goes down, and the cooling time at fixed energy goes up; when the grain size exceeds ~ 30Å there is a significant probability of a photoabsorption taking place before the energy of the previous photoabsorption has been radiated away. However, stochastic heating effects are noticeable even for grains as large as 300Å – the energy distribution function has narrowed considerably, but is still appreciably broad.

3.2 IR and Far-IR Emission Spectrum

With the energy distribution function calculated as discussed above, we can now calculate the time-averaged emission spectrum for a carbonaceous grain:

$$F_\lambda = 4\pi \int dE \frac{dP}{dE} C_{\rm abs}(\lambda) B_\lambda(T(E)) \quad . \tag{58}$$

In Fig. 19 we show the emission spectrum of PAH^+ molecules of various sizes heated by the ISRF, and in Fig. 20 we compare the emission spectrum calculated sing the energy distribution functions $dP/d\ln E$ with emission spectra calculated for dust with steady temperature $T_{\rm ss}$. We see that stochastic heating is important even for grains as large as ~ 100Å in the ISRF.

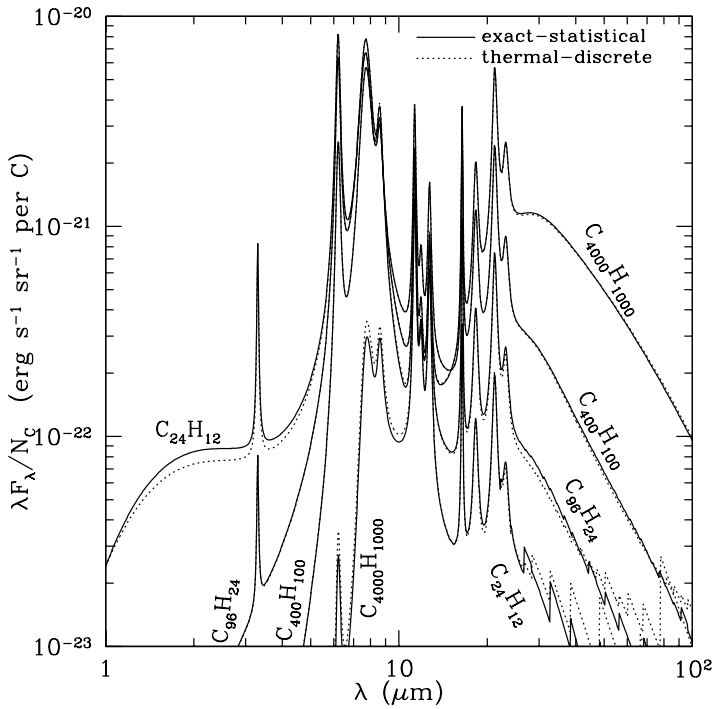

Fig. 19. IR emissivity per C atom for PAH^+ molecules of various sizes illuminated by the average ISRF. Solid line: "exact-statistical" calculation, which uses transition probabilities which do not involve the thermal approximation. Dotted line: "thermal-discrete" calculation where the spontaneous emission rates are calculated using a thermal approximation, as discussed in the text. The two methods are in excellent agreement, indicating that the thermal approximation can be used to calculate the transition rates. Taken from Draine & Li (2001).

In Fig. 21 we show the emission spectrum calculated for a mixture of carbonaceous and silicate grains with size distributions consistent with the average ($R_V = 3.1$) interstellar extinction curve, illuminated by the local ISRF. This should be the emission spectrum of the "cirrus" clouds. Also shown in Fig. 21 are observations of the emissivity per H atom of the dust at high galactic latitudes.

Diamonds show DIRBE photometry; the small triangles show our calculated spectrum convolved with the DIRBE filters, for comparison with the diamonds. The squares show the FIRAS determination of the emissivity per H nucleon. The far-infrared emission is in excellent agreement with the predictions of our dust model. The model is in very good agreement with DIRBE photometry at 3.5 μm and 25 μm; the model appears too low by about a factor 2 at 5 and 12 μm. The observations are difficult; it is hoped that SIRTF

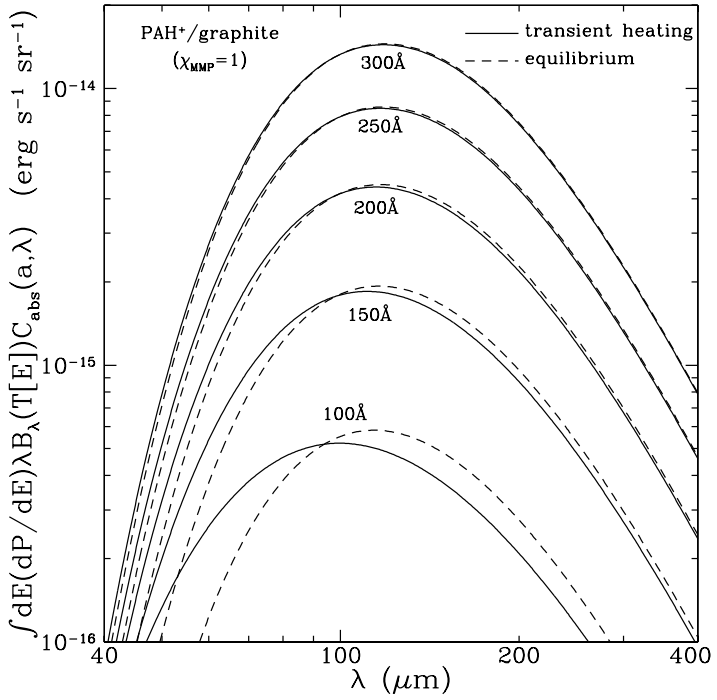

Fig. 20. IR emission per grain for carbonaceous grains of various sizes illuminated by the average ISRF. Solid line: full stochastic heating calculation. Broken line: assuming steady-state temperature $T_{\rm ss}$. For $a \gtrsim 200$Å in the ISRF we see that stochastic heating has little effect on the emission spectrum, but for $a \lesssim 150$Å it significantly modifies the emission spectrum. Taken from Li & Draine (2001).

will be able to measure the spectrum of selected cirrus clouds for comparison with our model.

In Fig. 22 we compare our model with observations taken on the galactic plane, where the FIR surface brightness is much higher. In addition to DIRBE photometry, spectroscopic observations made with the IRTS satellite are available.

These observations are looking in the galactic plane at the "tangent" point of gas in the 6 kpc ring, at a distance of 6 kpc from us. At this distance, the $40'$ DIRBE beam subtends 70 pc, so the observations sum the emission from dust in a region $\sim 70 \times 70$ pc on a side, and many kpc long. We compare the observations to a model which is obviously oversimplified: a uniform slab of dust heated by a uniform radiation field with the spectrum of the local ISRF but whose intensity we scale so that the dust emission best reproduces the observed spectrum: the best fit is obtained with the starlight intensity equal to twice the ISRF. The DIRBE beam obviously includes emission from

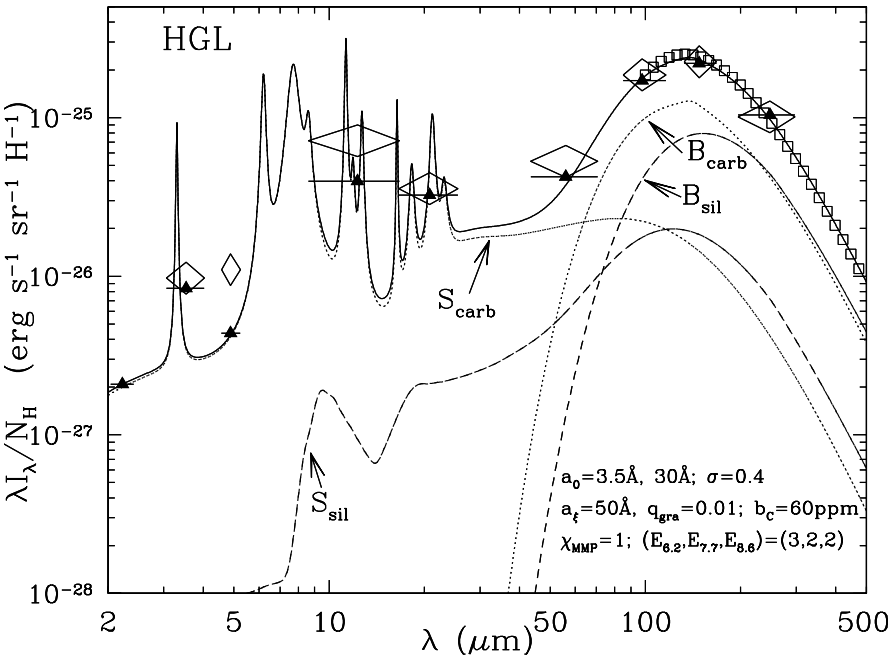

Fig. 21. IR emission per H for dust mixture illuminated by the ISRF. Diamonds: DIRBE (Arendt et al 1998). Squares: FIRAS (Finkbeiner et al. 1999). From Li & Draine (2001).

stars, which we believe dominate at $\lambda < 4\,\mu$m, so our model includes light from stars assumed to be mixed uniformly with the dust. This simple model is in good agreement with the observations. In particular, we successfully reproduce the very strong emission in the 5-12 μm region. The discrepancy at 100 μm is somewhat surprising, but may in part be due to oversimplification of our model, and perhaps in part to uncertainties in the DIRBE absolute calibration.

3.3 The Small Magellanic Cloud (SMC)

How successful is this dust model in reproducing the emission observed from other galaxies? The SMC, with metallicity ∼10% of solar (Dufour 1984), and dust-to-gas ratio ∼10% of the Milky Way (Bouchet et al. 1985) is a good test case. Li & Draine (2002) sum over both quiescent medium and regions of active star formation in the SMC, find that to match the observed spectrum they require a distribution of starlight intensities. Following Dale et al. (2001) they adopt a power-law distribution of starlight intensities.

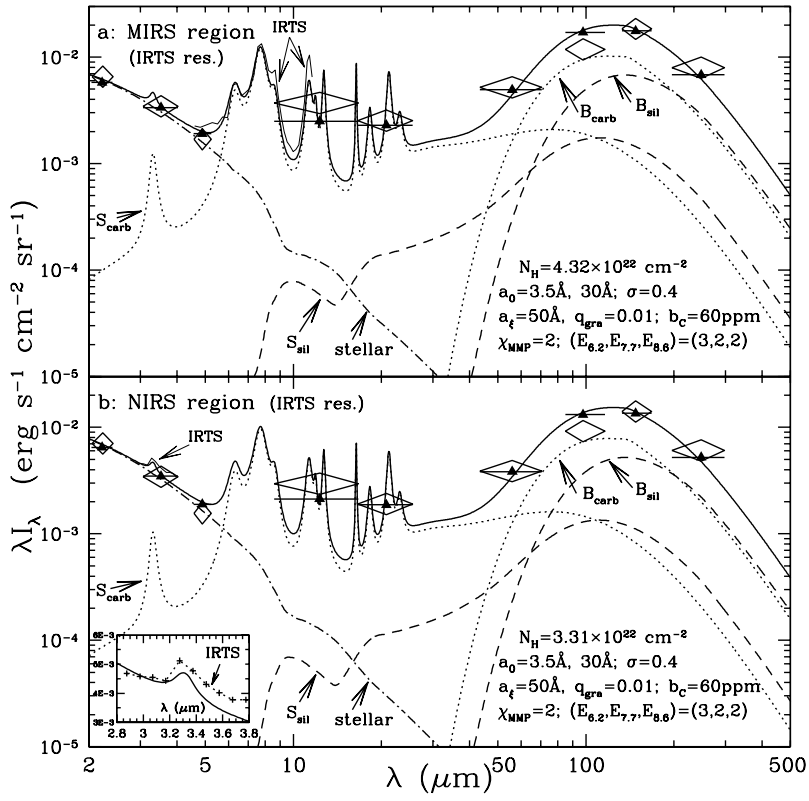

Fig. 22. IR surface brightness toward (a) $l = 44°20'$, $b = -0°20'$; (b) $l = 47°45'$. Diamonds: DIRBE photometry. Thin line, upper panel: 5-12 μm spectrum measured by MIRS on IRTS (Onaka et al. 1996). Thin line, lower panel: 2.8-3.9 μm spectrum measured by NIRS on IRTS (Tanaka et al. 1996). Solid line: carbonaceous-silicate dust model illuminated by 2×ISRF, plus reddened starlight. From Li & Draine (2001).

The dust extinction in the SMC is known to differ from Milky Way dust, primarily in the absence of a 2175Å extinction bump on most (but not all) SMC sightlines (Gordon & Clayton 1998). Since we take the view that the 2175Å feature is due to PAHs, the absence of this feature implies a low PAH abundance. We adopt the dust mixture of Weingartner & Draine (2001a), which reproduces the measured SMC bar extinction curve.

With suitable choice of illuminating radiation field, the dust model is able to reproduce the observed IR emission from the SMC. It appears that the carbonaceous/silicate grain model (Weingartner & Draine 2001a; Li & Draine 2001) can reproduce both the observed interstellar extinction by dust and the observed IR/FIR emission from dust.

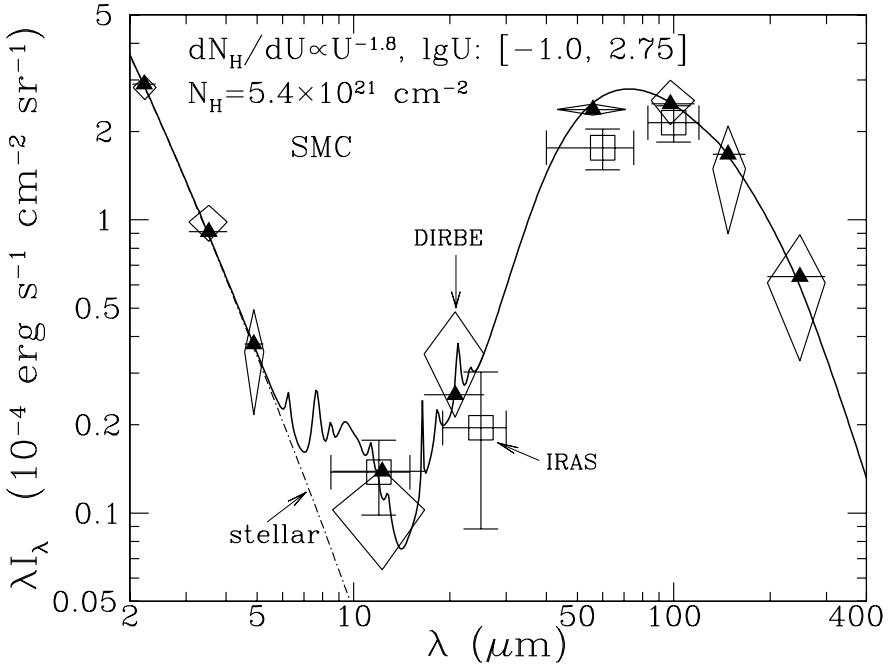

Fig. 23. Comparison between dust model (solid line) and the observed spectrum of the SMC obtained by COBE/DIRBE (diamonds) and IRAS (squares) averaged over a 6.25 deg^2 region including the optical bar and the Eastern Wing (Stanimirovic et al 2000). Model spectrum includes infrared emission from dust heated by a range of starlight intensities. plus starlight, which dominates at $\lambda \lesssim 7\,\mu$m. Triangles show the model spectrum convolved with the DIRBE filters. Taken from Li & Draine (2002).

4 Charging of Interstellar Dust

Why do we care about the charging of dust grains? There are a number of reasons:

- Charged dust grains are coupled to the magnetic field, whereas neutral grains are not. This is important not only for the motions of the dust grains, but also as a mechanism for coupling magnetic fields to neutral gas.
- Charged dust grains undergo stronger gas drag due to Coulomb interaction with ions in the gas.
- The photoelectric charging process injects energetic photoelectrons into the gas, which is a major mechanism for heating interstellar gas.
- Neutral and negatively-charged dust grains can play an important role in neutralization of ions.

- In cold, dense regions, the dust grains may "lock up" a substantial fraction of the electrons.

4.1 Collisions with Electrons and Ions

Consider a spherical grain of radius a and charge $Z_g e$, and a charged particle of charge ze, kinetic energy E, on a trajectory with impact parameter b. If the interaction potential is taken to be a Coulomb potential, then conservation of energy and angular momentum allow one to find the critical impact parameter $b_{\rm crit}$ for the particle to just graze the grain surface. Trajectories with $b < b_{\rm crit}$ will collide with the grain, and trajectories with $b > b_{\rm crit}$ will miss. The collision cross section is simply

$$C = \pi b_{\rm crit}^2 = \pi a^2 \left[1 - \frac{zeU}{E}\right] \quad \text{for } E > zeU \quad , \tag{59}$$

$$= 0 \qquad\qquad\qquad \text{for } E \leq zeU \quad , \tag{60}$$

where $U \equiv Z_g e/a$ is the electrostatic potential at the grain surface. If the velocity distribution is thermal, then the rate at which the charged particles reach the grain surface is just

$$\frac{dN}{dt} = n\pi a^2 \left(\frac{8kT}{\pi m}\right)^{1/2} \times \begin{cases} e^{-zeU/kT} & \text{for } zeU > 0 \\ \left[1 - \frac{zeU}{kT}\right] & \text{for } zeU < 0 \end{cases} \quad . \tag{61}$$

This is a wonderfully simple result. If the sphere is located in a plasma of electrons and ions, and the only charging process is collisional, then the sphere will become negatively charged since the electrons move more rapidly than the ions. The steady-state charge is such that suppression of the electron arrival rate, and enhancement of the ion arrival rate, make them equal:

$$n_e s_e \left(\frac{8kT}{\pi m_e}\right)^{1/2} e^{eU/kT} = n_I s_I \left(\frac{8kT}{\pi m_I}\right)^{1/2} \left[1 - \frac{eU}{kT}\right] \quad , \tag{62}$$

where we have assumed $Z_I = +1$. Taking logarithms of both sides we obtain

$$\frac{eU}{kT} = -\frac{1}{2}\ln\left(\frac{m_I}{m_e}\right) + \ln\left(\frac{s_I}{s_e}\right) + \ln\left(1 - \frac{eU}{kT}\right) \quad , \tag{63}$$

with the solution $eU/kT = -2.51$ for a hydrogen plasma ($m_I/m_e = 1836$) with $s_I = s_e$.

However, the Coulomb potential does not fully describe the interaction between a charged particle and a grain. In the case of a neutral grain, the electric field of the approaching charged particle will polarize the grain, resulting in an attractive potential – the same effect that causes ion-neutral scattering rates to be large, even at low temperatures. [1] Draine & Sutin (1987) have calculated

[1] This is just the familiar "image potential" from electrostatics for a charge near a conductor.

collision rates including the image potential. Image potential effects are important for neutral grains when $e^2/a \gtrsim kT$, or $aT \lesssim 1.67\times10^{-3}\,\mathrm{cm\,K}$. Thus it is an important correction for small grains in cold gas (e.g., $a \lesssim 1.67\times10^{-5}\,\mathrm{cm}$ for $T = 100\,\mathrm{K}$).

The "sticking coefficients" for small electrons and ions are not well known. In the case of an ion with an ionization potential larger than the work function for the grain material, it seems likely that the ion, upon arrival at the grain surface, will either remain stuck to the grain or will strip an electron from the grain and depart; in either case the ion "sticking coefficient" $s_I = 1$. The case of impinging electrons is less clear. The electron might be elastically reflected from the grain surface, or the electron might pass through a small grain and out the other side without energy loss, in which case the electron would have enough energy to return to infinity.

Experimental sticking coefficients for small neutral molecules or molecular ions can be estimated by dividing the measured electron capture rate coefficient by the estimated rate at which the electrons would reach the surface of the ion. Figs. 24 and 25 show the electron sticking coefficients for small neutral and charged carbonaceous clusters containing $10 < N_\mathrm{C} < 100$ carbon atoms.

In hot gas, it is possible for impinging electrons to eject an electron from the grain. For molecules, this is called "ionization"; for larger objects, it is called "secondary electron emission". It is therefore possible for grains to become positively charged by collisions in a hot ($T \gtrsim 10^6\,\mathrm{K}$) plasma (Draine & Salpeter 1979a).

4.2 Photoelectric Emission

The electrons in a neutral grain can be thought of a being confined within a potential well, as shown in Fig. 26. The potential well is produced by a "double layer" of charge at the boundary of the grain (the electron charge density extends beyond the ion charge density, resulting in a region near the surface with a radial electric field – see standard texts on solid state physics, e.g., Ashcroft & Mermin 1976).

Three cases are shown:

- For a grain with $Z \geq 0$, the excited electron will be subject to a long-range Coulomb attraction by the rest of the charge. In this case the electron which physically gets outside of the grain must still have additional energy in order to reach ∞.
- For a grain with charge $Z = -1$, the excited electron sees a system with zero net charge, so once the electron is physically outside the double layer, it will continue to infinity.
- For a grain with charge $Z < -1$, an electron which gets outside the double layer will be accelerated away from the grain. An excited electron can in principle penetrate the double layer by tunneling, so that it is not

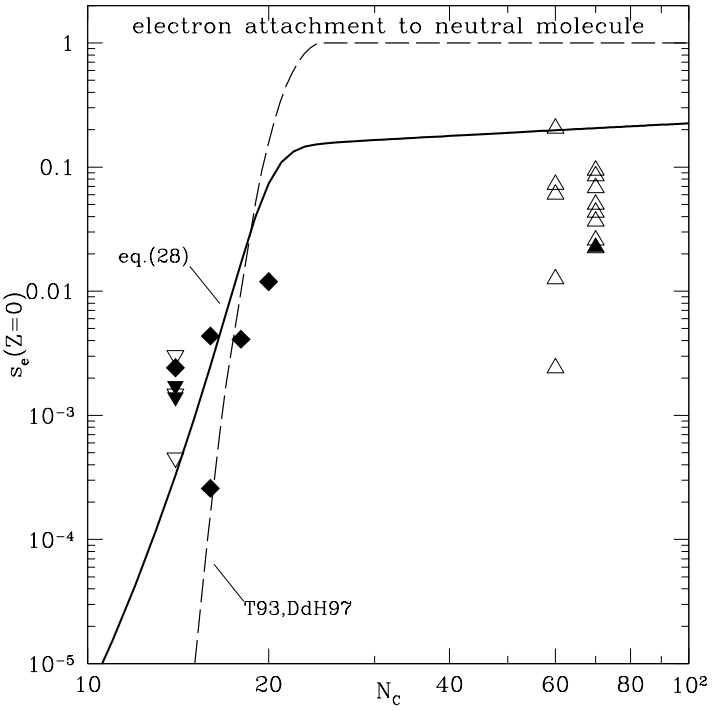

Fig. 24. Electron sticking coefficient for small neutral grains. From Weingartner & Draine (2001c).

actually necessary for the electron to have an energy higher than the top of the double layer.

An insulating grain has all the "valence band" energy levels occupied when it is neutral. The difference in energy between the top of the valence band and the first available vacant energy level (in the "conduction band") is referred to as the "band gap". If an insulating grain is to be negatively charged, the excess electrons must occupy available energy levels in the conduction band. Less energy is required to photoeject one of these "excess" electrons (a process known as "photodetachment") than to eject an electron from the top of the valence band.

When an ultraviolet photon is absorbed in a dust grain, it raises an electron to an excited state. If the electron has an energy high enough to reach infinity, and does not lose this energy to inelastic scattering, it will escape and be counted as a "photoelectron". To calculate the rate of photoelectric charging of a grain, we require the "photoelectric yield" $Y(h\nu, Z, a)$, which is the probability that absorption of a photon $h\nu$ will produce a photoelectron. To calculate the rate of photoelectric heating of the gas, we also need to

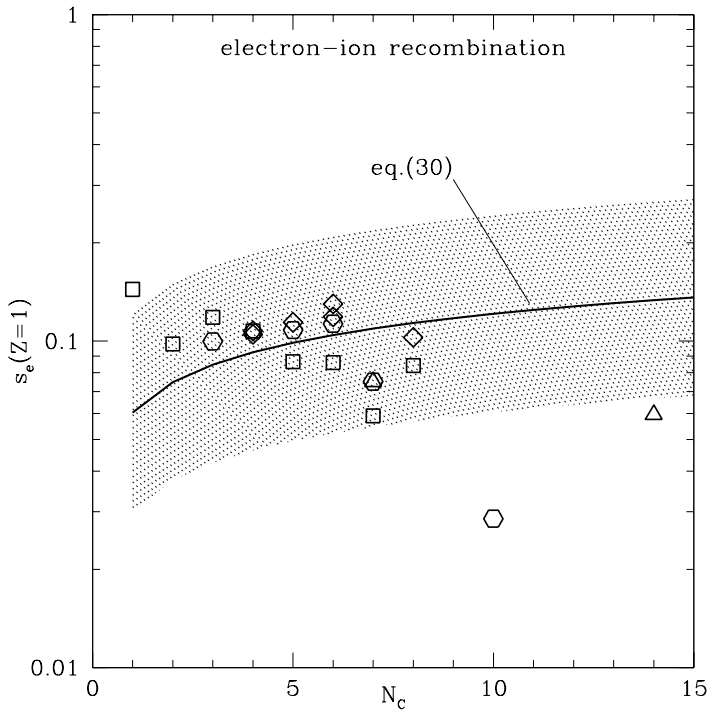

Fig. 25. Electron sticking coefficient for small grains with charge $Z = +1$. From Weingartner & Draine (2001c).

know the energy distribution function $f(E, h\nu, Z, a)$ of the energy E of the photoelectrons leaving the grain.

The photoelectric ejection process consists of four stages:

1. Excitation of an electron of appropriate energy.
2. Motion of the electron from the point of excitation to the grain surface,
3. Penetration of the surface layer and overcoming of the image potential.
4. Once outside the grain surface, the electron must overcome the Coulomb potential (if the grain is now positively charged) to reach infinity.

Weingartner & Draine (2001c) have estimated the photoelectric yield for small grains, both neutral and charged, taking into account the above effects. Allowance is made for dependence of the image potential on the grain radius a, and the possibility of tunneling through the double layer in the case of a negatively charged grain.

Watson (1973) pointed out that very small particles should have enhanced photoelectric yields because of step 2 above: in a small particle, photoexcitations will on average be closer to the grain surface, increasing the probability that the excited electron will reach the grain surface without energy loss.

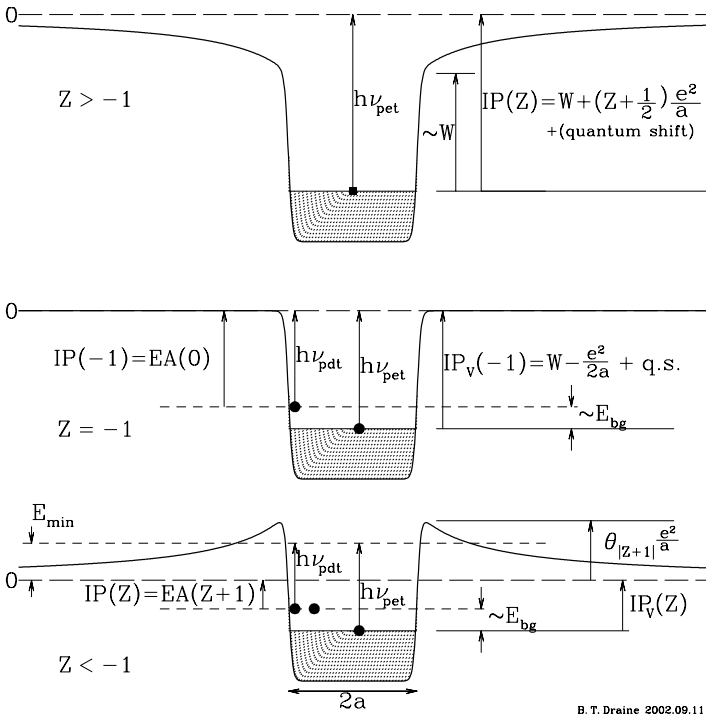

Fig. 26. Model for the potential confining electrons in a grain with charge Ze. Shaded regions show occupied energy levels. W is the work function for bulk material; $IP(Z)$ is the ionization potential; $EA(Z)$ is the electron affinity; $h\nu_{\rm pet}$ is the photoelectric threshold energy; $h\nu_{\rm pdt}$ is the photodetachment threshold energy (the minimum photon energy required to detach an electron from a negatively charged grain); $IP_V(Z)$ is the energy difference between infinity and the top of the valence band; $E_{\rm bg}$ is the bandgap energy for the material ($E_{\rm bg} = 0$ for a metal). Taken from Weingartner & Draine (2001c).

Draine (1978) proposed a simple function to estimate the magnitude of this yield enhancement, which we use:

$$y_1 = \left(\frac{\beta}{\alpha}\right)^2 \frac{\alpha^2 - 2\alpha + 2 - 2\exp(-\alpha)}{\beta^2 - 2\beta + 2 - 2\exp(-\beta)} \quad , \tag{64}$$

$$\beta = \frac{a}{l_a} \qquad \alpha = \frac{a}{l_a} + \frac{a}{l_e} \quad , \tag{65}$$

where $l_a = \lambda/[4\pi{\rm Im}(m)]$ is the photon attenuation length in the material, and l_e, the "electron escape length", is essentially the mean free path against energy loss to inelastic scattering for an excited electron. In the limit $\alpha \ll 1$ we have

$$y_1 \rightarrow \frac{\alpha}{\beta} = \frac{l_a + l_e}{l_e} \quad . \tag{66}$$

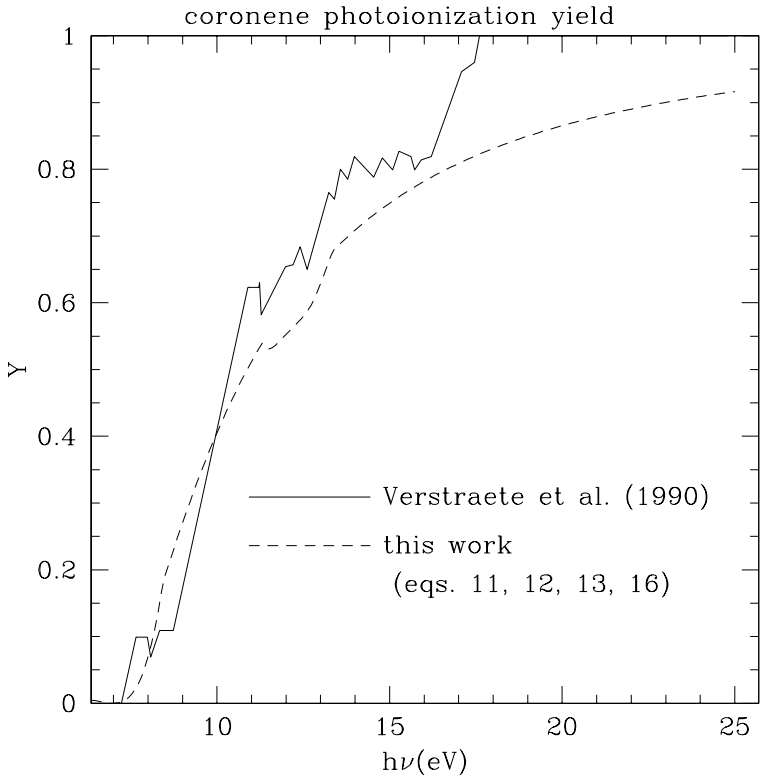

Fig. 27. Photoelectric yield for neutral coronene, as measured by Verstraete et al. (1990) and as estimated in the approach of Weingartner & Draine (2001c). Eq. 11, 12, 13, 16 refer to equations in Weingartner & Draine (2001c), from which this figure is taken.

Photon attenuation lengths $l_a \approx 300$Å are typical in the vacuum ultraviolet. Martin et al. (1987) report $l_e \approx 9$Å for 6 eV electrons in thin carbon films, and McFeely et al. (1990) report $l_e \approx 6$Å for 8 eV electrons in SiO_2. Weingartner & Draine (2001c) adopt $l_e = 10$Å, independent of energy, for both graphite and silicate grains. Since $l_e \ll l_a$, it is clear that very large yield enhancement factors y_1 are possible for very small grains.

Weingartner & Draine write

$$Y(h\nu, Z, a) = \min\left[y_0 \times y_1(h\nu, a)\right] \times y_2(h\nu, Z, a) \tag{67}$$

where y_2 is the fraction of electrons which, having crossed the grain surface, have sufficient energy to overcome the long-range coulomb attraction if $Z \geq 0$ (for $Z < 0$, $y_2 = 1$). For PAHs and larger carbonaceous grains, y_0 is chosen

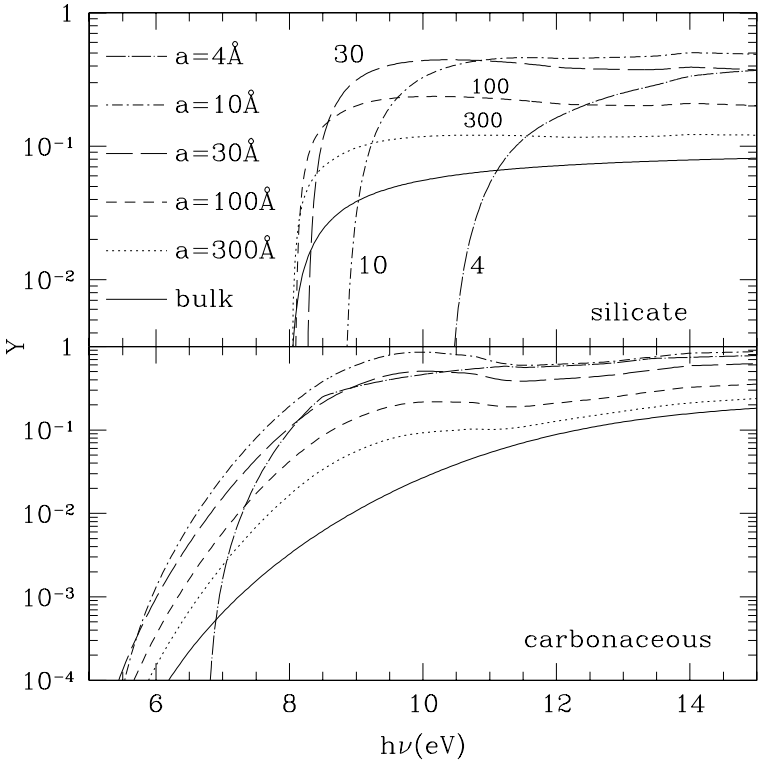

Fig. 28. Photoelectric yields (photoelectrons per absorbed photon) for neutral graphite and silicate grains as a function of incident photon energy $h\nu$, for selected values of the grain radius a. From Weingartner & Draine (2001c).

so that $Y = y_0 y_1 y_2$ approximates the photoionization yield measured for coronene.

Fig. 28 shows the photoelectric yields estimated for neutral carbonaceous and silicate grains of various radii.

4.3 Charge Distribution Functions

Fig. 29 shows grain charge distribution functions calculated for dust in a molecular cloud region. The H nucleon density is taken to be $n_{\rm H} = 300\,{\rm cm}^{-3}$, the gas temperature $T = 25\,{\rm K}$, and the fractional ionization $n_e/n_{\rm H} = 10^{-4}$. The radiation field is assumed to have the spectrum of the MMP ISRF, but with intensity a factor of 10 below the MMP value. Under these conditions small grains ($a \lesssim 200$Å) remain negatively charged. For larger grains, the reduced importance of "image charge" effects (as well as a slight reduction

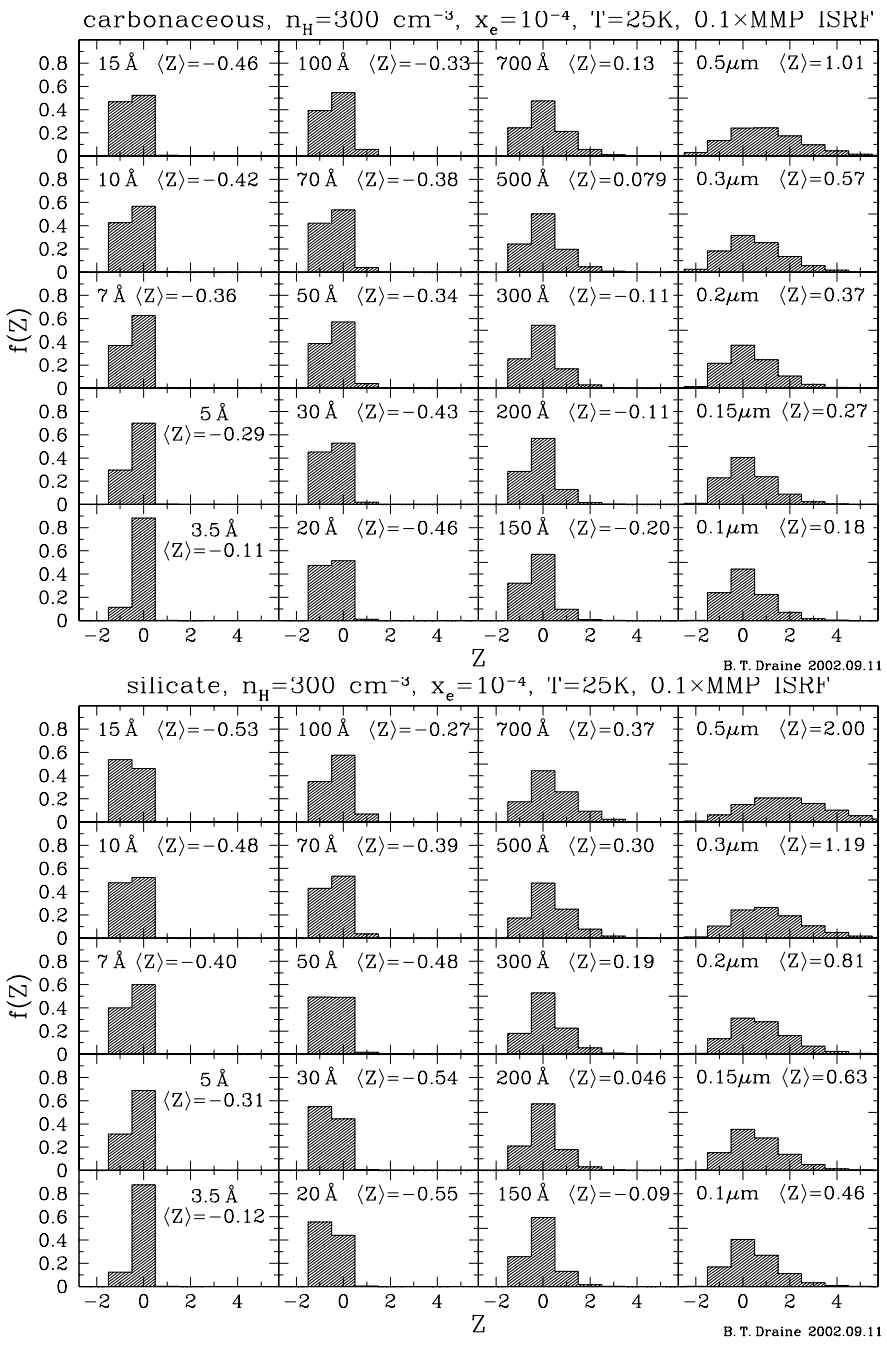

Fig. 29. Charge distribution functions for carbonaceous grains and silicate grains in cold molecular gas.

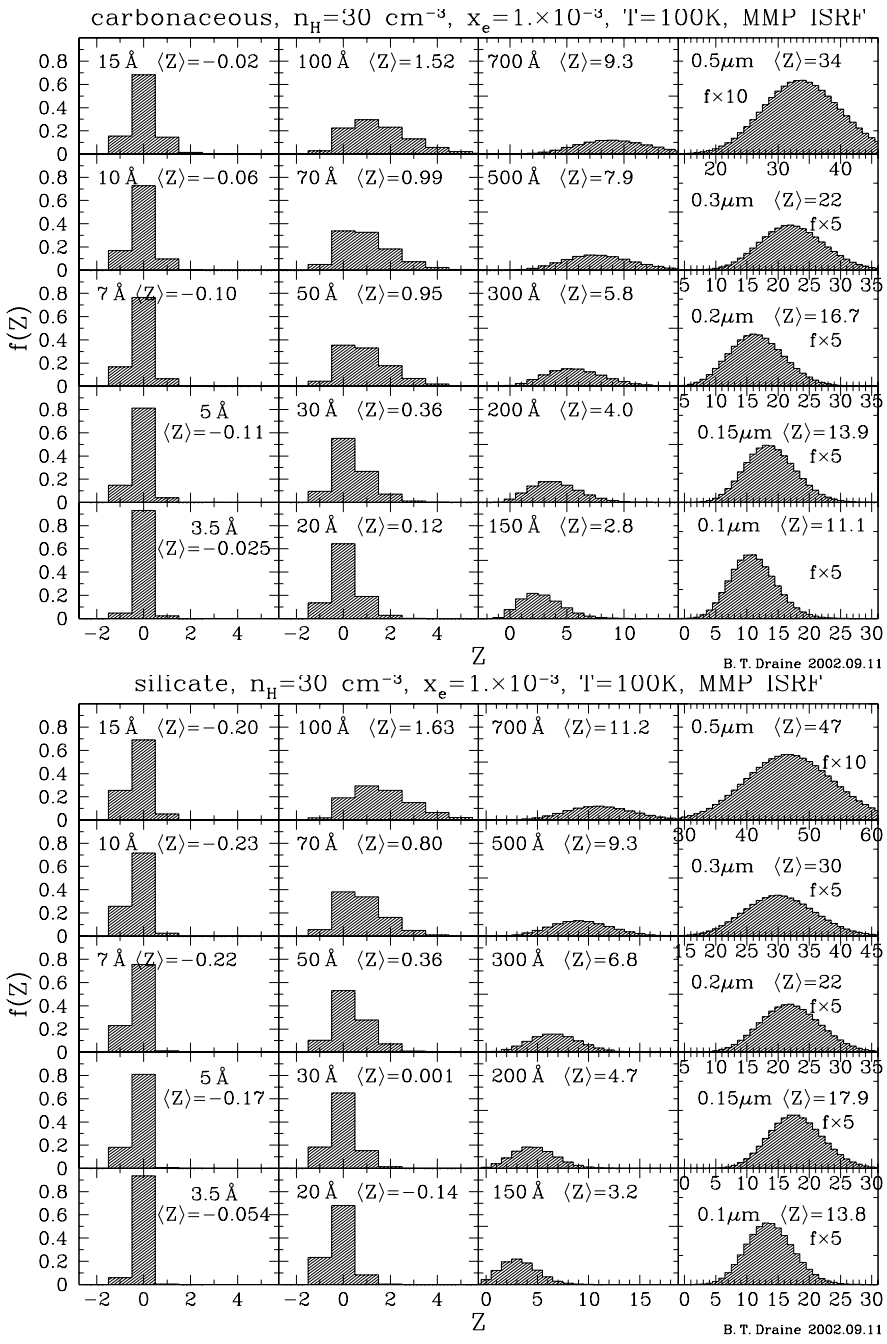

Fig. 30. Charge distribution functions for carbonaceous grains and silicate grains in "cold neutral medium" diffuse HI.

in the work function) tilts the balance in favor of photoelectric charging, but the grain potentials remain very small.

Fig. 30 shows grain charge distribution functions calculated for a diffuse region with starlight equal to the MMP ISRF. The electron density $n_e = 0.03\,\mathrm{cm}^{-3}$ is taken to be the same as for the molecular cloud region of Fig. 29, but the increased starlight intensity allows photoelectric emission to dominate the charging for grains with $a \gtrsim 25$Å. function The "CNM" conditions are appropriate to diffuse HI at 100 K. Despite the presence of ultraviolet radiation producing photoelectric emission, note that an appreciable fraction of the small grains can be neutral or even negatively charged.

We see that the competition between collisional charging and photoelectric charging can go either way, depending on the grain composition, the grain size a, the electron density n_e and temperature T, and the spectrum and intensity of the ultraviolet background due to starlight.

5 Dynamics of Interstellar Dust

What are the velocities of interstellar grains? To answer this question, we must understand the forces acting to accelerate or decelerate the grains.

5.1 Gas Drag

If the grain is moving relative to the gas, it will experience a drag force as momentum is transferred from the grain to the gas. This drag force is approximately $F_{\rm drag} = M_{gr} v_{gr}/\tau_{gr}$ where M_{gr} is the grain mass, v_{gr} is the grain speed relative to the gas, and τ_{gr} is the time for the grain to collide with its own mass in gas particles. For the case of an uncharged spherical grain in neutral gas, the problem can be solved exactly, and approximated to within 1% by

$$F_{\rm drag} = 2\pi a^2 kT \sum_i n_i \frac{8 s_i}{3\sqrt{\pi}} \left[1 + \frac{9\pi}{64} s_i^2\right]^{1/2} \qquad s_i^2 \equiv \frac{m_i v^2}{2kT} \quad , \tag{68}$$

where the sum is over the species (H, H_2, He) in the gas (Draine & Salpeter 1979a). If the grain is charged and ions are present, there is an additional "Coulomb drag" term (Draine & Salpeter 1979a), but this is numerically unimportant in regions of fractional ionization $\lesssim 10^{-2}$. Eq. (68) is obtained for either perfectly inelastic collision (where the gas atom is assumed to "stick") to the grain or perfectly elastic specular reflections. For subsonic motion, the drag time is

$$\tau_{\rm drag} = \frac{M_{gr} v}{F_{\rm drag}} = \frac{\rho a \sqrt{2\pi/kT}}{\sum_i n_i \sqrt{m_i}} \quad . \tag{69}$$

For a cool region where the hydrogen is primarily molecular,

$$\tau_{\rm drag} = 1.2\times10^5\,{\rm yr}\left(\frac{a}{0.1\,\mu{\rm m}}\right)\left(\frac{\rho}{3\,{\rm g\,cm^{-3}}}\right)\left(\frac{300\,{\rm cm^{-3}}}{n_{\rm H}}\right)\left(\frac{25\,{\rm K}}{T}\right)^{1/2} \quad , \tag{70}$$

while in a more diffuse region where the hydrogen is atomic,

$$\tau_{\rm drag} = 4.4\times10^5\,{\rm yr}\left(\frac{a}{0.1\,\mu{\rm m}}\right)\left(\frac{\rho}{3\,{\rm g\,cm^{-3}}}\right)\left(\frac{30\,{\rm cm^{-3}}}{n_{\rm H}}\right)\left(\frac{100\,{\rm K}}{T}\right)^{1/2} \quad . \tag{71}$$

5.2 Lorentz Force

Dust grains are charged, and there are magnetic fields in clouds. The cyclotron period is

$$\frac{2\pi}{\omega_c} = \frac{2\pi M_{gr}c}{|\langle Z\rangle|eB} \tag{72}$$

$$= \frac{5.2\times10^4\,{\rm yr}}{|\langle Z\rangle|}\left(\frac{a}{10^{-5}\,{\rm cm}}\right)^3\left(\frac{\rho}{3\,{\rm g\,cm^{-3}}}\right)\left(\frac{3\mu{\rm G}}{B}\right) \quad , \tag{73}$$

where we take $\langle Z\rangle$ because the grain charge fluctuates on a time short compared to the cyclotron period. Values of $\langle Z\rangle$ are indicated in Figs. 29 and 30. The character of the grain dynamics depends on the ratio of the drag force to the Lorentz force, or

$$\omega_c\tau_{\rm drag} = \frac{3}{4\pi}\frac{|\langle Z\rangle|eB}{a^2c}\frac{\sqrt{2\pi/kT}}{\sum_i n_i\sqrt{m_i}} \tag{74}$$

$$= 53\,|\langle Z\rangle|\left(\frac{B}{3\mu{\rm G}}\right)\left(\frac{10^{-5}\,{\rm cm}}{a}\right)^2\left(\frac{100\,{\rm K}}{T}\right)^{1/2}\left(\frac{30\,{\rm cm^{-3}}}{n_{\rm H}}\right) \quad , \tag{75}$$

where we have assumed the hydrogen to be atomic. For grains in cold clouds, we see that we usually have $\omega_c\tau_{\rm drag}\gg1$: grains are strongly coupled to the magnetic field, except for grain sizes where collisional charging and photoelectric charging happen to just balance so that $|\langle Z\rangle|\lesssim0.02(a/10^{-5}\,{\rm cm})^2$.

5.3 Radiation Pressure

The interstellar radiation field is in general anisotropic. As a result, dust grains are subject to "radiation pressure" forces which can cause drift of the grain relative to the gas. This drift can be important as a means of transporting dust through gas, but also because the drifting grains transfer momentum to the magnetic field (via the Lorentz force) and to the gas (via gas drag).

Consider a unidirectional beam of photons of energy $h\nu$, with energy density $u_\nu d\nu$ in interval $(\nu,\nu+d\nu)$. The photons have momentum $h\nu/c$, and

this momentum can be transferred to the grain by absorption or by scattering. It is easy to see that the rate of momentum transfer is

$$F_{\rm rad} = \int \frac{u_\nu d\nu}{h\nu} c \left[C_{\rm abs} + C_{\rm sca}(1 - \langle \cos\theta \rangle) \right] \frac{h\nu}{c} \tag{76}$$

$$= \pi a^2 \int u_\nu d\nu \; Q_{\rm pr}(\nu) \quad Q_{\rm pr}(\nu) \equiv Q_{\rm abs} + Q_{\rm sca}(1 - \langle \cos\theta \rangle) \quad . \tag{77}$$

where $Q_{\rm abs} \equiv C_{\rm abs}/\pi a^2$, $Q_{\rm sca} \equiv C_{\rm sca}/\pi a^2$, and $\langle \cos\theta \rangle$ is the mean of the cosine of the scattering angle.

We are generally interested in values of $Q_{\rm abs}$ and $Q_{\rm pr}$ averaged over the spectrum of the radiation.

We are often content to approximate the radiation from a star by a blackbody spectrum. In neutral regions of the interstellar medium we are frequently interested in averages over a blackbody spectrum with a cutoff at 13.6 eV, and it is useful to calculate spectrum-averaged values

$$\langle Q \rangle_T \equiv \frac{\int_0^{\nu_{\rm max}} d\nu \; B_\nu(T) Q(\nu)}{\int_0^{\nu_{\rm max}} d\nu \; B_\nu(T)} \quad , \tag{78}$$

where $B_\nu(T)$ is the Planck function (53) and $h\nu_{\rm max} = 13.6\,{\rm eV}$.

We will also be interested in Q values averaged over the interstellar radiation field, for which we use the estimate of Mathis, Mezger, & Panagia (1983).

$$\langle Q \rangle_{\rm ISRF} \equiv \frac{\int_0^{\nu_{\rm max}} d\nu \; u_\nu^{\rm ISRF} Q(\nu)}{\int_0^{\nu_{\rm max}} d\nu \; u_\nu^{\rm ISRF}} \quad . \tag{79}$$

Suppose that at some point in the interstellar medium the starlight has a net energy flux $c\Delta u_{\rm rad}$. By summing over the Skymap Star Catalog (Slater & Hashmall 1992), the Tycho Catalog (ESA 1997), and the all-sky ultraviolet observations of the S2/68 experiment on the TD-1A satellite, Weingartner & Draine (2001b) estimated the anisotropy in the starlight background at V, B, and 4 ultraviolet bands. In Fig. 32 we show the net dipole moment of the radiation field at these 6 wavelengths.

5.4 Recoil from Photoelectric Emission and Photodesorption

Radiation pressure is, of course, just the transfer of photon momentum to the grain. However, radiation can serve to energize other processes which can exert a thrust on the grain: photoelectric emission and photodesorption. To see that these might be important, it is sufficient to compare the momentum of an $h\nu \approx 10\,{\rm eV}$ photon with the momentum of the photoelectron it might produce, if the photoelectron kinetic energy $= f \times h\nu$:

$$\frac{p({\rm electron})}{p({\rm photon})} = \frac{(2m_e f h\nu)^{1/2}}{h\nu/c} = 320 f^{1/2} \left(\frac{10\,{\rm eV}}{h\nu} \right)^{1/2} \quad . \tag{80}$$

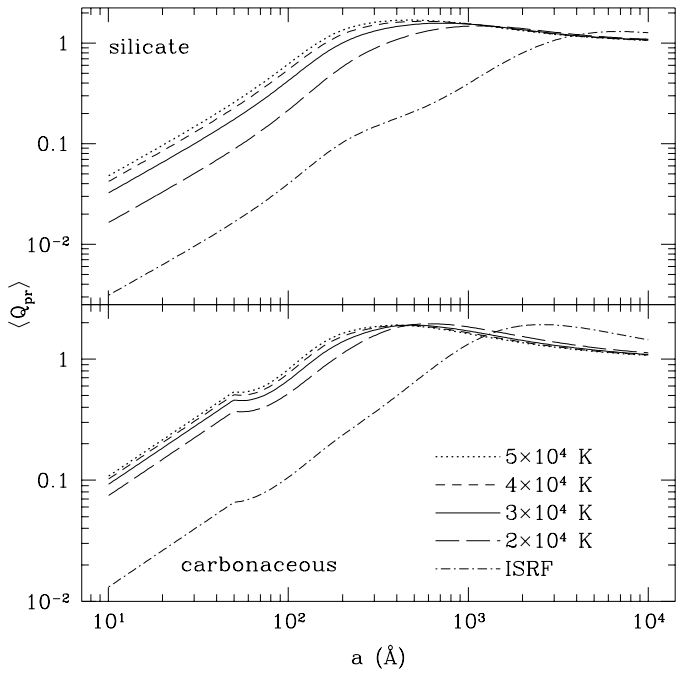

Fig. 31. Radiation pressure efficiency factor $\langle Q_{\rm pr}\rangle$ for neutral carbonaceous and silicate grains, averaged over the interstellar radiation field (ISRF) and blackbody spectra with indicated color tempertures, cut off at 13.6 eV. Taken from Weingartner & Draine (2001b).

Similarly, suppose that a photon caused an H_2 molecule to be desorbed with kinetic energy $f \times h\nu$:

$$\frac{p(H_2)}{p(\text{photon})} = \frac{(4m_{\rm H}fh\nu)^{1/2}}{h\nu/c} = 1.9\times10^4 f^{1/2}\left(\frac{10\,\text{eV}}{h\nu}\right)^{1/2} \quad . \qquad (81)$$

Therefore if an appreciable fraction of absorbed photons produce photoelectrons or photodesorb atoms or molecules, there could be a significant recoil on the grain.

For a spherical grain in an isotropic radiation field, the photoelectrons would be emitted isotropically, with zero net thrust. Suppose, however, that we have a unidirectional radiation field (e.g., light from a single star). In this case we might expect a higher rate of photoelectron emission from the "bright side" than from the "dark side" of the grain. However, very small grains do not have a "dark side" – they are effectively transparent to the incident radiation, so one must try to estimate how this depends on grain size. How can we estimate the bright side/dark side asymmetry? A simple model is to assume

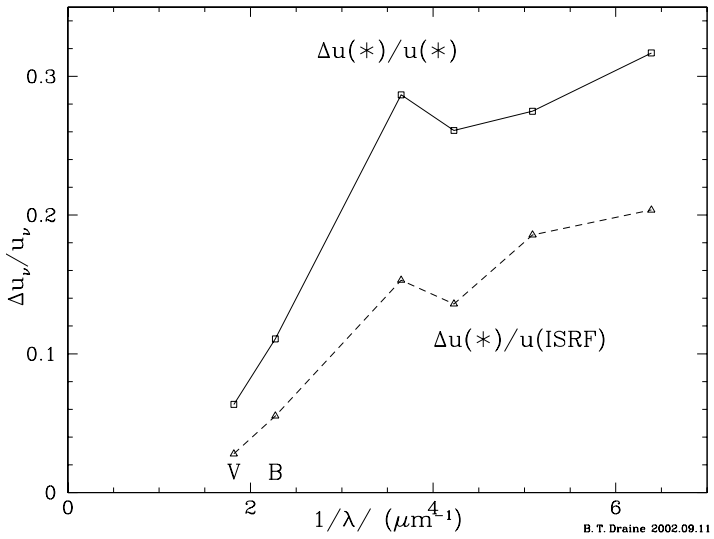

Fig. 32. Dipole fraction for the interstellar radiation field. Upper curve is the ratio of the measured dipole moment to the measured starlight (the measurements are incomplete). Lower curve is the ratio of the measured dipole moment to the total estimated ISRF. The true fraction is probably between these two curves. After Weingartner & Draine (2001b).

that the rate of photoelectric emission from a point on the grain surface is proportional to $|\mathbf{E}|^2$ just inside the surface. Using Mie theory to calculate the electric field intensity $\mathbf{E}$ in a spherical grain, one can then evaluate the relative rates of photoelectric emission over the grain surface. Using this approach, Weingartner & Draine (2001b) have investigated the net thrust due to escaping photoelectrons – equal and opposite to the net momentum which the escaping electrons have when they reach infinity. The photoelectric yield, and the energy of the photoelectrons, is of course affected by the charge on the grain, and therefore depends on the environmental conditions. The analysis is complicated by the fact that if the grain is charged, photoelectrons with nonzero angular momentum will escape to infinity in directions different from the direction they are travelling when they emerge from the grain surface (until it reaches infinity, the electric field of the photoelectron exerts a force on the grain).

Fig. 33 shows the results of Weingartner & Draine (2001b) for the ratio of the photoelectric thrust to the radiation pressure force, as a function of grain size. We see that this is an order-unity correction for grains with $a \approx 100$Å in the CNM.

For photoelectric emission, it is reasonable to assume that the grain is "spherically symmetric" prior to arrival of the photon – there are just as many

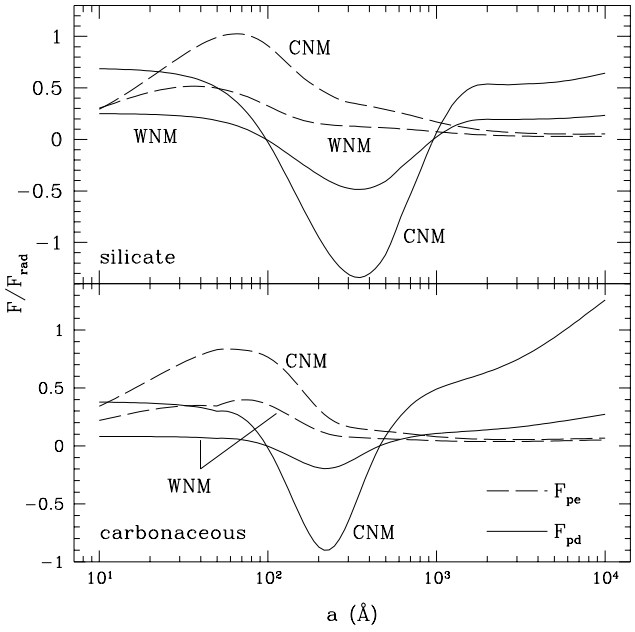

Fig. 33. Photoelectric thrust and photodesorption thrust relative to radiation pressure for carbonaceous and silicate grains as a function of grain radius a. Curve labelled "CNM" is for cold diffuse clouds with $n_e = .03\,\mathrm{cm}^{-3}$, $T = 100\,\mathrm{K}$, and the standard ISRF. Note that the photodesorption force can be negative for grains with radii $100\text{Å} \lesssim a \lesssim 500\text{Å}$. From Weingartner & Draine (2001b).

electrons available for photoejection on the bright side as on the dark side of the grain. For photodesorption, however, this is not a reasonable assumption. As we will see in §6 below, grains are expected to be spinning rapidly, with their principal axis of largest moment of inertia expected to be aligned with the angular momentum. Because of this gyroscopic stabilization, one may expect that if photodesorption is a rapid process, then the "bright" side of the grain will have fewer adsorbed molecules ready to be photodesorbed, an effect which will depend on the orientation of the grain's spin axis with the direction of radiation anisotropy.

If photodesorption is rapid, the thrust will be limited by the need to resupply the grain surface with new molecules to be photodesorbed. The story has a number of additional complications:

- The result will depend on the wavelength-dependence of the photodesorption cross sections for the adsorbed species. This is essentially unknown. Weingartner & Draine simply assume that the photodesorption rate for

a molecule on the grain surface is proportional to $|\mathbf{E}|^2$ just outside the grain surface, integrated from 6-13.6 eV.
- Adsorbed species may diffuse over the grain surface, so that the "bright side" could be replenished from the "dark side".
- If photodesorption is rapid, the surface coverage of adsorbates will depend on the orientation of the grain spin axis relative to the direction of starlight anisotropy.
- The spinning grain can undergo "polar flips" – the "thermal flipping" process described by Lazarian & Draine (1999a).
- If the grain is moving, the grain motion will alter the rates at which molecules are resupplied to the different parts of the grain surface: the "bright side" may suffer a reduction in the rate of arrival of atoms or molecules from the gas.
- H atoms which are not photodesorbed might react on the grain surface to form H_2, and could recoil from the grain with substantial kinetic energy. This process might happen more rapidly on the dark side where the H concentration is higher, thus acting to oppose the thrust due to photodesorption.

With so many uncertainties, it is not possible to reach definite quantitative estimates for the photodesorption force, but Weingartner & Draine (2001b) evaluate one plausible set of assumptions; results are shown in Fig. 33 for grains in the "warm neutral medium" and the "cold neutral medium". It is curious that there is a range of grain sizes (100 - 400Å for carbonaceous grains, 100 - 1000Å for silicate grains) where they find that the photodesorption force is *negative* – this occurs because for this range of sizes, interference effects cause $|\mathbf{E}|^2$ to be larger on what would have been expected to be the dark side of the grain if the grain were opaque and geometric optics were applicable. Note that the larger grains do behave as "expected" for macroscopic targets.

The "bottom line" is that photodesorption can make a significant contribution to the net force on the grain, which (coincidentally) is expected to be comparable in magnitude to the radiation pressure force and the photoelectric thrust, but which can in principle be of the opposite sign, depending on detailed physics of photodesorption which are not known at this time.

5.5 Drift Velocities for Interstellar Grains

For the special case where the radiation anisotropy is parallel to the magnetic field direction, we can obtain the steady-state grain drift velocity by balancing the drag force against the radiation-related forces:

$$F_{\rm drag} = F_{\rm rad} + F_{\rm pe} + F_{\rm pd} \quad , \tag{82}$$

where $F_{\rm pe}$ and $F_{\rm pd}$ are the forces due to photoelectric emission and photodesorption. If we assume subsonic motion, and neglect Coulomb drag, this can

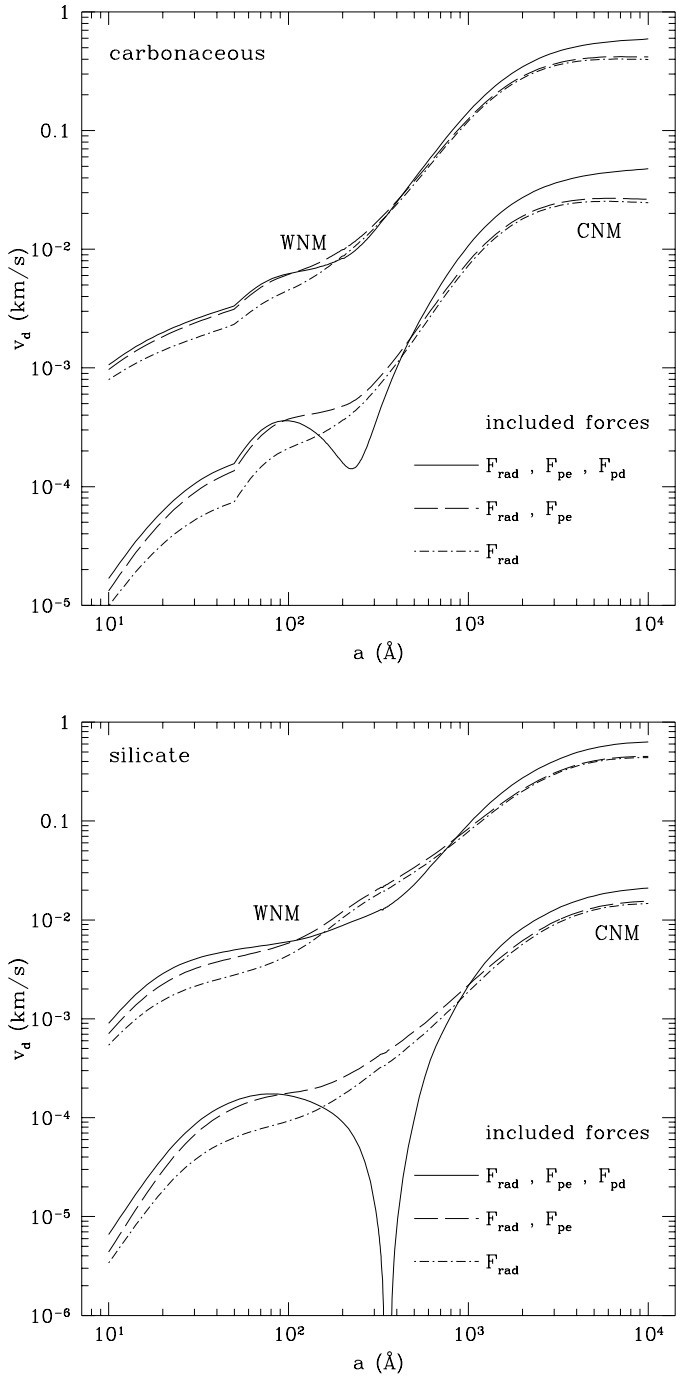

Fig. 34. Drift velocities for carbonaceous and silicate grains, as a function of grain size, in the CNM and WNM, for a radiation anisotropy $\Delta u_{\rm rad}/u_{\rm ISRF} = 0.1$. Taken from Weingartner & Draine (2001b). The minimum in drift velocity for $a \approx 250$Å carbonaceous grains or $a \approx 350$Å silicate grains in the CNM is due to the reversal of the photodesorption force for grains in this size range (see Fig. 33).

be written

$$\frac{v_{\rm drift}}{\sqrt{kT/m_{\rm H}}} = \langle Q_{\rm pr}\rangle \left(\frac{\Delta u_{\rm rad}}{n_{\rm H}kT}\right) \frac{1+F_{\rm pe}/F_{\rm rad}+F_{\rm pd}/F_{\rm rad}}{\sum_i (n_i/n_{\rm H})\sqrt{m_i/m_{\rm H}}} \quad , \tag{83}$$

so we see that the grain will drift with a "Mach number" which is approximately equal to $\langle Q_{\rm pr}\rangle$ times the ratio of the anisotropic radiation pressure to the gas pressure. Since $Q_{\rm pr}$ reaches values of order unity (see Fig. 31), we may expect peak Mach numbers or order 0.2 or so – the ratio of the anisotropic radiation energy density to the gas pressure in the diffuse ISM.

In Figure 34 we show drift speeds calculated by Weingartner & Draine for carbonaceous and silicate grains in the WNM and CNM. The drift speeds are clearly a strong function of grain size, and appear to be negligible for small $a \lesssim 100$Å grains. For larger grains the drift velocities are modest but potentially significant since they could be sustained for long times: in the CNM, a radiation anisotropy of only $\Delta u_{\rm rad}/u_{\rm rad} = 0.1$ would give a $0.3\,\mu$m carbonaceous grain a drift speed of $\sim 0.04{\rm km\,s^{-1}}$, so in 10 Myr it could drift 0.4 pc, and in the WNM the drift speeds are about an order of magnitude larger. This could in principle lead to removal of the large grains from some gas elements and concentration in others.

6 Rotational Dynamics of Interstellar Dust

The rotational dynamics of interstellar grains constitutes a fascinating story, not yet fully told. It is intimately tied to the long-standing problem of interstellar grain alignment, which we will discuss in §7.

6.1 Brownian Rotation?

Early discussions of the rotational dynamics of interstellar grains generally assumed the grains to be rigid spheres, which appeared to capture the essential physics, and discussed the scattering of impinging atoms from the grain surface. As far as grain rotation was concerned, it seemed obvious that the grain would simply undergo a form of Brownian motion, exchanging linear and angular momentum with the gas. Once statistical equilibrium was attained, a rigid grain (with purely elastic scattering of atoms from its surface) would have an expectation value of $kT_{\rm gas}/2$ for the kinetic energy in each of its degrees of freedom: three translational and three rotational. Thus the r.m.s. translational velocity of the grain would be

$$\langle v^2\rangle^{1/2} = \left(\frac{3kT}{M}\right)^{1/2} = \left(\frac{9kT}{4\pi\rho a^3}\right)^{1/2} \tag{84}$$

$$= 1.82\frac{\rm cm}{\rm s}\left(\frac{T}{100\,{\rm K}}\right)^{1/2}\left(\frac{3\,{\rm g\,cm^{-3}}}{\rho}\right)^{1/2}\left(\frac{10^{-5}\,{\rm cm}}{a}\right)^{3/2} \quad , \tag{85}$$

which is negligible under all foreseeable circumstances. The r.m.s. rotation rate

$$\frac{\langle\omega^2\rangle^{1/2}}{2\pi} = \frac{1}{2\pi}\left(\frac{3kT}{2Ma^2/5}\right)^{1/2} = \frac{1}{2\pi}\left(\frac{45kT}{8\pi\rho a^5}\right)^{1/2} \tag{86}$$

$$= 4.6\times10^4\mathrm{Hz}\left(\frac{T}{100\,\mathrm{K}}\right)^{1/2}\left(\frac{3\,\mathrm{g\,cm^{-3}}}{\rho}\right)^{1/2}\left(\frac{10^{-5}\,\mathrm{cm}}{a}\right)^{5/2} \tag{87}$$

is more impressive, though it simply corresponds to an equatorial velocity equal to the r.m.s. translational velocity (85) times a factor $\sqrt{5/2} = 1.58$.

6.2 Suprathermal Rotation

Following the discovery of grain alignment in 1949, theoretical studies of the rotational dynamics were carried out to try to understand the alignment process, including the seminal paper by Davis & Greenstein (1951). It was recognized that, since interstellar grains were likely to have vibrational temperatures differing from the gas temperature, eq. (87) needed to be modified, and it was understood that for a spherical grain the temperature T appearing in eq. (87) should be some weighted mean of the gas temperature and the grain temperature, since collisions of atoms with the grain surface will not be perfectly elastic.

However, in 1975 – 24 years after Davis & Greenstein's study – Purcell (1975) realized that interstellar grains could act as "pinwheels". After all, a simple pinwheel weighing many grams can readily be put into rotation with a rotational kinetic energy many orders of magnitude greater than kT by the air molecules which excite it. Purcell (1979) showed, in fact, that there were 3 distinct physical processes acting on interstellar grains which could each, acting alone, cause a grain to rotate with a rotational energy $(1/2)I\omega^2 \gg kT$:

1. The effective "accomodation coefficient" will probably vary over the grain surface, due to chemical inhomogeneities and/or geometrical irregularities. Such variations in accomodation coefficient on a nonspherical grain will lead to a systematic torque (i.e., one which whose time-average is not expected to be zero) if the gas temperature and grain temperature differ.
2. Photoelectrons ejected from the grain may, on average, carry away angular momentum, resulting in a systematic torque.
3. H_2 formation on the grain surface, with the nascent H_2 molecules ejected with a significant kinetic energy, is expected to result in a large systematic torque, particularly if the H_2 formation occurs at a relatively small number of "active sites" on the grain surface.

Purcell showed that of the three processes, the H_2 formation process was likely to be the most important in regions where the H is atomic.

6.2.1 Suprathermal Rotation Driven by H_2 Formation

It is instructive to examine the argument for suprathermal rotation driven by H_2 formation at active sites on the grain surface.

To simplify the argument, let us consider a region where only atomic H is present (no He), and consider a cube of sides $2b \times 2b \times 2b$, with volume $8b^3$, surface area $24b^2$, and effective radius $a_{\rm eff} = (6/\pi)^{1/3}b = 1.24b$.

Choose a site at random on the grain surface, and assume that H_2 molecules are formed at that site at a rate $\dot{N}_1$. For simplicity, suppose that the newly-formed H_2 molecules leave normal to the surface with kinetic energy E_{H_2}. The expectation value for the square of the moment arm is then just $(2/3)b^2$, and the expectation value for the mean square torque exerted by this site is

$$\Gamma_1^2 = \dot{N}_1^2[m_{H_2}v_{H_2}]^2 \times \frac{2}{3}b^2 \tag{88}$$

$$= \frac{8}{3}\dot{N}_1^2 m_H E_{H_2} b^2 \quad . \tag{89}$$

Now suppose that there are a total of N_{site} such sites on the grain surface, and suppose that a fraction γ of the H atoms which impinge on the surface are converted to H_2 (so there are $\gamma/2$ H_2 formation events per arriving H atom). In a thermal gas, the rate per area at which atoms collide with a convex surface is just $n(kT/2\pi m)^{1/2}$, so

$$\dot{N}_1 = \frac{\gamma}{2N_{site}} n({\rm H}) \left(\frac{kT}{2\pi m_H}\right)^{1/2} 24b^2 \quad . \tag{90}$$

Since the sites are assumed to be randomly located, the torques add like a random walk, so that the expectation value for the square of the total torque is just

$$\langle \Gamma_{ex}^2 \rangle = N_{site}\Gamma_1^2 \tag{91}$$

$$= \frac{192}{\pi}\frac{1}{N_{site}}\gamma^2 n({\rm H})^2 E_{H_2} kT\ b^6 \quad . \tag{92}$$

The rotating grain will experience gas drag. For slow rotation rates ω, it is not difficult to show that the drag torque is

$$\Gamma_{drag} = -\frac{80}{3} n({\rm H}) \left(\frac{m_H kT}{2\pi}\right)^{1/2} b^4 \omega \quad . \tag{93}$$

To find $\langle \omega^2 \rangle$, we now set $\langle \Gamma_{ex}^2 \rangle = \langle \Gamma_{drag}^2 \rangle$ to obtain

$$\langle \omega^2 \rangle = \frac{27}{50}\frac{\gamma^2}{N_{site}}\frac{E_{H_2}}{m_H}\frac{1}{b^2} \quad , \tag{94}$$

or a rotational kinetic energy, relative to the thermal value,

$$\frac{I\langle \omega^2 \rangle}{3kT} = \frac{3}{25}\frac{M}{m_H}\frac{\gamma^2}{N_{site}}\frac{E_{H_2}}{kT} \tag{95}$$

$$= 2.0\times10^{11}\frac{\gamma^2}{N_{site}}\left(\frac{b}{10^{-5}\,\mathrm{cm}}\right)^3\left(\frac{\rho}{3\,\mathrm{g\,cm^{-3}}}\right)\left(\frac{E_{\mathrm{H_2}}}{\mathrm{eV}}\right)\left(\frac{100\,\mathrm{K}}{T}\right)\ . \quad (96)$$

where $M = 8b^3\rho$ is the grain mass. Now this is no small number! The number of active sites is uncertain. If we suppose that there is a surface area s^2 per active site, then $N_{site} = 24b^2/s^2$, and

$$\frac{I\langle\omega^2\rangle}{3kT} = 8.4\times10^5\gamma^2\left(\frac{s}{10\text{Å}}\right)^2\left(\frac{b}{10^{-5}\,\mathrm{cm}}\right)\left(\frac{\rho}{3\,\mathrm{g\,cm^{-3}}}\right)\left(\frac{E_{\mathrm{H_2}}}{\mathrm{eV}}\right)\left(\frac{100\,\mathrm{K}}{T}\right). \quad (97)$$

The r.m.s. rotation rate is

$$\frac{\langle\omega^2\rangle^{1/2}}{2\pi} = 3.6\times10^5\mathrm{Hz}\ \gamma\left(\frac{s}{10\text{Å}}\right)\left(\frac{10^{-5}\,\mathrm{cm}}{b}\right)\left(\frac{E_{\mathrm{H_2}}}{1\,\mathrm{eV}}\right)\quad , \quad (98)$$

so that we might have MHz rotational frequencies for $b < 3\times10^{-6}$ cm! It is apparent that systematic torques can play a major role in grain dynamics.

Each H_2 formation site can be thought of as being like a small rocket thruster attached to the grain surface: the systematic torque due to H_2 formation is fixed in body coordinates, so long as the H_2 formation sites do not change. The kinetics of H_2 formation on grain surfaces is poorly understood at this time, and it is not certain how long-lived the active sites are likely to be.

6.2.2 Radiative Torques Due to Starlight

The three torques identified by Purcell do indeed appear to be individually capable of driving grains to suprathermal rotation. In fact, there appears to be an additional physical process which can compete with the H_2 formation torque for grains larger than $\sim 10^{-5}$ cm: torques exerted on interstellar grains by starlight.

We discussed above the "radiation pressure" force which anisotropic starlight could exert on a grain. It turns out that starlight can also exert a torque on grains, and these torques can be dynamically important!

How can we address this problem? Analytic progress is difficult, because the only cases for which we have analytic solutions are cases where radiative torques vanish: (1) grains of complex shape but small compared to the wavelength; (2) spheres; (3) spheroids. In the first case the torques vanish because only the dipole response of the grain is important, and the dipole radiation does not carry angular angular momentum. In the case of spheres and spheroids, there is no torque because of the symmetry of the target.

In order to obtain a nonzero torque we must have an asymmetric target. Draine & Weingartner (1996) discussed use of the discrete dipole approximation to calculate radiative torques. The DDSCAT code (Draine & Flatau 2000) now provides the capability to compute torques. For an asymmetric target illuminated by a beam of unpolarized radiation, the direction and magnitude of the torque depends on the orientation of the target relative to

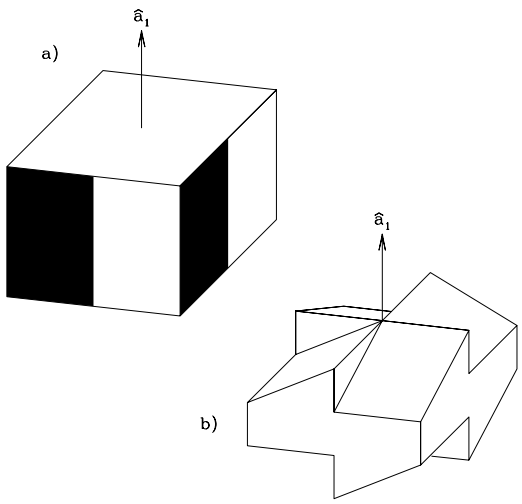

Fig. 35. Macroscopic examples of targets which would be subject to radiative torques. From Draine & Weingartner (1996).

the beam. It is useful to define a "torque efficiency vector" $\mathbf{Q_\Gamma}$ defined so that the torque on the grain is given by

$$\mathbf{\Gamma}_{rad} = \pi a_{\rm eff}^2 u_{rad} \frac{\lambda}{2\pi} \mathbf{Q_\Gamma} \quad , \tag{99}$$

where the effective radius $a_{\rm eff}$ is the radius of an equal volume sphere. We will generally want to average $\mathbf{Q_\Gamma}$ over some spectrum; Draine & Weingartner (1996) calculate

$$\langle \mathbf{Q_\Gamma} \rangle \equiv \frac{\int \mathbf{Q_\Gamma} \lambda u_\lambda d\lambda}{\int \lambda u_\lambda d\lambda} \quad , \tag{100}$$

$$\bar{\lambda} \equiv \frac{\int \lambda u_\lambda d\lambda}{\int u_\lambda d\lambda} \quad , \tag{101}$$

for u_λ taken to be the MMP ISRF (for which $\bar{\lambda} = 1.202\,\mu$m). With these definitions, the torque

$$\mathbf{\Gamma}_{rad} = \pi a_{\rm eff}^2 u_{rad} \frac{\bar{\lambda}}{2\pi} \langle \mathbf{Q_\Gamma} \rangle \quad . \tag{102}$$

We recall from classical mechanics that an arbitrary object has three principal axes, $\hat{\mathbf{a}}_1$, $\hat{\mathbf{a}}_2$, $\hat{\mathbf{a}}_3$, and the moment of inertia tensor is diagonal in a coordinate system aligned with these three axes. Let the eigenvalues of the moment of inertia tensor be $I_1 \geq I_2 \geq I_3$.

For purposes of discussion, let us assume that $I_1 > I_2 = I_3$. If the grain has angular momentum $\mathbf{J}$, then the rotational kinetic energy is

$$E_{rot} = \frac{(J\cos\beta)^2}{2I_1} + \frac{(J\sin\beta)^2}{2I_2} \tag{103}$$

$$= \frac{J^2}{2I_1} + J^2\frac{(I_1-I_2)}{I_1I_2}\sin^2\beta \quad , \tag{104}$$

with the rotational kinetic energy minized for $\beta = 0$. As we will see below, when J is large we expect the grain to remain close to this minimum energy state, with $\sin^2\beta \ll 1$.

The grain spins rapidly, so we are concerned with the torque after averaging over rotations of the grain around the axis $\hat{\mathbf{a}}_1$. This rotation-averaged torque therefore depends only on a single angle – the angle Θ between $\hat{\mathbf{a}}_1$ and the direction of the incident radiation.

We will see below that we expect a spinning dust grain to precess around the direction of the local magnetic field $\mathbf{B}$, so what we really need is the torque averaged over grain rotations *and* over precession of the axis $\hat{\mathbf{a}}_1$ around the magnetic field direction. For a given grain and spectrum of radiation, this will now depend on two angles: the angle ψ between $\mathbf{B}$ and the direction of the radiation, and the angle ξ between $\hat{\mathbf{a}}_1$ and $\mathbf{B}$.

For purposes of spinup (or spindown), we are interested in the projection of the torque efficiency vector along the spin axis, i.e., the axis of largest moment of inertia: $\mathbf{Q}_{\mathbf{\Gamma}}(\hat{\mathbf{\Theta}})\cdot\hat{\mathbf{a}}_1$. Draine & Weingartner (1996, 1997) define $H(\xi,\phi) = \langle \mathbf{Q}_{\mathbf{\Gamma}}\cdot\hat{\mathbf{a}}_{\mathbf{1}}\rangle$ averaged over rotation around $\hat{\mathbf{a}}_1$ and precession of $\hat{\mathbf{a}}_1$ around $\mathbf{B}$. They calculate $H(\xi,\phi)$ for three grain shapes with effective radii $a_{\rm eff} = 0.2\,\mu$m. The numerical values of H of course depend on ξ and ϕ, but a typical value of $|H|$ would be $|H| \approx 0.005$ (see Fig. 5 of Draine & Weingartner 1997), so that the spinup torque would be

$$\langle \mathbf{\Gamma}_{rad}\cdot\hat{\mathbf{a}}_1\rangle = H\bar{\lambda}\Delta u_{rad}\pi a_{\rm eff}^2 \quad . \tag{105}$$

It is of interest to compare this to the spinup torque due to H_2 formation. We can rewrite eq. (92) replacing b by $(\pi/6)^{1/3}a_{\rm eff}$, and project onto a random direction $\hat{\mathbf{a}}_1$ to obtain

$$\langle(\mathbf{\Gamma}_{ex}\cdot\hat{\mathbf{a}}_1)^2\rangle^{1/2} = \frac{1}{3}\left(\frac{2}{3\pi}\right)^{1/2}\left(\frac{6}{\pi}\right)^{1/3}\gamma\left(\frac{E_{\rm H_2}}{kT}\right)^{1/2} s\,n({\rm H})kT\,\pi a_{\rm eff}^2 \quad . \tag{106}$$

Thus the ratio of the radiative spinup torque (105) to the r.m.s. value of the H_2 formation torque is

$$\frac{\langle \mathbf{\Gamma}_{rad}\cdot\hat{\mathbf{a}}_1\rangle}{\langle(\mathbf{\Gamma}_{ex}\cdot\hat{\mathbf{a}}_1)^2\rangle^{1/2}} = \frac{H\bar{\lambda}}{0.191\gamma(E_{\rm H_2}/kT)^{1/2}s}\,\frac{\Delta u_{rad}}{n({\rm H})kT} \tag{107}$$

$$= \frac{2.92}{\gamma}\left(\frac{H}{0.005}\right)\left(\frac{T}{100\,{\rm K}}\right)^{1/2}\left(\frac{\rm eV}{E_{\rm H_2}}\right)^{1/2}\left(\frac{10\text{Å}}{s}\right)\frac{\Delta u_{rad}}{n({\rm H})kT} \quad . \tag{108}$$

Adopting the 10% anisotropy estimated by Weingartner & Draine (2001b), we have $\Delta u_{rad} \approx 8.64 \times 10^{-14}\,\mathrm{erg\,cm^{-3}}$. With $n(\mathrm{H}) = 30\,\mathrm{cm^{-3}}$, and $T = 100\,\mathrm{K}$, we have $\Delta u_{rad}/n(\mathrm{H})kT = 0.21$. Therefore with an H_2 formation efficiency $\gamma < 0.5$ the radiative torque would exceed the H_2 formation torque if the other parameters have nominal values (in particular, $s = 10$Å). Many of the numbers are uncertain; the important point is that for $a_{\rm eff} = 0.2\,\mu$m grains the radiative torque has a magnitude which is comparable to our estimate for the H_2 formation torque.

7 Alignment of Interstellar Dust

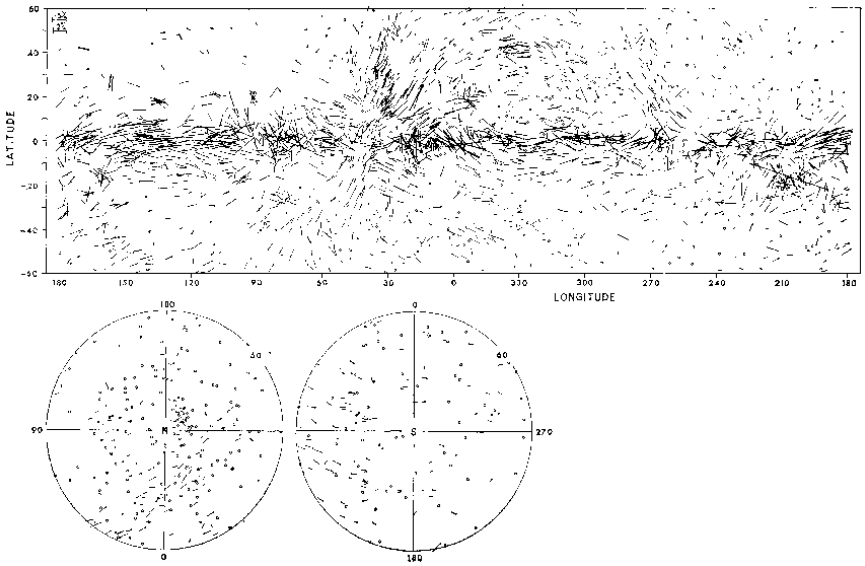

Fig. 36. Linear polarization of light from 1800 stars. From Mathewson & Ford 1970.

Polarization of starlight was discovered in 1949. It was immediately deduced that the only plausible mechanism was "linear dichroism" of the interstellar medium due to aligned dust grains, but understanding the mechanism responsible for this alignment has frustrated astrophysicists for half a century. In fact, the story of the efforts of astrophysicists to understand grain alignment is humbling. It is not just because it has taken us so long to solve the problem – the humbling lesson is that several very important and relatively simple physical effects were overlooked for decades. It was not that these physical effects were difficult to understand, or that they involved physics

which has only recently been understood. On the contrary – the physics involved would have been familiar to well-trained physicist in 1950. It was simply that important processes were overlooked:

- The Rowland effect: a charged, spinning dust grain will develop a magnetic moment due to its circulating charge (Martin 1971).
- The Barnett effect: a spinning dust grain with unpaired electron spins will spontaneously magnetize (Dolginov & Mytrophanov 1976).
- Suprathermal rotation due to dust-gas temperature differences (Purcell 1975, 1979).
- Suprathermal rotation due to photoelectric emission (Purcell 1975, 1979).
- Suprathermal rotation due to H_2 formation (Purcell 1975, 1979).
- Viscoelastic dissipation of rotational kinetic energy due to time-varying stresses in a grain which is not rotating around a principal axis (Purcell 1979)
- "Barnett dissipation" of rotational kinetic energy due to the electron spin system (Purcell 1979).
- Dissipation of rotational kinetic energy due to the nuclear spin system (Purcell 1979).
- Suprathermal rotation due to starlight torques (Draine & Weingartner 1996).
- Fluctuation phenomena associated with Barnett dissipation (Lazarian & Roberge 1997; Lazarian & Draine 1999a) and coupling to the nuclear spins (Lazarian & Draine 1999b)

Have we thought of all the important processes? Or are there other important phenomena to which our eyes are still closed?

7.1 The Motion of Spinning Grains

As seen above, dust grains spin very rapidly. Consider for the moment one spinning grain. If the angular momentum $\mathbf{J}$ does not happen to be along one of the grain's principal axes, then the grain's angular velocity ω will not be parallel to $\mathbf{J}$, and will nutate around $\mathbf{J}$, with a nutation rate that will be smaller than (but comparable to) the rotation rate.

Now imagine observing a single grain as it spins at kHz rotation frequencies. Because the rotation and nutation are both rapid, we will quickly obtain a rotation-nutation average of the grain orientation. During this observation, the angular momentum $\mathbf{J}$ is conserved, and defines a preferred direction. Now consider light propagating in some particular direction. Because of the rotation-nutation averaging, the grain will tend to polarize the light with electric vector either exactly perpendicular to $\mathbf{J}$, or exactly parallel to $\mathbf{J}$, depending on whether the grain on average has its "long" axis perpendicular to $\mathbf{J}$, or parallel to $\mathbf{J}$.

This is for one grain. If a population of grains shows a tendency to polarize light, then the individual grain angular momenta cannot be randomly-oriented – there must be a tendency for the angular momenta **J** to be aligned with some preferred direction in space.

The problem of grain alignment is to account for the alignment of grain angular momenta **J**.

Many alignment mechanisms have been proposed over the years. Some directly involve the galactic magnetic field (Davis & Greenstein 1951). Other proposed mechanisms rely on so-called "mechanical alignment" due to gas (Gold 1952) or cosmic rays (Salpeter & Wickramasinghe 1969) streaming relative to the grains. Harwit (1970) suggested that grain angular momenta might be aligned as a result of the angular momentum absorbed from starlight photons, if the starlight is anisotropic. It was only in 1971 that Martin (1971) pointed out that even in the case of nonmagnetic alignment processes, the observed alignment would be either exactly parallel or exactly perpendicular to the magnetic field, simply as a result of the magnetic moment on a spinning grain.

7.2 Grain Magnetic Moments and Precession Around B

Grain in diffuse regions tend to be electrically charged (see Fig. 30). If charged, a spinning dust grain will develop a magnetic moment due to the "Rowland effect": the rotating charge on the grain constitutes a current circulating around a loop, and there will be a resulting magnetic field and magnetic moment interior to the loop. Recall that a current I flowing in a loop with area A generates a magnetic moment $m = IA/c$. The mean of $x^2 + y^2$ over the surface of a sphere is just $(2/3)a^2$, so the magnetic moment due to charge Ze distributed uniformly over the surface of a spinning sphere is

$$\mu = \frac{\omega Ze}{2\pi c}\pi\frac{2a^2}{3} = \frac{\omega Zea^2}{3c} \quad . \tag{109}$$

If ω is at an angle $\theta > 0$ relative to **B**, the spinning sphere will precess with a precession frequency

$$\omega_p = \frac{\mu B\sin\theta}{I\omega\sin\theta} = \frac{5}{8\pi}\frac{ZeB}{\rho a^3 c} \tag{110}$$

$$= 1.01\times10^{-4}\,\mathrm{yr}^{-1}Z\left(\frac{B}{3\mu\mathrm{G}}\right)\left(\frac{3\,\mathrm{g\,cm}^{-3}}{\rho}\right)\left(\frac{10^{-5}\,\mathrm{cm}}{a}\right)^3 \quad . \tag{111}$$

We have seen above (Fig. 30) that in a CNM environment, we might expect an $a = 10^{-5}\,\mathrm{cm}$ grain to have $\langle Z\rangle \approx 10$, for a precession period $\sim 6000\,\mathrm{yr}$. This time is short compared to the other dynamical times: the gas drag time (71), or (as we shall see below) the time for grain alignment to occur.

We can therefore conclude that regardless of what process is responsible for alignment of interstellar grains, each grain will have a time-averaged

angular momentum distribution which must be symmetric around **B**. Therefore the interstellar dust mixture will tend to polarize starlight either exactly parallel to **B** or exactly perpendicular to **B**, for any conceivable alignment mechanism!

7.3 Barnett Effect

Dolginov & Mytrophanov (1976) pointed out that the "Barnett effect" would result in grain magnetic moments much larger than due to the Rowland effect. The Barnett effect can be stated very simply: an uncharged object rotating with angular velocity ω tends to spontaneously magnetize, with a magnetization $M = \chi\omega/\gamma$, where χ is the susceptibility, and γ is the "gyromagnetic ratio" for the material – the ratio of (magnetic moment)/(angular momentum) for the electron orbitals or electron spins responsible for the magnetizability of the material. For electron spins, $\gamma = \mu_B/(\hbar/2) = e/2m_ec$, where $\mu_B \equiv e\hbar/2m_ec$ is the Bohr magneton.

The spontaneous magnetization is equal to that which would be produced in a stationary sample in a (fictitous) applied magnetic field $H_{Be} = \omega/\gamma = 2m_ec\omega/e$ – the so-called "Barnett equivalent field".

At first sight the Barnett effect seems surprising, but it is not difficult to understand. Consider an unmagnetized sample (equal numbers of "spin-up" and "spin-down" electrons), with angular momentum J, spinning at angular velocity ω. At constant total angular momentum, the angular velocity of the sample can be reduced, with consequent reduction of the rotational kinetic energy $I\omega^2/2$, if some of the angular momentum is put into the electron spin system. The electrons have magnetic moments, so with unequal numbers of electrons in the two spin states, the sample is now magnetized. The reduction in rotational kinetic energy is accompanied by heating of the grain, with an increase in entropy. The effect was observed in the laboratory by Barnett (1915).

For normal paramagnetic materials, the magnetic susceptibility is just $\chi = n_s\mu_B^2/kT_g$, where n_s is the number density of unpaired electrons, and T_g is the grain temperature. The magnetic moment due to the Barnett effect is thus

$$\mu = \frac{4\pi a^3}{3}\frac{n_s\mu_B^2}{kT}\frac{2m_ec}{e}\omega \quad . \tag{112}$$

The ratio of the "Barnett effect moment" to the "Rowland effect moment" is

$$\frac{\mu(\text{Barnett})}{\mu(\text{Rowland})} = \frac{2\pi a n_s\hbar^2}{ZkT_gm_e} \tag{113}$$

$$= \frac{2.8\times10^5}{Z}\left(\frac{a}{10^{-5}\,\text{cm}}\right)\left(\frac{20\,\text{K}}{T_g}\right)\left(\frac{n_s}{10^{22}\,\text{cm}^{-3}}\right) \quad . \tag{114}$$

An unpaired electron density $n_s \approx 10^{22}\,\text{cm}^{-3}$ is typical for normal paramagnetic materials, so it is clear that the Barnett effect is very important

for interstellar grains, and will result in precession periods of order days or months rather than the thousands of years for the Rowland effect.

7.4 Alignment by Paramagnetic Dissipation: Davis-Greenstein Mechanism

Davis and Greenstein (1951) described a mechanism which could produce grain alignment. Consider a grain spinning with angular velocity ω in a static magnetic field $\mathbf{B}_0$. Let θ be the angle between $\mathbf{B}_0$ and ω.

The grain material has a magnetic susceptibility χ, and it will try to magnetize in response to an applied magnetic field. In grain body coordinates, the applied field has a static component parallel to the grain rotation axis, with magnitude $B_\parallel = B_0 \cos\theta$, and a component of magnitude $B_\perp = B_0 \sin\theta$ which appears to be rotating, with angular velocity ω relative to the grain. The rotating field $\mathbf{B}_\perp$ is perpendicular to ω.

It seems clear that the grain material will develop a magnetization $\mathbf{M}$ which will have a static component $\mathbf{M}_\parallel = \chi_0 B_\parallel$ parallel to ω, and a component $\mathbf{M}_\perp$ which rotates in body coordinates (but is stationary in inertial coordinates), with magnitude $M_\perp = |\chi(\omega)| B_\perp$, where $\chi(\omega)$ is the (complex) magnetic susceptibility for a magnetic field rotating at frequency ω. In body coordinates, the rotating magnetization $\mathbf{M}_\perp$ will "lag" behind the rotating field $\mathbf{B}_\perp$ – there will be an "in-phase" component $\chi_1(\omega) B_\perp$ and an "out-of-phase" component $\chi_2(\omega) B_\perp$.

The galactic magnetic field $\mathbf{B}_0$ will exert a torque on the grain magnetic moment $V\mathbf{M}$. The torque is obviously $\perp$ to $\mathbf{B}_0$. A bit of calculation shows that the out-of-phase component of the magnetization results in a torque of magnitude $V\chi_2 B_\perp B_0 = V\chi_2 B_0^2 \sin\theta$ which acts to leave the component of the angular momentum $\parallel$ to B_0 unchanged (the torque, after all, must be $\perp \mathbf{B}_0$) but acts to reduce the component $J_\perp = J\sin\theta$ perpendicular to $\mathbf{B}_0$:

$$\frac{d}{dt} J_\perp = -V\chi_2 B_0^2 \sin\theta \quad . \tag{115}$$

At low frequencies the imaginary component of the magnetic susceptibility varies linearly with frequency: $\chi_2 = K\omega$. With $\omega = J/I = J_\parallel / I\cos\theta$, noting that $J_\parallel = const$, we obtain

$$\frac{d}{dt} J_\perp = J_\parallel \frac{d}{dt} \tan\theta = -J_\parallel \frac{VKB_0^2}{I} \tan\theta \quad , \tag{116}$$

with solution

$$\tan\theta = \tan(\theta_0) e^{-t/\tau_{\rm DG}} \quad , \tag{117}$$

$$\tau_{\rm DG} \equiv \frac{I}{VKB_0^2} \quad . \tag{118}$$

The magnetic susceptibilities of paramagnetic materials are quite well understood at the frequencies of interest (see, e.g., Morrish 1965), with

$$K \approx 1.25 \times 10^{-13}\,\mathrm{s}\left(\frac{20\,\mathrm{K}}{T}\right) \quad . \tag{119}$$

With this value, and $I \approx (2/5)\rho V a^2$, the Davis-Greenstein alignment time

$$\tau_{\rm DG} = \frac{2\rho a^2}{5KB_0^2} \tag{120}$$

$$= 1.2 \times 10^6\,\mathrm{yr}\left(\frac{a}{10^{-5}\,\mathrm{cm}}\right)^2\left(\frac{\rho}{3\,\mathrm{g\,cm^{-3}}}\right)\left(\frac{T}{20\,\mathrm{K}}\right)\left(\frac{5\mu\mathrm{G}}{B_0}\right)^2 \quad . \tag{121}$$

Thermally-rotating grains are disaligned by random collisions with gas atoms on a time scale $\tau_{\rm drag}$. The ratio of the alignment time to the disalignment time is

$$\frac{\tau_{\rm DG}}{\tau_{\rm drag}} = 2.8\left(\frac{n_{\rm H}}{30\,\mathrm{cm^{-3}}}\right)\left(\frac{T_g}{20\,\mathrm{K}}\right)\left(\frac{5\mu\mathrm{G}}{B_0}\right)^2\left(\frac{T}{100\,\mathrm{K}}\right)^{1/2}\left(\frac{a}{10^{-5}\,\mathrm{cm}}\right) \quad , \tag{122}$$

where we have assumed the hydrogen to be atomic. Thus we see that even for $a = 10^{-5}$ cm grains and a relatively high value of the magnetic field strength, alignment is slow compared to disalignment, and the ratio is linear in the grain radius a. The Davis-Greenstein alignment mechanism favors alignment of *smaller* grains, but this is a problem, since small grains are observed to NOT be aligned, while large grains are (Kim & Martin 1995). As we will see below, some important physics has been overlooked.

7.5 Effect of Suprathermal Rotation

Consider now a grain rotating suprathermally. The Davis-Greenstein alignment time is independent of the rotation rate, since the torque is proportional to the rate of rotation. On the other hand, the time scale for random collisions to change the direction of the angular momentum is approximately $(J/J_{th})^2\tau_{\rm drag}$, where J_{th} is the angular momentum expected for Brownian rotation. So if the grain rotation is suprathermal, with $J/J_{th} \gg 1$, we can virtually ignore the disaligning effects of random collisions, and Davis-Greenstein paramagnetic dissipation will bring the grain into alignment with $\mathbf{B}_0$ in a few million years. As we have seen in §6.2, suprathermal rotation appears to be expected. Could it for some reason be suppressed in small grains?

7.6 Thermal Flipping vs. Suprathermal Rotation

Why aren't small grains aligned? From eq. (97) it certainly appears that H_2 formation should be able to drive grains as small as 10^{-6} cm into suprathermal rotation, and yet there is strong evidence that grains smaller than 10^{-5} cm are not aligned (Kim & Martin 1995).

Lazarian & Draine (1999a) have proposed an explanation for this – the process of "thermal flipping" may prevent small grains from achieving suprathermal rotation.

The key issue is that the grain does NOT behave like a "rigid body" subject only to external torques – the grain has internal vibrational degrees of freedom. The grain rotational kinetic energy depends on the angle β between principal axis $\hat{\mathbf{a}}_1$ and $\mathbf{J}$ through eq. (104):

$$E_{rot} = \frac{J^2}{2I_1} + J^2\frac{(I_1 - I_2)}{I_1 I_2}\sin^2\beta \quad . \tag{123}$$

In the absence of external torques (and ignoring the small amount of angular momentum in the spin system), J is fixed, but the rotational kinetic energy can change if energy is exchanged with the vibrational degrees of freedom of the grain. Thus we expect the angle β to fluctuate. Suppose, for example, that we start at $\beta = 0$. Thermal fluctuations will cause β to "explore" the region $0 \leq \beta < \pi/2$. If

$$J^2\frac{(I_1 - I_2)}{I_1 I_2} \lesssim kT \quad , \tag{124}$$

then thermal fluctuations could allow β to reach $\pi/2$: the maximum possible rotational kinetic energy. At this point β can go either way, with equal probabilities, so the grain may "flip over" to the state $\pi/2 < \beta \leq \pi$.

Now consider the effects of H_2 formation torques. These torques are *fixed* in body coordinates. If the grain "flips" from $\beta = 0$ to $\beta = \pi$, the torques change sign in inertial coordinates! As a result, if the grain flips frequently, the H_2 torques can be averaged out to zero, and have no significant effect on the grain dynamics, so that the grain rotation remains essentially thermal! Lazarian & Draine (1999a) refer to this as "thermal trapping".

The question now comes down to estimating the rate of flipping, and how the rate depends on grain size. Lazarian & Draine (1999a) discussed the role which the Barnett effect (i.e., the electron spin system) can play in coupling the grain rotation to the vibrational modes, and concluded that flipping would be rapid enough to result in thermal trapping for grain sizes $a \lesssim 0.1\,\mu$m. This seemed to successfully account for the absence of grain alignment for $a \lesssim 0.1\,\mu$m.

However, further analysis of grain dissipational processes showed that the *nuclear* spin system could be important at the lower rotational rates appropriate to larger grains (Lazarian & Draine 1999b). It was found that the coupling of grain rotation to the nuclear spin system would lead to rapid thermal flipping even for grains as large as $\sim 1\,\mu$m!

Thermal flipping therefore now appears able to prevent H_2 formation torques from being able to achieve superthermal rotation even for the $a \approx 0.2\,\mu$m grains which are observed to be aligned! How is grain alignment to be achieved?

7.7 Effect of Radiative Torques

So long as the grain surface is not modified, the H_2 formation torques are fixed in body coordinates, and thermal flipping will cause these torques to average to zero if the grain spends equal amounts of time in the two "flip states" (i.e., $\beta < \pi/2$ and $\beta > \pi/2$). However, the grain is also subject to other systematic torques, the most important of which is the radiative torque due to anisotropic starlight. This torque is *not* fixed in body coordinates, so that even if the grain spends equal amounts of time in the two flip states, there is a secular change in angular momentum due to the radiative torques. Radiative torques are unimportant for small $a \lesssim 0.05\,\mu$m grains, but very important for $a \gtrsim 0.1\,\mu$m grains. It therefore appears that "thermal trapping" will prevent small ($a \lesssim 0.05\,\mu$m) grains from achieving suprathermal rotation, but that larger ($a \gtrsim 0.1\,\mu$m) grains *can* achieve suprathermal rotation, following which they can be gradually aligned by the Davis-Greenstein mechanism.

But life turns out to be more complicated. Draine & Weingartner (1997) found that radiative torques act not only to spin up grains, but also to change their alignment. The characteristic time scale for radiative torques to change the grain alignment turns out to be just the drag time $\tau_{\rm drag}$, which is shorter than the Davis-Greenstein alignment time, so that the radiative torques appear able to dominate over the systematic effects of the Davis-Greenstein alignment torque.

Study of three different grain shapes and different angles between the magnetic field direction and the starlight anisotropy direction showed that under some conditions the starlight torques brought about alignment (the aligned state was an "attractor"), while under other conditions the grain did not settle down in any stationary state. There appeared to be an overall tendency for grain alignment to take place, but the sample of 3 grain shapes was insufficient to reach general conclusions.

Further study of this problem is underway, and it is hoped that in a year or two we will have definite conclusions on the role of radiative torques in the grain alignment problem. But for the moment the situation appears very promising – we seem to finally understand the absence of alignment of small grains, and it appears that the physics we now understand will explain the alignment of the larger ones, with radiative torques due to starlight playing a critical role.

7.8 Alignment and Disalignment in Different Regions

There is evidence that the degree of grain alignment varies from one region to another. Observations of polarization of starlight indicate that the $a \gtrsim 0.1\,\mu$m grains in diffuse clouds are substantially aligned, but JHK observations of quiescent dark clouds (Goodman et al. 1995) indicate that the dust grains in the dark interiors are not aligned. How can we understand this?

There are several possible plausible answers:

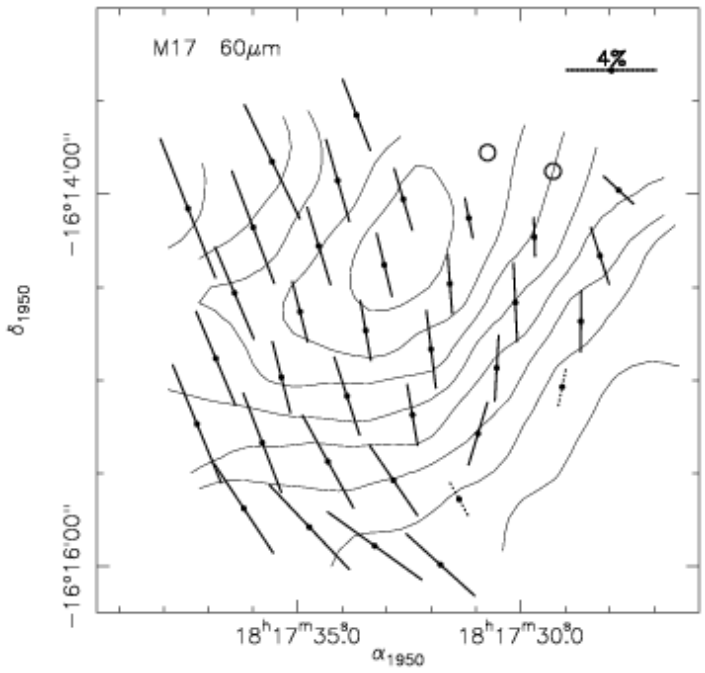

Fig. 37. 60 μm linear polarization toward M17. Flux contours are at 20%, 30%, ...,90% of the peak flux. From Dotson et al (2000).

- The inner dark regions have insufficient starlight for the radiative torques to achieve grain alignment.
- The inner dark regions are molecular, so that H_2 formation torques cannot drive suprathermal rotation.
- Photoelectric emission is suppressed in the inner dark regions.

It is also possible, of course, that either the magnetic field structure is completely tangled in the interior, or the grains in the central regions are for some reason more spherical, but these do not seem plausible.

It is also interesting to note that in some dark clouds the grains are reasonably well aligned: for example, the M17 molecular cloud (Fig. 37) shows linear polarization (averaged over the 22″ beam) as large as 5%. Note, though, that although this cloud is "dark" (i.e., we cannot see into it at optical wavelengths) it is full of stars – the infrared spectrum indicates a grain temperature $T \approx 45\,\mathrm{K}$, and the grains must be heated by starlight: the mean starlight intensity must be $\sim (45/20)^6 \approx 10^2$ times greater than the ISRF in order to heat the grains to this temperature! It therefore appears likely that starlight torques could drive the grains in this cloud to suprathermal rotation rates.

Finally, a recent study by Padoan et al. (2001) concluded that submm polarization maps of quiescent cores were consistent with a model where the grains in the outer parts of the cloud with $A_V \lesssim 3$ mag were aligned, while grains in regions with $A_V > 3$ mag were randomly oriented.

All of the above appear consistent with the idea that starlight torques are an essential part of the grain alignment process. Grains deep in quiescent dark clouds are unable to align because starlight torques are weak or absent, whereas starlight torques are present are do produce alignment within star-forming clouds.

7.9 Summary of the Grain Alignment Story

The grain alignment story has been long and complicated, with a number of false turns. The discussion above has skipped some of the important physics involving coupling of the grain rotation to the electron and nuclear spin systems (see Lazarian & Draine 1999a,b) as well as the important question of the grain dynamics during "crossovers", when reversals of the systematic torques on the grain cause the grain angular momentum to become small – during this time the grain is very vulnerable to disalignment (see, e.g., Lazarian & Draine 1997).

To summarize: the important elements of the grain alignment story now appear to be as follows:

- Grains are subject to 2 important systematic torques:
  - H_2 formation torques,
  - radiative torques due to starlight.
- For grains with rotational kinetic energies less than a few times kT_d, thermal fluctuations allow the grain to sample different orientations of the principal axes relative to the instantaneous angular momentum $\mathbf{J}$, leading to "thermal flipping" of the grain between the two "flip states".
- If the thermal flipping is sufficiently rapid, the grain will spend 50% of the time in each flip state, in which case the H_2 formation torque, which is fixed in body coordinates, will integrate to zero in inertial coordinates: the H_2 formation torque will be unable to drive the grain to suprathermal rotation.
- Starlight torques are not fixed in body coordinates, and hence do not integrate to zero even if the grain spends equal amounts of time in the two flip states.
- For grains with $a \gtrsim 0.1\,\mu$m in regions with sufficiently strong starlight, the systematic torque due to starlight will be able to drive the grain to suprathermal rotation.
- Once a grain achieves suprathermal rotation, thermal flipping will cease, the grain will settle into a state where the principal axis $\hat{\mathbf{a}}_1$ is either parallel or antiparallel to $\mathbf{J}$, and all systematic torques will operate simultaneously.

- Grains in suprathermal rotation are essentially immune from disalignment by random collisions. Alignment will result from the combined effects of Davis-Greenstein alignment and starlight torques.
- Under some circumstances, starlight torques do not result in strong alignment. However, numerical experiments suggest that, averaged over irregular grain shapes, starlight torques lead to overall alignment.
- The fact that starlight torques are important only for grains with $a \gtrsim 0.1\,\mu$m appears to account for the observation that $a \lesssim 0.05\,\mu$m grains in diffuse clouds are not aligned, while $a \gtrsim 0.1\,\mu$m grains appear to be well-aligned.

8 Evolution of the Grain Population

The interstellar grain population in a galaxy is the result of a rich and complicated mix of processes.

We would like to know the composition of interstellar dust, how and where it forms, and the extent to which individual grains are either homogeneous or conglomerate. We would like to know what the size distribution of the different types of grains is, how and where the size distribution is fashioned, and the manner in which the size distribution varies from one region to another. If we understood the balance of processes acting in our part of the Milky Way, perhaps we could deduce how grains might differ in the inner or outer parts of the Milky Way, and in the LMC, SMC, and other galaxies.

Unfortunately, the overall grain evolution problem seems to me to be beyond our grasp at this time – I don't think we understand the parts well enough to justify trying to put them together as a whole. At this time, we have to try to clarify the individual elements of the story.

8.1 Dust Formation in Stellar Outflows

There is abundant evidence that dust grains form in some stellar outflows: we see infrared emission from dust around red giants, around carbon stars, and in planetary nebulae. In all these cases the dust condensed out of material which at an earlier time was completely gaseous. Observations show that different types of stellar outflows form different types of dust.

The dust around red giants with O/C > 1 shows a $10\,\mu$m emission feature which is due to the Si-O stretching mode in amorphous silicate material; around some OH/IR stars the $10\,\mu$m feature appears in absorption (e.g., Demyk et al. 2000), along with emission features revealing the presence of crystalline silicates.

The dust around carbon stars, on the other hand, does not show the $10\,\mu$m feature, which is consistent with the fact that we do not expect silicates to form in an atmosphere with O/C < 1. Some carbon stars (e.g. IRC+10216) instead show a $11.3\,\mu$m emission feature which is attributed to SiC (e.g., Blanco et al. 1998).

It should also be mentioned that we find presolar grains in meteorites whose isotopic composition clearly indicates formation in outflows from evolved stars (Hoppe & Zinner 2000); these include nanodiamonds, SiC, graphite, and Al_2O_3. Some of these grains may have formed in supernova ejecta.

So there is no question that stellar outflows contribute dust to the interstellar medium. However, this does *not* necessarily imply that the bulk of the dust in the interstellar medium was formed in stellar outflows.

The physics and chemistry of dust formation in stellar outflows is complex: the material is generally far from thermodynamic equilibrium, and the outflows themselves are often (perhaps always?) hydrodynamically complex – neither steady nor spherically symmetric. We can not yet reliably describe the details of the grain formation process.

8.2 Grain Growth in the ISM

8.2.1 Accretion in the ISM

Dust grains in the interstellar medium can grow, since atoms from the gas can stick to them. We can calculate the lifetime against accretion for an atom or ion in the gas phase:

$$\tau^{-1} = A_i^{-1/2} s_i \left(\frac{8kT}{\pi m_{\rm H}}\right)^{1/2} \int da \pi a^2 \frac{dn_d}{da} D(a) \quad , \tag{125}$$

where A_i is the mass number of the ion, s_i is the sticking coefficient, and $n_d(a)$ is the number density of grains with radii less than a. The enhancement factor $D(a)$ gives the collision rate relative to what it would be in the absence of electrostatic effects:

$$D(a) = \sum_{Z_d} f(Z_d, a) B(Z_d, a) \quad , \tag{126}$$

where

$$B(Z_d, a) = \begin{cases} \exp\left(-Z_d Z_i e^2/akT\right) & \text{for } Z_g Z_i > 0 \\ \left(1 - \frac{Z_d Z_i e^2}{akT}\right) & \text{for } Z_g Z_i < 0 \\ 1 + \left(\frac{\pi Z_i^2 e^2}{2akT}\right)^{1/2} & \text{for } Z_g = 0 \end{cases} \quad . \tag{127}$$

Fig. 38 shows the collisional enhancement factor $D(a)$ calculated by Weingartner & Draine (1999) for carbonaceous and silicate grains in various environments. Enhancement factors $D \gtrsim \sim 10^2$ are found for $a \lesssim 10^{-7}$ cm grains in the CNM. As a result, an ion (e.g., SiII, TiII, FeII) would have a lifetime against accretion of $\sim 1 \times 10^5$ yr in the CNM if the grain size distribution includes the ultrasmall grain population of Fig. 10. Therefore we expect that those metals which can "stick" to the small grains will be strongly depleted

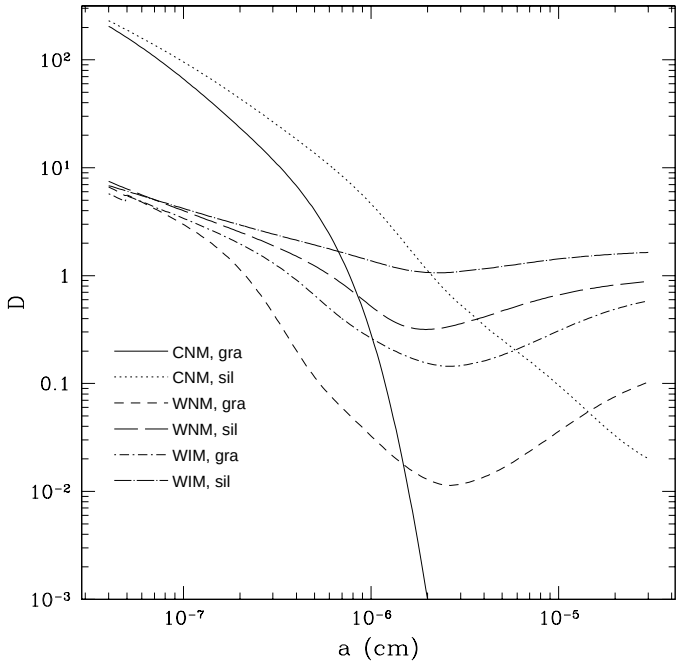

Fig. 38. Collision enhancement factor for positively charged ion (see text). From Weingartner & Draine (1999).

from the gas phase; presumably those elements which are not strongly depleted (e.g., Na, K, S) for some reason do not remain on the ultrasmall grains after they collide.

8.2.2 Mantle Formation

As discussed in §1.8, grains in dark molecular clouds are apparently coated with ice "mantles". The overall mantle composition is dominated by H_2O ice. It is not known whether the H_2O molecules arrived from the gas phase and then froze onto the grain, or whether the H_2O formed by surface chemistry. In most clouds the gas phase H_2O abundance is very low, and the observed mantles would not be able to form by accretion, suggesting that O and H atoms arriving at the grain react there to form H_2O (Jones & Williams 1984). However, it has recently been proposed that the H_2O could be produced in the gas phase during occasional passage of a shock wave, and then quickly accreted onto the grain surfaces (Bergin et al. 1999). Other molecules (e.g., CO) may be mixed with the H_2O, or in some cases condensed separately, as the absorption profile in some cases requires that the CO not be mixed with polar molecules. This could result if the H_2O was deposited while the

grain was too warm to retain CO, with the CO later freezing out when the conditions changed and the grain became colder.

8.2.3 Coagulation

The grain population in normal diffuse clouds has a very large population of very small grains, required to explain the rapid rise in extinction at short wavelengths. In dense regions, however, the extinction at short wavelengths appears to be reduced. This can only happen if some of the small grains are either destroyed altogether, or simply coagulated onto big grains. The latter seems more likely.

What is the time scale for such coagulation? This depends on the velocity differences between different grains. Grain-grain velocities can be the result of differential drift velocities (see §5.5), hydrodynamic turbulence (see, e.g., Draine 1985), or MHD turbulence (Lazarian & Yan 2002).

Grains larger than $\sim 10^{-5}\,$cm contribute a geometric cross section per H $\Sigma \approx 0.5 \times 10^{-21}\,\mathrm{cm}^2$. If the characteristic grain-grain velocity difference is Δv_d, then the grain-grain coagulation time would be

$$t_{coag} = [n_{\rm H}\Sigma\Delta v_d]^{-1} = 2\times 10^8\,{\rm yr}\left(\frac{30\,{\rm cm}^{-3}}{n_{\rm H}}\right)\left(\frac{0.1{\rm km\,s}^{-1}}{\Delta v_d}\right) \quad , \qquad (128)$$

so that grain coagulation will not be very important in diffuse clouds, but could proceed in dense regions.

8.3 Photolysis

When grains with ice mantles are returned to diffuse regions and exposed to ultraviolet radiation, it appears that most of the material is driven off, but the ultraviolet radiation photolyzes the ice to produce an organic refractory residue (e.g., Greenberg et al. 2000). This residue may be responsible for the interstellar $3.4\,\mu$m "aliphatic C-H" absorption band.

8.4 Photodesorption

The process of photodesorption is potentially very important, but is unfortunately not well understood because of limited laboratory studies. Photodesorption is a quantum process whereby absorption of a single photon can lead to ejection of an atom or molecule from a solid. For example, an absorbed photon might cause an atom or molecule on a substrate to be excited to a repulsive electronic state which would then be ejected from the substrate.

Photodesorption was discussed by Draine & Salpeter (1979b), who argued that a molecule in a surface monolayer might have a photodesorption cross section as large as $\sim 10^{-18}\,\mathrm{cm}^2$.

If an atom or molecule adsorbed on a grain surface has a cross section $\sigma_{pd} = 10^{-18}\sigma_{-18}\,\mathrm{cm}^2$ for $8 < h\nu < 13.6\,$eV photons, the photodesorption rate

for an adsorbed atom or molecule would be $\sim 6\times10^{-11}\sigma_{18}\,\mathrm{s}^{-1}$ in the diffuse ISM, since the density of $8-13.6\,\mathrm{eV}$ photons is $\sim 2.0\times10^{-3}\,\mathrm{cm}^{-3}$ in the MMP ISRF. Laboratory studies show that H_2O ice has a photodesorption cross section $\sigma_{pd}\approx 8\times10^{-18}\,\mathrm{cm}^2$ at $\lambda = 1215$Å (Westley et al. 1995a, 1995b), so that it seems likely that at least some species will have $\sigma_{-18}\gtrsim 1$, with photodesorption rate $\gtrsim 6\times10^{-11}\,\mathrm{s}^{-1}$. Note that this estimated photodesorption rate is comparable to photodissociation rates for diatomic molecules in the interstellar radiation field.[2]

O is the most abundant species after H and He. The probability per unit time that an O atom will arrive at a single surface site (of area $\sim 10^{-15}\,\mathrm{cm}^2$) is $\sim 2\times10^{-13}\,\mathrm{s}^{-1}$ in the CNM. It is therefore apparent that any species with $\sigma_{18}\gtrsim .01$ will be photodesorbed before accretion of anything chemically interesting (other than H) can take place on top of it.

We conclude that photodesorption most likely plays a dominant role in determining what kind of accretional growth takes place on a grain. It is no surprise that the noble gases (He, Ne, Ar) do not deplete, but the fact that some chemically-reactive elements (e.g., Na, K, S) appear to undergo minimal depletion, at least in the diffuse ISM, may be due to photodesorption.[3] Laboratory studies of photodesorption from carbonaceous or silicate substrates would be of great value to clarify why some elements deplete and others do not in the diffuse ISM.

8.5 Grain Destruction in Shock Waves

From time to time a shock wave will pass through an element of interstellar gas, compressing, heating, and accelerating the gas (Draine & McKee 1993), and creating conditions under which grain destruction can occur (Draine 1995). Shock waves can be driven into cold cloud material ahead of an ionization/dissociation front (Bertoldi & Draine 1996), as the result of energetic outflows from newly-formed stars, or as the result of the explosion of a nearby supernova.

It is easiest to study the shock in the "shock frame" where the shock front is stationary: in the upstream direction the grains and gas move together toward the shock with a speed equal to the shock speed v_s. The fluid is then decelerated at the shock front, with the postshock gas velocity $v_g\approx v_s/4$ for a strong shock. The postshock gas is initially hot. If the shock is strong, and we can neglect the effects of a possible magnetic precursor, the gas temperature will rise to

$$T_s \approx \frac{3}{16k}\mu v_s^2 = 2300\times\,\mathrm{K}\left(\frac{\mu}{m_\mathrm{H}}\right)\left(\frac{v_s}{10\mathrm{km\,s}^{-1}}\right)^2 \quad , \tag{129}$$

[2] Roberge et al. (1991) estimate photodissociation rates $8.6\times10^{-10}\,\mathrm{s}^{-1}$ and $3.5\times10^{-10}\,\mathrm{s}^{-1}$ for CH and OH, respectively.

[3] The only other depletion-suppressing process would be chemisputtering by H atoms: an impinging H atom might react with the adsorbed atom, and the reaction energy might eject the resulting hydride.

where μ is the mass per free particle ($\mu/m_{\rm H} \approx 1.4/1.1 = 1.27$ for cold atomic clouds, and $\mu/m_{\rm H} = 1.4/0.6 = 2.33$ for molecular gas, where we assume He/H=0.1).

The grains move across the shock front into the postshock fluid, where they initially have velocity $v_s - v_g \approx (3/4)v_s$ relative to the gas. The grains now begin to decelerate by gas drag, but are also acted on by the magnetic field $\mathbf{B}$ and electric field $\mathbf{E} = -\mathbf{v}_g \times \mathbf{B}/c$ (evaluated in the shock frame). As a result, the grain population develops grain-grain velocity differences which can be of order the shock speed v_s, or even larger if conditions are favorable for "betatron" acceleration of the dust as the density and magnetic field increase in cooling postshock gas (Spitzer 1976; Draine & Salpeter 1979b).

8.5.1 Grain-Grain Collisions

In the absence of betatron acceleration, a grain will slow down by a factor $1/e$ when it has collided with its own mass of gas. If all grains were identical, then the chance that a grain would run into another grain before appreciable slowing-down would be of order the dust-to-gas mass ratio of ~ 0.01, and we can therefore expect that a typical grain (one representative of the bulk of the grain mass) will have a probability of ~ 0.01 of collision with another comparable grain with a grain-grain velocity difference $\sim v_s$.

The physics of grain-grain collisions has been discussed by Tielens et al. (1994). For refractory grains one expects virtually complete destruction if the energy in the center-of-mass system is sufficient to vaporize both grains. For identical grains, mean atomic mass 20 amu, and binding energy per atom of 5.7 eV (these numbers are appropriate to $MgFeSiO_4$ silicate) complete vaporization could occur in a head-on collision between identical grains with a velocity difference of 15 km s^{-1}, so we may expect vaporization of perhaps of $\sim 1\%$ of the grains in a hydrodynamic shock with shock speed $v_s \gtrsim 20$km s^{-1}. At lower grain-grain collision speeds, shattering may occur. Thus we should expect that several percent of the large dust grains will be shattered in shocks with $v_s \gtrsim 10$km s^{-1}. Grain-grain collisions may be responsible for maintaining the population of small grains in the interstellar medium.

8.5.2 Sputtering

In a fast shock, the grain material can be eroded by the process of "sputtering", where individual atoms or ions from the gas collide with the grain, occasionally ejecting one of the grain atoms. In interstellar gas, the sputtering rate depends mainly on the sputtering "yields" $Y(E)$ for H and He projectiles incident on silicate or carbonaceous target materials. In ionized gas the sputtering rates will be affected by the grain charge. An expression for the rate of sputtering of a moving grain, and estimates for sputtering yields Y, are given by Draine & Salpeter (1979a).

In the initial postshock region where the gas is hot, the sputtering is due to a combination of thermal energy and the motion of the grain through the gas with velocity $\sim 3v_s/4$. If the gas cools before the grain slows down, then

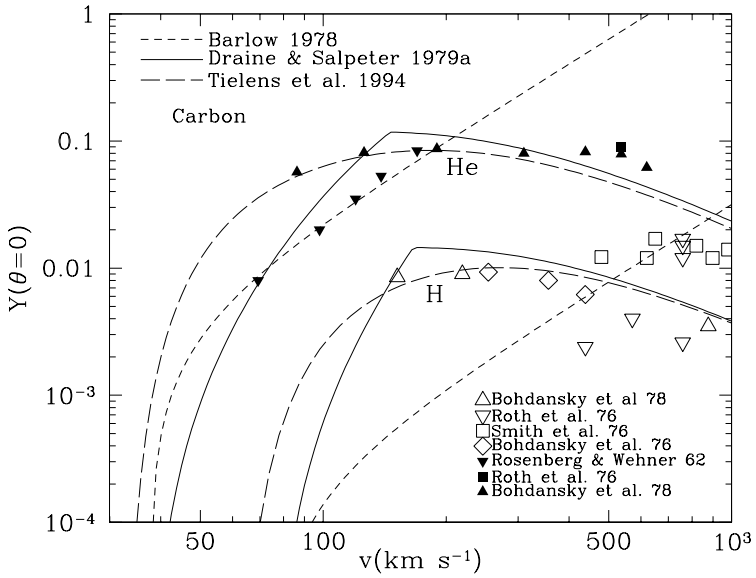

Fig. 39. Sputtering yields for H and He on carbon estimated by Barlow (1978), Draine & Salpeter (1979a), and Tielens et al. (1994), and compared with laboratory data.

subsequent sputtering is entirely due to the rapid motion of the grain through the gas, with He atoms having kinetic energies 4 times larger than H atoms. The sputtering continues until the grain slows to the point where the kinetic energy of the impinging He atoms is too low for appreciable sputtering.

Detailed models of grain destruction in shock waves are in general agreement that shock speeds $v_s \gtrsim 100\mathrm{km\,s^{-1}}$ result in substantial grain destruction, with essentially complete grain destruction for $v_s > 200\mathrm{km\,s^{-1}}$ in the case of a radiative shock – see Fig. 41 (Draine & Salpeter 1979b; Jones et al. 1994).

These estimates for grain destruction sppear to be in agreement with the observation that high-velocity gas (which has been shocked) tends to have enhanced gas phase abundances of elements, such as Si, which are normally heavily depleted in interstellar gas, an effect first noted for Ca by Routly & Spitzer (1952). Fig. 42 shows this effect for Si.

8.6 Thermal Sublimation

Ice mantles on grains can be removed if the grains become too warm. What is the critical grain temperature for ice mantle removal?

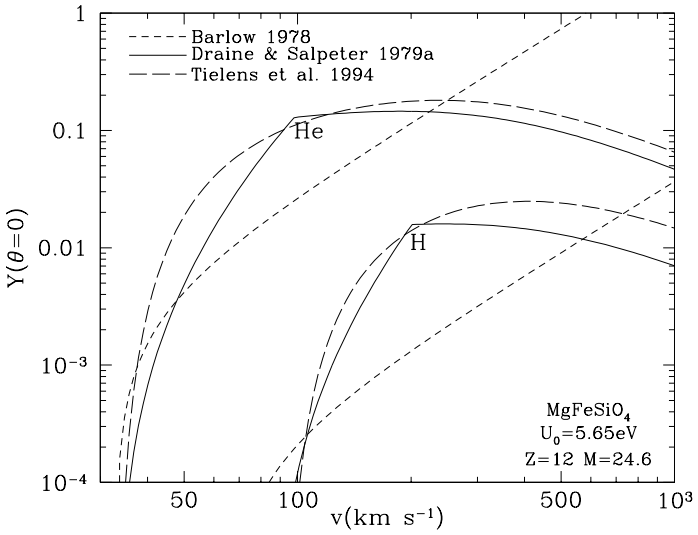

Fig. 40. Sputtering yields for H and He on silicate material estimated by Barlow (1978), Draine & Salpeter (1979a), and Tielens et al. (1994).

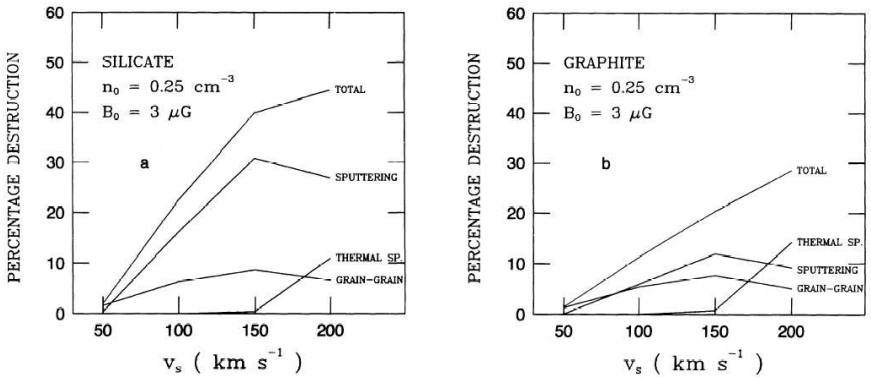

Fig. 41. Fractional grain destruction calculated for graphite and silicate grains in interstellar shock waves in low density gas. Figure from Jones et al. (1994).

The probability per unit time for a surface molecule to desorb is approximately

$$\frac{dP}{dt} = \nu_0 e^{-U_0/kT} \quad , \tag{130}$$

where U_0 is the binding energy of the molecule, and $\nu_0 \approx 10^{13}\,\mathrm{s}^{-1}$ is a characteristic vibration frequency. If there are $N_{\rm mono}$ monolayers of ice on the grain and we want it to survive a time Δt, the grain temperature should not

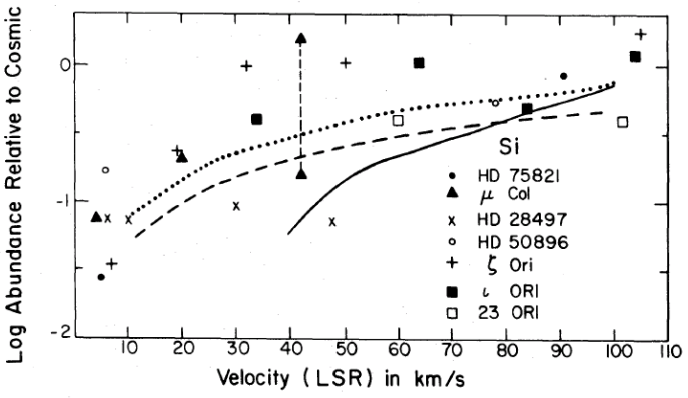

Fig. 42. Observed gas-phase Si abundances: evidence for refractory grain destruction in high-velocity shocks. Solid, dashed, and broken lines are theoretical models discussed by Cowie (1978). Figure from Cowie (1978).

exceed

$$T_{\rm sub} = \frac{U_0/k}{\ln(\nu_0 \Delta t/N_{\rm mono})} \tag{131}$$

Some heating phenomena are brief (e.g., a stellar flare or a supernova) but we are usually interested in longer time scales. For example, a massive star in or near the cloud might have a lifetime $\Delta t \approx 5 \times 10^6$ yr. We can write

$$T_{\rm sub} = \frac{U_0/54k}{1 + 0.018 \ln[(\Delta t/10^6\,{\rm yr})(10^3/N_{\rm mono})]} \tag{132}$$

Thus, a H_2O ice mantle ($U_0 = 0.5\,{\rm eV}$) 10^3 monolayers thick will survive 10^6 yr provided $T < 108\,{\rm K}$. Therefore we should not be surprised to find H_2O ice in clouds where the grain temperature is 80 K (as in the molecular cloud OMC-1), but it would be a great surprise to find H_2O ice if the grain temperature were, say, 120K.

8.7 Gamma Ray Bursts

Gamma ray bursts may destroy dust grains out to a substantial distance. While this is probably uninteresting in terms of evolution of the overall grain population in galaxies, it may nevertheless be of observational interests because it affects the observable properties of gamma-ray bursts. This is of considerable interest because there is evidence that gamma-ray bursts are associated with star-forming regions in galaxies, and yet the optical afterglows from a number of bursts show little evidence for reddening.

Grain destruction near GRBs has been discussed by Waxman & Draine (2000), Fruchter, Krolik & Rhoads (2001), and Draine & Hao (2002). There

are two separate mechanisms which could be important. Thermal sublimation (as discussed above, but now with larger binding energies $U_0/k \approx 7 \times 10^4\,\mathrm{K}$ and shorter times $\Delta t \approx 10\,\mathrm{s}$ for the optical transient, so the grain temperature can rise to $\sim 3000\,\mathrm{K}$. Draine & Hao find that for a reasonable (but very uncertain) estimate of the GRB peak optical luminosity, dust grains can be destroyed out to distances of ∼5 pc.

A more exotic grain destruction mechanism may operate; if effective, it could destroy grains out to greater differences. This is the mechanism of "Coulomb explosion" (Waxman & Draine 2000). The grains will be quite highly charged due to the intense X-ray irradiation from the GRB. If the grains are sufficiently weak, the electrostatic stresses on the grain might conceivably tear it apart. Fruchter et al give arguments in favor of this outcome, in which case GRBs could destroy grains out to quite large distances.

8.8 Time Scales

When all grain destruction processes are considered, it is found that sputtering in shock waves dominates the overall destruction of refractory grains. The frequency with which grains are overtaken by such shocks depends on the frequency of the supernovae which drive these blastwaves, and on the structure of the interstellar medium, since material in dense regions is "sheltered" from the effects of a passing blastwave. The problem is complex, and therefore there are many places where different assumptions could alter the quantitative conclusion, but Draine & Salpeter (1979b) estimated a lifetime $\sim 1.3 \times 10^8\,\mathrm{yr}$ for silicate material in a diffuse cloud, while Jones et al. (1994) find a lifetime $2.2 \times 10^8\,\mathrm{yr}$ for silicate grains.

Draine & Salpeter (1979b) stress that this relatively short lifetime was impossible to reconcile with the idea that "interstellar grains are stardust": nearly all of the Si in the interstellar medium is in solid form (e.g., see Fig. 9, showing that only 2.5% of the Si is in the gas phase in the cloud toward ζOph). The "turnover" time of the interstellar medium is equal to the ratio of (mass in gas)/(rate of mass going into stars), or $\sim 5{\times}10^9 M_\odot / 5 M_\odot\,\mathrm{yr}^{-1} \approx 1{\times}10^9\,\mathrm{yr}$. Suppose that all the Si leaving stars entered the ISM in solid form, but there was no grain growth in the ISM. A grain destruction time $\sim 2 \times 10^8\,\mathrm{yr}$ – only ∼20% of the turnover time – would imply that ∼ 80% of the Si would be found in the gas phase. However, observations of diffuse clouds typically show $< 10\%$ of the Si in the gas gas phase (see, e.g., Fig. 9).

The ineluctable conclusion is that *most* of the Si atoms in grains must have joined those grains in the ISM through some process of grain growth. The kinetics of accretion implies that only in denser regions can accretion rates be large enough to remove Si from the gas fast enough to maintain the low observed gas-phase abundances. This in turn requires that there must be fairly rapid exchange of mass between the dense and less dense phases of the ISM. A more quantitative discussion of the required mass exchange rates may be found in Draine (1990) and Weingartner & Draine (1999).

9 Effects of Dust on Interstellar Gas

9.1 Photoelectric Heating

Photoelectrons emitted from dust grains depart with nonzero kinetic energy. This is often the dominant mechanism for heating interstellar gas, whether in diffuse clouds or in photodissociation regions.

Photoelectric heating rates have been reestimated recently by Bakes & Tielens (1994) and Weingartner & Draine (2001c). For starlight with the spectrum of the ISRF, Weingartner & Draine find a heating rate per H nucleon $\Gamma/n_{\rm H} \approx 6\times10^{-26}\,{\rm erg\,s^{-1}}$ for conditions characteristic of cool H I clouds. This heating rate is much larger than other heating mechanisms, such as ionization by cosmic rays or X-rays.

9.2 H_2 Formation and Other Chemistry

The H_2 molecule is central to interstellar chemistry. The rovibrational lines can be an important coolant for gas at temperatures $100 \lesssim T \lesssim 2000\,{\rm K}$.

The principal gas-phase formation processes are via H^-

$$H + e^- \rightarrow H^- + h\nu \quad ; \quad H^- + H \rightarrow H_2 + e^- \tag{133}$$

or 3-body collisions:

$$H + H + X \rightarrow H_2 + X + \Delta E \tag{134}$$

where the third body X could be H, He, or another H_2. The H^- formation pathway (133) is slow because of the generally low abundance of H^- in diffuse gas, and the 3 body process (134) requires very high densities to become important. In the interstellar medium of the Milky Way, the dust abundance is such that H_2 formation is overwhelmingly due to grain surface catalysis. The grain catalysis process was first proposed by Gould & Salpeter (1963), and the basic picture has not changed:

1. An H atom arrives at a grain surface and "sticks".
2. The H atom diffuses over the grain surface until it becomes trapped by either chemisorption or physisorption
3. A second H atom arrives at the surface, sticks, diffuses over the surface, and encounters the trapped H atom.
4. The two H atoms react to form H_2, releasing $\sim 4.5\,{\rm eV}$ of energy, and ejecting the H_2 from the grain surface into the gas.

Part of the 4.5eV goes into overcoming the binding of the two H atoms to the surface, part goes into vibrational excitation of the grain lattice ("heat"), part appears as kinetic energy of the H_2, and part appears in vibrational and rotational energy of the newly-formed H_2 molecule.

In the above picture, the H_2 formation rate is

$$\frac{dn(H_2)}{dt} = Rn_H n(H) \tag{135}$$

$$R = \frac{1}{2}\left(\frac{8kT}{\pi m_H}\right)^{1/2} \int da \frac{1}{n_H}\frac{dn_d}{da}\pi a^2 \gamma(a) \tag{136}$$

$$= 7.3\times10^{-17}\,\mathrm{cm^3\,s^{-1}}\left(\frac{T}{100\,\mathrm{K}}\right)^{1/2}\frac{A\langle\gamma\rangle}{10^{-21}\,\mathrm{cm^2H^{-1}}} \tag{137}$$

$$A \equiv \int da(1/n_H)(dn_d/da)\pi a^2 \tag{138}$$

$$\langle\gamma\rangle \equiv \frac{1}{A}\int da(1/n_H)(dn_d/da)\pi a^2\gamma(a) \tag{139}$$

where $\gamma(a)$ is the fraction of H atoms colliding with a grain of radius a which are converted to H_2; $\gamma < 1$ since not all impinging H atoms will "stick", and some of those which stick may later be removed from the surface by some process other than H_2 formation. Gould & Salpeter argued for γ of order unity under interstellar conditions.

Dust models which reproduce the observed extinction of starlight have

$$A \equiv \int da \frac{1}{n_H}\frac{dn_d}{da}\pi a^2 \gtrsim 10^{-21}\,\mathrm{cm^2} \tag{140}$$

For example, the dust model of Weingartner & Draine (2001a) has $A = 6.7\times10^{-21}\,\mathrm{cm^2/H}$. The H_2 formation "rate coefficient" R can be determined from ultraviolet observations of H_2 in diffuse regions; Jura (1975) found $R \approx 3\times10^{-17}\,\mathrm{cm^3\,s^{-1}}$, which implies $\langle\gamma\rangle \approx 0.06$. It appears, then, that the very small grains which dominate the grain surface area (in particular, the PAHs) must not be efficient catalysts for H_2 formation.

How might H_2 formation on the smallest grains be suppressed? The time scale between photon absorption events is

$$\tau_{\rm abs} \approx 10^6\,\mathrm{s}(10\text{Å}/a)^3 \quad , \tag{141}$$

while the time scale between arrival of H atoms is

$$\tau_H \approx 8\times10^6\,\mathrm{s}\left(\frac{10\text{Å}}{a}\right)^2\left(\frac{30\,\mathrm{cm^{-3}}}{n_H}\right)\left(\frac{100\,\mathrm{K}}{T}\right)^{1/2} \tag{142}$$

so it is possible that an H atom physisorbed on a very small grain may be removed when the grain is heated by a photon absorption event, so that only rarely would an arriving H atom find another H atom with which to recombine. The efficacy of this process depends on the binding energy of the H atom.

9.3 Grains as Sources of Complex Molecules

Observational studies of star-forming regions sometimes find molecular abundances in the gas phase which are difficult to understand in the context of pure gas-phase chemistry. An extreme example of this is the observation of D_2CO/H_2CO=0.003 toward Orion (Turner 1990), or D_2CO/H_2CO=0.03-0.16 toward the low-mass protostar IRAS 16293-2422 (Ceccarelli et al 2001). Such extreme deuteration seems impossible to envision in the gas phase, but could occur by chemistry on grain mantles during a precollapse phase, with the molecules put into the gas phase when the dust is warmed by energy from the protostar. There seems little doubt that at least some regions have molecular abundances which are heavily influenced by grain surface chemistry.

9.4 Ion Recombination on Dust Grains

In diffuse clouds, the ion/neutral fraction elements with ionization potentials $< 13.6\,\mathrm{eV}$ is indicative of the relative rates for photoionization of starlight vs. recombination of ions with electrons. It is often assumed that the only channel for neutralization of metal ions X^+ is radiative recombination, $X^+ + e^- \rightarrow X + h\nu$. However, collisions with neutral or negatively charged grains can be more important than radiative recombination for neutralization of metal ions for conditions typical of the diffuse interstellar medium (Weingartner & Draine 2001d). Weingartner & Draine provide estimates for the effective "rate coefficient" for ion neutralization via collisions with dust grains. Recombination on dust grains is particularly effective for protons in H I regions, and therefore is involved in regulating the free electron density.

9.5 Coupling Neutral Gas to Magnetic Fields

In gas of low fractional ionization, a significant fraction of the "free" charge present may be located on dust grains. The fraction of the free charge residing on the grains depends very much on the numbers of very small dust grains, but appears likely to become significant in regions of low fractional ionization $n_e/n_\mathrm{H} \lesssim 10^{-6}$ (Draine & Sutin 1987).

Coupling of the magnetic field to the gas is due to the force exerted on moving charges; in regions of low fractional ionization, the neutral gas will be unaffected by the magnetic field unless the charged species are collisionally coupled to the neutral atoms and molecules. Because dust grains have relatively large physical cross sections, the charge trapped on dust grains can be important at coupling the magnetic field to the neutral gas in MHD shocks in gas with fractional ionization $n_e/n_\mathrm{H} \lesssim 10^{-7}$ (Draine 1980; Draine, Roberge & Dalgarno 1983).

9.6 Dust Grains as Magnetometers?

Magnetic fields are dynamically important in the ISM, but difficult to observe remotely. Nature has been kind enough to strew microscopic magnetometers – dust grains – throughout the interstellar medium. Unfortunately we have not yet figured out how these magnetometers work, so that even if we could measure their degree of alignment, we would not be able to determine the magnetic field strength. But we *can* use dust grains as "compasses" to indicate the *direction* of the magnetic field.

As discussed above, dust grains have their angular momenta $\mathbf{J}$ systematically aligned with the magnetic field $\mathbf{B}_0$, at least in regions where sufficient starlight is present. Here we review the main features of this alignment:

- It is virtually certain that the sense of alignment is to have $\mathbf{J} \parallel \mathbf{B_0}$ (to within a sign – parallel and antiparallel are equally favored).
- Suppose the grain has 3 principal axes $\hat{\mathbf{a}}_1$, $\hat{\mathbf{a}}_2$, and $\hat{\mathbf{a}}_3$, with moments of inertia $I_1 \geq I_2 \geq I_3$. If the grain has rotational kinetic energy $E_{\rm rot} > (3/2)kT_{\rm gr}$, then the grain will tend to have its shortest axis $\hat{\mathbf{a}}_1 \parallel \mathbf{J}$ so as to minimize its rotational kinetic energy at constant $\mathbf{J}$. In regions where the grains are cooler than the gas (the most common situation), this is expected to be true for both large grains (which rotate suprathermally) and small grains (which rotate thermally).
- Thus we expect the grains to have their "long axes" $(\hat{\mathbf{a}}_2, \hat{\mathbf{a}}_3) \perp \mathbf{B_0}$.
- Starlight extinction will be greatest for starlight with $\mathbf{E} \parallel$ the long axes, and therefore we expect the transmitted starlight to have $\mathbf{E} \parallel \mathbf{B}_0$.
- Far-infrared and submm emission will be polarized $\parallel$ to the grains' long axes, and hence we expect the FIR/submm emission to be polarized with $\mathbf{E} \perp \mathbf{B}_0$.

Therefore we can obtain a map of the magnetic field by either measuring the polarization of starlight for many stars, or by mapping the polarized far-infrared or submm emission from the cloud. CCDs and infrared detectors make possible extensive measurements of starlight polarization, even in dense regions, and FIR/submm arrays (e.g., SCUBA on the JCMT) make possible measurements of polarized submm emission.

Grains are likely to have a fairly high polarizing efficiency in the FIR/submm. Define

$$C_{\rm pol} \equiv \frac{1}{2}\left[C(\mathbf{E} \parallel \hat{\mathbf{a}}_2) + C(\mathbf{E} \parallel \hat{\mathbf{a}}_3)\right] - C(\mathbf{E} \parallel \hat{\mathbf{a}}_1) \tag{143}$$

$$C_{\rm ran} \equiv \frac{1}{3}\left[C(\mathbf{E} \parallel \hat{\mathbf{a}}_1) + C(\mathbf{E} \parallel \hat{\mathbf{a}}_2) + C(\mathbf{E} \parallel \hat{\mathbf{a}}_3)\right] \tag{144}$$

If the grains were spherical, there would of course be no polarization in extinction or emission. Fig. 43 shows how the polarizing efficacy depends on the axial ratio of the dust grains. The grains are assumed to be either oblate

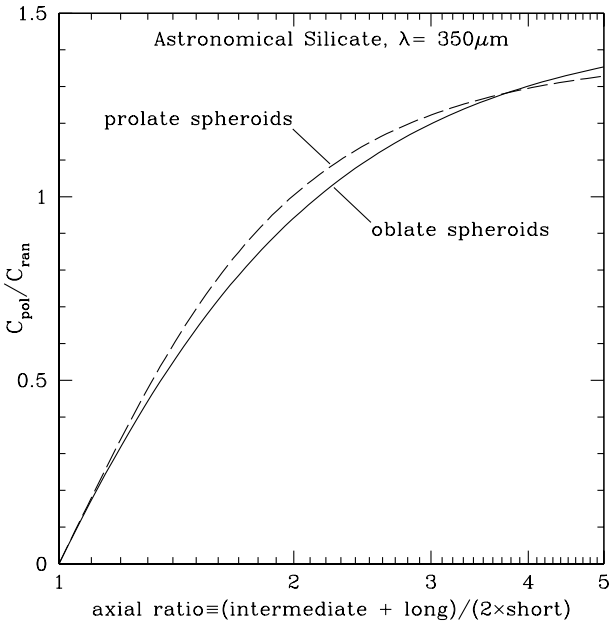

Fig. 43. Polarization efficiency $C_{\rm pol}/C_{\rm ran}$ for spheroidal dust grains (oblate and prolate) as a function of the axial ratio. From Padoan et al. (2001).

or prolate spheroids, and the dielectric function of the grains is taken to be that of "astronomical silicate" at 350 μm.

For perfect spinning alignment, the maximum polarization is obtained for a sightline $\perp \mathbf{B}_0$:

$$P_{\rm max} = \frac{C_2 + C_3 - 2C_1}{C_2 + C_3 + 2C_1} = \frac{C_{\rm pol}/C_{\rm ran}}{1 - \frac{1}{6}\frac{C_{\rm pol}}{C_{\rm ran}}} \tag{145}$$

Suppose the grain shape has (intermediate+long)/(2×short) = 1.4 (e.g., axial ratios 1:1.2:1.6). Then $C_{\rm pol}/C_{\rm ran} \approx 0.5$ for astronomical silicate. Perfect alignment would give polarization in emission $P = 0.5/(1 - .08) = 0.55$. However, the largest observed polarizations are $\sim 10\%$, implying either

- imperfect alignment
- less elongation
- disorder in the magnetic field on short length scales.

Unfortunately, it will be difficult to determine the relative importance of these three effects. For perfectly aligned grains in a uniform magnetic field perpendicular to the line-of-sight, $P = 0.1$ would be produced by grains with axial ratio of only ~ 1.05 – very minimal elongation.

10 Concluding Remarks

There are many unanswered questions in the astrophysics of interstellar dust grains in cold clouds. The questions are interesting in their own right, but one is also driven to answer them by the need to understand dust grains well enough to use them as diagnostics of interstellar conditions, and to understand the effects which dust grains have on the dynamics and evolution of interstellar gas. With the advent of powerful infrared and submillimeter observing facilities – including *SIRTF, SOFIA, ALMA, Herschel,* and *Planck* – we can anticipate that there will be progress on the astrophysics of dust, driven by the challenge of understanding the new data. An exciting decade lies before us!

I thank Robert Lupton for making available the SM software package. This work was supported in part by NSF grant AST 9988126.

References

1. Agladze, N.I., Sievers, A.J., Jones, S.A., Burlitch, J.M., & Beckwith, S.V.W. 1996: Ap. J., **462**, 1026-1040
2. Allamandola, L.J., Hudgins, D.M., & Sandford, S.A. 1999: Ap. J., Lett., **511**, L115-L119
3. Arendt, R.G., et al. 1998: Ap. J., **508**, 74-105
4. Asano, S., & Sato, M. 1980: Appl. Opt., **19**, 962
5. Asano, S., & Yamamoto, G. 1975: Appl. Opt., **14**, 29
6. Ashcroft, N.W., & Mermin, N.D. 1976: Solid State Physics (New York: Holt, Rinehart, and Winston)
7. Bakes, E.L.O., & Tielens, A.G.G.M. 1994: Ap. J., **427**, 822-838
8. Barlow, M.J. 1978: M.N.R.A.S, **183**, 367-395
9. Barnett, S.J. 1915: Phys. Rev. **6**, 239-270
10. Bergin, E.A., Neufeld, D.A., & Melnick, G.J. 1999: Ap. J., Lett., **510**, L145-148
11. Bertoldi, F., & Draine, B.T. 1996: Ap. J., **458**, 222-232
12. Blanco, A., Borghesi, A., Fonti, S., & Orofino, V. 1998: Astr. Ap., **330**, 505-514
13. Bohdansky, J., Roth, J., Sinha, M.K. 1976: in *Proc. 9th Symp. on Fusion Technology* (London: Pergamon), p. 541
14. Bohdansky, J., Bay, H.L, & Ottenberger, W. 1978: J. Nucl. Mat., **76**, 163
15. Bohren, C.F., & Huffman, D.R. 1983: Absorption and Scattering of Light by Small Particles (New York: Wiley)
16. Bouchet, P., Lequeux, J., Maurice, E., Prévot, L., & Prévot-Burnichon, M.L. 1985: Astr. Ap., **149**, 330-336
17. Boulanger, F., Boissel, P., Cesarsky, D., Ryter, C. 1998: Astr. Ap., **339**, 194-200
18. Boulanger, F., & Pérault, M. 1988: Ap. J., **330**, 964-985
19. Cardelli, J.A., Clayton, G.C., & Mathis, J.S. 1989: Ap. J., **345**, 245-256
20. Cardelli, J.A., Mathis, J.S., Ebbets, D.C., & Savage, B.D. 1993: Ap. J., Lett., **402**, L17-20
21. Ceccarelli, C., Loinard, L, Castets, A., Tielens, A.G.G.M., Caux, E., Lefloch, B., & Vastel, C. 2001: Astr. Ap., **372**, 998-1004

22. Cesarsky, D., Lequeuex, J., Abergel, A., Perault, M., Palazzi, E., Madden, S., & Tran, D. 1996: Astr. Ap., **315**, L305-308
23. Clayton, G.C., Anderson, C.M., Magalhaes, A.M., Code, A.D., Nordsieck, K.H. et al. 1992: Ap. J., Lett., **385**, L53-57
24. Cowie, L.L. 1978: Ap. J., **225**, 887-892
25. Crinklaw, G., Federman, S.R., & Joseph, C.L. 1994: Ap. J., **424**, 748-753
26. Dale, D.A., Helou, G., Contursi, A., Silberman, N.A., & Kolhatkar, S. 2001: Ap. J., **549**, 215-227
27. Davis, L., & Greenstein, J.L. 1951: Ap. J., **114**, 206-240
28. Debye, P. 1909: Ann. Phys. (Leipzig), **30**, 57
29. Demyk, K., Dartois, E., Wiesemeyer, H., Jones, A.P., & d'Hendecourt, L. 2000: Astr. Ap., **364**, 170-178
30. de Oliveira-Costa, A., Kogut, A., Devlin, M.J., Netterfield, C.B., Page, L.A., & Wollach, E.J. 1997: Ap. J., **482**, L17-20
31. de Oliveira-Costa, A., Tegmark, M., Devlin, M.J., Haffner, L.M., Herbig, T., Miller, A.D., Page, L.A., Reynolds, R.J., & Tufte, S.L. 2000: Ap. J., **542**, L5-8
32. de Oliveira-Costa, A., Tegmark, M., Gutiérrez, C.M., Jones, A.W., Davies, R.D., Lasenby, A.N., Rebolo, R., & Watson, R.A. 1999: Ap. J., **527**, L9-12
33. de Oliveira-Costa, A., Tegmark, M., Page, L.A., & Boughn, S.P. 1998: Ap. J., **509**, L9-12
34. Dolginov, A.Z., & Mytrophanov, I.G. 1976: Ap. Sp. Sci., **43**, 291-317
35. Dotson, J.L., Davidson, J., Dowell, C.D., Schleuning, D.A., Hildebrand, R.H. 2000: Ap. J. Suppl., **128**, 335-370
36. Draine, B.T. 1978: Ap. J. Suppl., **36**, 595-619
37. Draine, B.T. 1980: Ap. J., **241**, 1021-1038
38. Draine, B.T. 1981: Ap. J., **245**, 880-890
39. Draine, B.T. 1985: in Protostars and Planets II, ed. D.C. Black & M.S. Matthews (Tucson: Univ. of Arizona Press), 621-640
40. Draine, B.T. 1988: Ap. J., **333**, 848-872
41. Draine, B.T. 1989a: in Interstellar Dust, Proceedings of IAU Symp. 135, ed. L.J. Allamandola & A.G.G.M. Tielens, (Dordrecht: Kluwer), 313-327
42. Draine, B.T. 1989b: in ESA, Infrared Spectroscopy in Astronomy, 93-98
43. Draine, B.T. 1990: in The Evolution of the Intestellar Medium. ed. L. Blitz, Astr. Soc. Pacific. Conf. Series, **12**, 193-205
44. Draine, B.T. 1995: in *Shocks in Astrophysics*, ed. T.J. Millar, Ap. Sp. Sci., **233**, 111-123
45. Draine, B.T. 2000: in Light Scattering by Nonspherical Particles: Theory, Measurements, and Applications, ed. M.I. Mishchenko, J.W. Hovenier, & L.D. Travis (San Diego: Academic Press), 131-145
46. Draine, B.T., & Flatau, P.J. 1994: J. Opt. Soc. Am. **A**, **11**, 1491-1499
47. Draine, B.T., & Flatau, P.J. 2000: http://xxx.lanl.gov/abs/astro-ph/0008151
48. Draine, B.T., & Goodman, J. 1993: Ap. J., **405**, 685-697
49. Draine, B.T., & Hao, L. 2002: Ap. J., **569**, 780-791
50. Draine, B.T., & Lazarian, A. 1998a: Ap. J., Lett., **494**, L19-22
51. Draine, B.T., & Lazarian, A. 1998b: Ap. J., **508**, 157-179
52. Draine, B.T., & Lazarian, A. 1999a: Ap. J., **512**, 740-754 (DL99a)
53. Draine, B.T., & Lazarian, A. 1999b: in Microwave Foregrounds, eds. A. de Oliveira-Costa & M. Tegmark, A.S.P. Conf. Series **181** (San Francisco: Astr. Soc. Pac.), 133-149

54. Draine, B.T., & Lee, H.-M. 1984: Ap. J., **285**, 89–108
55. Draine, B.T., & Li, A. 2001: Ap. J., **551**, 807-824
56. Draine, B.T., & Malhotra, S. 1993: Ap. J., **414**, 632-645
57. Draine, B.T., & McKee, C.F. 1993: Ann. Rev. Astr. Ap., **31**, 373-432
58. Draine, B.T., Roberge, W.G., & Dalgarno, A. 1983: Ap. J., **264**, 485-507
59. Draine, B.T., & Salpeter, E.E. 1979a: Ap. J., **231**, 77-94
60. Draine, B.T., & Salpeter, E.E. 1979b: Ap. J., **231**, 438-455
61. Draine, B.T., & Sutin, B. 1987: Ap. J., **320**, 803-817
62. Draine, B.T., & Tan, J.C. 2002: astro-ph/0208302
63. Draine, B.T., & Weingartner, J.C. 1996: Ap. J., **470**, 551-565
64. Draine, B.T., & Weingartner, J.C. 1997: Ap. J., **480**, 633-646
65. Dufour, R. J. 1984: in IAU Symp. 108, Structure and Evolution of the Magellanic Clouds, ed. S. van den Bergh & K.S. de Boer (Dordrecht: Reidel), 353-360
66. Duley, W.W., Scott, A.D., Seahra, S., & Dadswell, G. 1998: Ap. J., Lett., **503**, L183-185
67. Erickson, W.C. 1957: Ap. J., **126**, 480-492
68. ESA, 1997: The Hipparcos and Tycho Catalogues (ESA SP-1200)
69. Farafonov, V.G., Voshchinnikov, N.V., & Somsikov, V.V. 1996: Appl. Opt., **35**, 5412-5426
70. Ferrara, A., & Dettmar, R.-J. 1994: Ap. J., **427**, 155-159
71. Finkbeiner, D.P., Davis, M., & Schlegel, D.J. 1999: Ap. J., **524**, 867-886
72. Finkbeiner, D.P., Schlegel, D.J., Frank, C., & Heiles, C. 2002: Ap. J., **566**, 898-904
73. Fitzpatrick, E.L. 1999: P. A. S. P., **111**, 63-75
74. Fitzpatrick, E.L., Massa, D. 1986: Ap. J., **307**, 286-294
75. Fruchter, A., Krolik, J.H., & Rhoads, J.E. 2001: Ap. J., **563**, 597-610
76. Gillett, F.C., Forrest, W.J., Merrill, K.M., Soifer, B.T., & Capps, R.W. 1975: Ap. J., **200**, 609-620
77. Gillett, F.C., Jones, T.W., Merrill, K.M., & Stein, W.A. 1975: Astr. Ap., **45**, 77-81
78. Gilra, D.P. 1972: in The Scientific Results of OAO-2, ed. A.D. Code (NASA SP-310), p. 295
79. Gold, T. 1952: M.N.R.A.S, **112**, 215-218
80. Goodman, A.A., Jones, T.J., Lada, E.A., & Myers, P.C. 1995: Ap. J., **448**, 748-765
81. Goodman, J.J., Draine, B.T., & Flatau, P.J. 1991: Optics Lett., **16**, 1198-1200
82. Gordon, K.D., & Clayton, G.C. 1998: Ap. J., **500**, 816-824
83. Gould, R.J., & Salpeter, E.E. 1963: Ap. J., **138**, 393-407
84. Greenberg, J.M., Gillette, J.S., Muñoz, C., Guillermo, M., Mahajan, T.B., Zare, R.N., Li, A., Schutte, W.A., de Groot, M., & Mendoza-Gómez, C. 2000: Ap. J., Lett., **531**, L71-73
85. Hall, J.S. 1949: Science, **109**, 166
86. Hall, J.S., & Mikesell, A.H. 1949: A. J., **54**, 187-188
87. Harwit, M. 1970: Bull. Astron. Inst. Czech., **21**, 204-210
88. Hayakawa, S. 1970: Prog. Theor. Phys., **43**, 1224
89. Heger, M.L. 1922: Lick Obs. Bull., **10**, 146-147
90. Hiltner, W.A. 1949a: Science **109**, 165
91. Hiltner, W.A. 1949b: Ap. J., **109**, 471-478
92. Hoppe, P., & Zinner, E. 2000: J. Geophys. Res., **105**, 10371-10386

93. Jackson, J.D. 1975: Classical Electrodynamics (New York: Wiley), p. 154
94. Jenniskens, P., & Desert, F-X. 1994: Astr. Ap. Suppl., **106**, 39-78
95. Joblin, C., d'Hendecourt, L., Leger, A., & Maillard, J.P. 1990: Nature, **346**, 729-731
96. Jones, A.P., Tielens, A.G.G.M., Hollenbach, D.J., & McKee, C.F. 1994: Ap. J., **433**, 797-810
97. Jones, A.P., & Williams, D.A. 1984: M.N.R.A.S, **209**, 955-960
98. Jura, M. 1975: Ap. J., **197**, 575-580
99. Kerr, T.H., Hibbins, R.E., Fossey, S.J., Miles, J.R., Sarre, P.J. 1998: Ap. J., **495**, 941-945
100. Kim, S.-H., & Martin, P.G. 1995: Ap. J., **444**, 293-305
101. Kogut, A., Banday, A.J., Bennett, C.L., Górski, K.M., Hinshaw, G., & Reach, W.T. 1996a: Ap. J., **460**, 1-9
102. Kogut, A., Banday, A.J., Bennett, C.L., Górski, K.M., Hinshaw, G., Smoot, G.F., & Wright, E.L. 1996b: Ap. J., **464**, L5-L9
103. Landau, L. D., & Lifshitz, E.M. 1960: Electrodynamics of Continuous Media (New York: Pergamon)
104. Lazarian, A., & Draine, B.T. 1997: Ap. J., **487**, 248-258
105. Lazarian, A., & Draine, B.T 1999a: Ap. J., Lett., **516**, L37-40
106. Lazarian, A., & Draine, B.T. 1999b: Ap. J., Lett., **520**, L67-70
107. Lazarian, A., & Draine, B.T. 2000: Ap. J., Lett., **536**, L15-18
108. Lazarian, A., & Roberge, W.G. 1997: Ap. J., **484**, 230-237
109. Lazarian, A., & Yan, H. 2002: Ap. J., Lett., **566**, L105-108
110. Li, A., & Draine, B.T. 2001: Ap. J., **554**, 778-802
111. Li, A., & Draine, B.T. 2002: Ap. J., **576**, 762-772
112. Martin, C., Arakawa, E.T., Callcott, T.A., & Warmack, R.J. 1987: J. Electr. Spectrosc. Rel. Phenom., **42**, 171-175
113. Martin, P.G. 1971: M.N.R.A.S, **153**, 279-285
114. Mathewson, D.S., & Ford, V.L. 1970: Mem.R.A.S., **74**, 139
115. Mathis, J.S., Cohen, D., Finley, J.P., & Krautter, J. 1995: Ap. J., **449**, 320-329
116. Mathis, J.S., Mezger, P.G., & Panagia, N. 1983: Astr. Ap., **128**, 212-229 (MMP)
117. McFeely, F.R., Cartier, E., Yarmoff, J.A., & Joyce, S.A. 1990: Phys. Rev. **B**, **42**, 5191
118. Mennella, V., Brucato, J.R. Colangeli, L., & Palumbo, P. 1999: Ap. J., Lett., **524**, L71-74
119. Merrill, P.W. 1934: P. A. S. P., **46**, 206-207
120. Mie, G. 1908: Ann. Phys. (Leipzig), **25**, 377
121. Mishchenko, M.I., Hovenier, J.W., & Travis, L.D. 2000: in Light Scattering by Nonspherical Particles: Theory, Measurements, and Applications (San Diego: Academic Press), 3-27
122. Mishchenko, M.I., Travis, L.D., & Macke, A. 2000: in Light Scattering by Nonspherical Particles: Theory, Measurements, and Applications (San Diego: Academic Press), 147-172
123. Morrish, A.H. 1965: The Physical Principles of Magnetism (New York: IEEE Press)
124. Morton, D.C. 1975: Ap. J., **197**, 85-115
125. Onaka, T., Yamamura, I., Tanabé, T., Roellig, T.L., & Yuen, L. 1996: P. A. S. J., **48**, L59-63

126. Overbeck, J.W. 1965: Ap. J., **141**, 864-886
127. Padoan, P., Goodman, A., Draine, B.T., Juvela, M., Nordlund, A, & Rögnvaldsson, Ö.E. 2001: Ap. J., **559**, 1005-1018
128. Pendleton, Y.J., & Allamandola, L.J. 2002: Ap. J. Suppl., **138**, 75-98
129. Purcell, E.M. 1969: Ap. J., **158**, 433-440
130. Purcell, E.M. 1975: in The Dusty Universe (New York: Neale Watson), 155-167
131. Purcell, E.M. 1979: Ap. J., **231**, 404-416
132. Roberge, W.G., Jones, D., Lepp, S., & Dalgarno, A. 1991: Ap. J. Suppl., **77**, 287-297
133. Roche, P.F., & Aitken, D.K. 1984: M.N.R.A.S, **208**, 481-492
134. Rogers, C., & Martin, P.G. 1979: Ap. J., **228**, 450-464
135. Rosenberg, D., & Wehner, G.K. 1962: J. Appl. Phys., **33**, 1842
136. Roth, J., Bohdansky, J., Pschenrieder, W., & Sinha, M.K. 1976: J. Nucl. Mat., **63**, 222
137. Routly, P.M., & Spitzer, L. 1952: Ap. J., **115**, 227-243
138. Salpeter, E.E., & Wickramasinghe, N.C. 1969: Nature, **222**, 442
139. Sarre, P.J., Miles, J.R., Kerr, T.H., Hibbins, R.E., Fossey, S.J., & Somerville, W.B. 1995: M.N.R.A.S, **277**, L41-43
140. Savage, B.D., Cardelli, J.A., & Sophia, U.J. 1992: Ap. J., **401**, 706-723
141. Scott, A., Duley, W.W., 1996: Ap. J., Lett., **472**, L123-125
142. Serkowski, K. 1973: in IAU Symp. No. 52, Interstellar Dust and Related Topics, eds. J. M. Greenberg and H. C. van de Hulst (Dordrecht: Reidel), 145-152
143. Slater, M., & Hashmall, J. 1992: NASA/Goddard Space Flight Center Document 554-FDD-89/001R3UD1
144. Slysh, V.I. 1969: Nature, **224**, 159
145. Smith, J.N., Meyer, C.H., Layton, J.K. 1976: Nucl. Tech., **29**, 318
146. Smith, R.K., & Dwek, E. 1998: Ap. J., **503**, 831-842
147. Sofia, U.J., & Meyer, D.M. 2001: Ap. J., **554**, L221-224 (and erratum: Ap. J., **558**, L147)
148. Spitzer, L. 1976: Comments Astrophys., **6**, 177-187
149. Stanimirovic, S., Stavely-Smith, L., van der Hulst, J.M., Bontekoe, T.J.R., Kester, D.J.M., & Jones, P.A. 2000: M.N.R.A.S, **315**, 791-807
150. Stecher, T.P., & Donn, B. 1965: Ap. J., **142**, 1681-83
151. Stein, S.E., & Brown, R.L. 1991: J. Am. Chem. Soc.,, **113**, 787-
152. Tanaka, M., et al. 1996: P. A. S. J., **48**, L53-57
153. Tielens, A.G.G.M., McKee, C.F., Seab, C.G., & Hollenbach, D.J. 1994: Ap. J., **431**, 321-340
154. Trumpler, R.J. 1930: P. A. S. P., **42**, 214-227
155. Turner, B.E. 1990: Ap. J., Lett., **362**, L29-33
156. van de Hulst, H.C. 1957: Light Scattering by Small Particles (New York: Dover)
157. Verstraete, L., Léger, A., d'Hendecourt, L., Défourneau, D., & Dutuit, O. 1990: Astr. Ap., **237**, 436-444
158. Voshchinnikov, N.V., & Farafonov, V.G. 1993: Ap. Sp. Sci., **204**, 19-86
159. Watson, W.D. 1973: J. Opt. Soc. Am., **63**, 164-
160. Waxman, E., & Draine, B.T. 2000: Ap. J., **537**, 796-802
161. Weingartner, J.C., & Draine, B.T. 1999: Ap. J., **517**, 292-298
162. Weingartner, J.C., & Draine, B.T. 2001a: Ap. J., **548**, 296-309 (WD01)
163. Weingartner, J.C., & Draine, B.T. 2001b: Ap. J., **553**, 581-594

164. Weingartner, J.C., & Draine, B.T. 2001c: Ap. J. Suppl., **134**, 263-281
165. Weingartner, J.C., & Draine, B.T. 2001d: Ap. J., **563**, 842-852
166. Westley, M.S., Baragiola, R.A., Johnson, R.E., & Baratta, G.A. 1995a: Nature, **373**, 405
167. Westley, M.S., Baragiola, R.A., Johnson, R.E., & Baratta, G.A. 1995b: Plan. Sp. Sci., **43**, 1311-1315
168. Witt, A.N., Smith, R.K., & Dwek, E. 2001: Ap. J., Lett., **550**, L201-205
169. Wolff, M.J., Clayton, G.C., Kim, S.-H., Martin, P.G., & Anderson, C.M. 1997: Ap. J., **478**, 395-402
170. Wright, E.L., Mather, J.C., Bennett, C.L., Cheng, E.S., Shafer, R.A., et al. 1991: Ap. J., **381**, 200-209